2018년 8월
박사학위 논문

서지유발 동기화 스위칭 기법에 기반한 우주용 냉각기 미소진동 에너지 수확용 피에조 시스템에 관한 연구

조선대학교 대학원
항 공 우 주 공 학 과
권 성 철

서지유발 동기화 스위칭 기법에 기반한 우주용 냉각기 미소진동 에너지 수확용 피에조 시스템에 관한 연구

- A Study on Surge-inducing Synchronous Switching Strategy for Spaceborne Cooler Micro-vibration Energy Harvesting Piezoelectric System -

2018년 8월 24일

조선대학교 대학원

항 공 우 주 공 학 과

권 성 철

서지유발 동기화 스위칭 기법에 기반한 우주용 냉각기 미소진동 에너지 수확용 피에조 시스템에 관한 연구

지도교수 오 현 웅

이 논문을 공학 박사학위 신청 논문으로 제출함.

2018년 4월

조선대학교 대학원

항 공 우 주 공 학 과

권 성 철

권성철의 박사학위논문을 인준함

위원장	조선대학교	교수	공 창 덕 (인)
위 원	한국항공대학교	교수	황 재 혁 (인)
위 원	조선대학교	교수	이 창 열 (인)
위 원	국방과학연구소	선임연구원	나 경 수 (인)
위 원	조선대학교	교수	오 현 웅 (인)

2018년 6월

조선대학교 대학원

Contents

LIST OF TABLES

LIST OF FIGURES

NOMENCLATURE

m	:	Tip mass of the piezoelectric harvester
c	:	Damping coefficient of the piezoelectric harvester
k	:	Stiffness of the piezoelectric harvester
α	:	Piezoelectric mechanical-electrical transformer coefficient
C_p	:	Clamped capacitance of the piezoelectric harvester
Q_p	:	Electrical charge in piezoelectric capacitance
Q_s	:	Electrical charge in storage capacitor
x	:	Displacement of the piezoelectric harvester
L_I	:	Inductor
R_{sw}	:	Switch resistance
D	:	Bridge diode
R_D	:	Diode resistance
C_s	:	Storage capacitor
V_p	:	Piezoelectric voltage
V_B	:	Inductor-induced voltage
V_s	:	Storage voltage in the storage capacitor
V_{fw}	:	Forward voltage drop induced by the bridge diode
i_p	:	Piezoelectric current
i_I	:	Inductor current
i_s	:	Storage current
$t_{\vert x_{\max}\vert}$	:	Time instant when the piezoelectric deflection, x, is maximum or minimum
τ_{opt}	:	Optimal switching duration calculated from $\pi\sqrt{L_I C_p}$

β	:	Switching duration factor
P_{ce}	:	Loss energy in electrical resistance
P_{in}	:	Absorbed energy in inductor
P_{sc}	:	Stored energy in storage capacitor
f_0	:	Vibration amplitude of the vibration source
w	:	Vibration frequency of the vibration source
$P_{Hi.Sw}$	:	High-frequency switching period
$f_{Hi.Sw}$	:	High-frequency switching frequency
$D_{Hi.Sw}$	:	PWM Duty cycle
ψ	:	High-frequency switching duration factor
$\overline{E_{cm}}$	:	Mechanical damping energy dissipated by the mechanical damping of the piezoelectric harvester
$\overline{E_{ce}}$	:	electrical energy absorbed in the piezoelectric harvester
$\overline{E_{av}}$	:	Piezoelectric force energy
$\overline{E_{ind}}$	:	Inductor working energy
$\overline{E_{loss}}$	:	Loss energy in resistances
$\overline{E_{out}}$	:	Net output energy
SSHI	:	Synchronized switching harvesting on inductor
S^3HI	:	Surge-inducing synchronized switch harvesting on inductor
H-S^3HI	:	High-frequency-included surge-inducing synchronized switch harvesting on inductor

초 록

서지유발 동기화 스위칭 기법에 기반한 우주용 냉각기 미소진동 에너지 수확용 피에조 시스템에 관한 연구

권 성 철
지도교수 : 오 현 웅
항공우주공학과
조선대학교 대학원

임무장비의 극저온 유지를 위한 냉각기, 위성의 자세제어용 액츄에이터인 플라이 휠, 자세정보 제공을 위한 기계식 자이로, 안테나의 기계적 구동이 가능한 김벌식 안테나, 태양전지판의 태양추적 구동기 등과 같이 기계적 회전 또는 병진 구동부를 갖는 탑재장비는 목적하는 기능을 구현함과 동시에 미소진동을 수반한다. 이러한 진동발생원으로부터의 진동외란은 그 크기가 극히 미소함에도 불구하고 정밀 지향성능이 요구되는 고해상도 관측위성의 영상품질을 저하시키는 주요 원인으로 작용하며, 관측위성의 고해상도 임무요구조건 충족을 위해서는 상술한 진동발생원으로부터의 미소진동은 항상 차폐의 대상으로만 존재하였다.

본 연구에서는 상술한 미소진동을 회수하여 전기에너지로 재생하는 에너지 하베스팅 기술의 적용 가능성에 주목하였으며, 에너지 하베스팅 기술의 우주적용을 목적으로 맥동형 우주용 냉각기를(Pulse Tube-Type Spaceborne Cooler) 에너지 재생원으로 선정하였다. 맥동형 냉각기는 일반적으로 신뢰도 만족을 위하여 비상모드를 제외하고는 상시 운용되어 지속적인 에너지 재생 및 활용에 있어 유리하고, 단일 특정 주파수로 냉각기가 구동되는 관계로 동특성 파악이 용이하여 에너지 하베스터 설계 관점에서 유리한 장점을 갖는다.

본 연구에서는 우주용 냉각기로부터 발생하는 미소진동을 전기에너지로 재생하기 위하여 진동·압력·충격 형태의 기계 에너지를 활용하는 피에조 기반의 에

너지 수확장치를 고안하였다.

피에조 기반의 에너지 수확장치는 다른 발전방법에 비해 에너지 밀집도가 높고, 설계가 용이하여 많은 진동원으로부터의 적용가능성 검토가 이루어졌고, 에너지 재생 효율을 높이기 위해 종래까지 많은 연구 및 기술 개발이 이루어 졌다. 이러한 효율증대를 위한 기술 개발에는 크게 하베스터의 구조적 설계를 최적화 하는 기계적 접근법과 전기 회로의 제어를 통한 전기적 접근법으로 구분된다. 기계적 최적화 설계는 외부 진동 주파수와 수확장치의 고유 진동수를 일치시켜 주 가진주파수 대역에서 최대의 기계-전기 에너지 변환이 가능한 반면, 수확된 전기 에너지의 충전 및 활용을 위한 적절한 전기회로의 설계 없이는 에너지 재생성능에 기술적 한계가 존재한다. 전술한 기계적 접근의 한계를 극복하고 더욱 향상된 에너지 재생성능 보장을 위해, 전기·전자 회로에 기초한 다양한 기법들이 연구 되었으며; Guyomar et. al. [1] 은 피에조 하베스터에서 발생한 전압신호 절대값의 최대치에 동기화 스위칭을 실시하여 인덕터의 역기전력 현상에 기인한 큰 전기 진동을 유발하였으며, 에너지 재생분야에 있어 비약적인 발전을 이루었다. 상기의 스위칭 기법은 SSHI(Synchronized Switching Harvesting on Inductor)로 지칭되며, 간단한 회로 구성만으로도 기능구현이 용이하여 다양한 관점에서의 연구가 수행되었고; 이를 기반으로 응용된 형태의 다양한 기법들이 보고되었다. 하지만, 전술한 SSHI기법을 적용하더라도 에너지 재생의 대상이 되는 외부진동원의 크기가 극히 미소할 경우 에너지 수확이 불가능한 기술적 제약이 존재하였다.

상기의 기술적 한계를 극복하기 위하여, 본 연구에서는 인덕터의 물리적 관성효과를 이용한 서지유발 동기화 스위칭 기법을(Surge-inducing Synchronous Switching Harvesting on Inductor) 제안하였으며, 스위칭 직후 발생하는 서지 전압은 정류회로 및 베터리에 기 충전된 전압량에 의해 존재하는 문턱전압을 상회하는 크기로 증폭되어, 기존 스위칭 기법 적용 시 에너지 재생이 불가능한 수준의 미소진동에서도 유효한 수준의 에너지 재생이 가능하다. 본 연구에서 적용한 서지유발 동기화 스위칭 기법은 스위칭 시간 및 형태(예, 고주파)를 적절히 조절함으로써 최적의 성능보장이 가능하다. 본 연구에서 제안한 스위칭 기법의 유효성 검증을 목적으로, 켄틸레버 형태의 피에조 단독 수준에서 기본특성 시험

및 이로부터 도출된 특성치를 토대로 수치해석을 실시하였으며, 실제 개발된 스위칭 회로와의 조합으로 성능시험을 실시하여 설계의 유효성을 입증하였다. 아울러, 우주용 냉각기와 피에조 하베스터, 스위칭 회로의 결합으로 구성된 복합시스템 수준에서 기능 및 성능시험을 실시하여 본 연구에서 제안한 서지유발 동기화 스위칭 기법은 우주용 냉각기로부터 발생하는 미소진동 에너지의 수확이 가능함을 입증하였다.

핵심어 : 미소진동, 우주용 냉각기, 에너지 수확, 피에조, 서지현상

ABSTRACT

A Study on Surge-inducing Synchronous Switching Strategy for Spaceborne Cooler Micro-vibration Energy Harvesting Piezoelectric System

by Kwon, Seong-Cheol
Advisor : Prof. Oh, Hyun-Ung, Ph. D.
Department of Aerospace Engineering
Graduate School of Chosun University

The spaceborne cryocooler is widely used to cool the focal plane of an infrared imaging sensor. However, such a spaceborne cooler produces undesirable micro-vibration during its on-orbit operations. Even if its amplitudes are regarded as micro-scale, the cooler-induced vibration disturbances significantly affect the image quality of the high-resolution observation satellite.

To manage the micro-vibration induced by the cooler, passive-type isolators are generally employed in space program owing to their simplicity and reliability. However, efforts to positively utilize the micro-vibration energy as a renewable energy source have not been made in space applications but only forwarded to reducing the micro-vibration to obtain high-quality images from the observation satellite. At this point, we focus on the feasibility of positively utilizing the micro-vibration as a renewable power source by employing energy harvesting technology.

The energy harvesting technology has recently received remarkable attention. Hence, a great deal of research has been directed toward developing energy-harvesting systems over the past decade. However, the efforts to

facilitate their application into space were scarce. Because the low vibration amplitudes, regarded as micro-scale, has so far acted as an entry barrier for the harvesting technology.

In terms of energy harvesting methods, piezoelectric elements, in particular, have received considerable attention because of their high-power density and promising integration potential, as well as widely available vibratory energy sources in various fields, to the extent that several researchers have dealt with the piezoelectric element as promising potential energy harvesting applications. In line with the increased attention on piezoelectric elements, various technical efforts to enhance their energy harvesting capability have been made as well. For example, Guyomar et al. [1] proposed a non-linear harvesting technique, called synchronized switch harvesting on inductor (SSHI). The proposed SSHI technique has garnered considerable attention on account of its practical applicability and superiority in harvesting performance. However, such a technique could only bring their advantages, provided that the amplitude of vibratory source is large enough to generate a piezo-induced voltage in which its level can overcome the threshold voltage. Hence, the micro-scale vibration acts as an entry barrier for such harvesting techniques.

To overcome above mentioned drawbacks of the conventional SSHI, a novel switching strategy that exploits the full potential of the surging phenomenon has been proposed. This switching strategy locates the synchronous switch on a different position compared with the conventional SSHI, such that the inductor employed in the proposed strategy acts as a charge-pump unlike its role in the conventional SSHI. In the proposed switching scheme, the switching duration is intentionally shortened compared with the optimal switching duration of the conventional SSHI in order to induce sudden current transits in the inductor. Thereby, the piezoelectric voltage can be substantially boosted over the threshold voltage, even if the

vibration amplitudes are regarded as micro-scale.

On the other hand, above mentioned S^3HI strategy inevitably suffers from a series of energy losses in the inductor at every instance of switching, due to its relatively shorter switching duration compared with the conventional SSHI strategy. To overcome such a drawback of the S^3HI strategy, while still striving to induce surge phenomena to exploit their full potential from the point of view of energy harvesting capability, an advanced strategy that combines high-frequency switching with the S^3HI strategy is proposed as well. The basic concept of the proposed strategy is to make the switching duration relatively longer than the S^3HI strategy, while finely splitting it up to realize the high-frequency switching. Thereby, both the demands of maximizing the incoming energy in the inductor and maintaining the surge-inducing mechanism can be satisfied by the proposed strategy, which we called the high-frequency-included surge-inducing synchronized-switch harvesting (H-S^3HI) strategy.

Based on above mentioned strategies, i.e. S^3HI and H-S^3HI, the feasibility of harvesting the cooler-induced miro-vibration energy has been evaluated under the cooler assembly level which comprises the cooler, the passive vibration isolator, the piezoelectric harvesters, and the switching circuit.

Key Word: Micro-vibration, Spaceborne Cooler, Energy Harvesting, Piezoelectricity, Surging Effect

Ⅰ. Introduction

The line-of-sight (LOS) jitter on an imaging sensor of a high-resolution observation satellite is defined as time-varying motion on the focal plane during image acquisition, which is caused by internal and external disturbances acting on the optical payloads [2]. To comply with the strict mission requirements, the jitter level should be predicted accurately through numerical or experimental approaches to determine whether it meets the given specifications. If the jitter level exceeds the given requirements, a technical mitigation plan has to be implemented to manage the jitter properly.

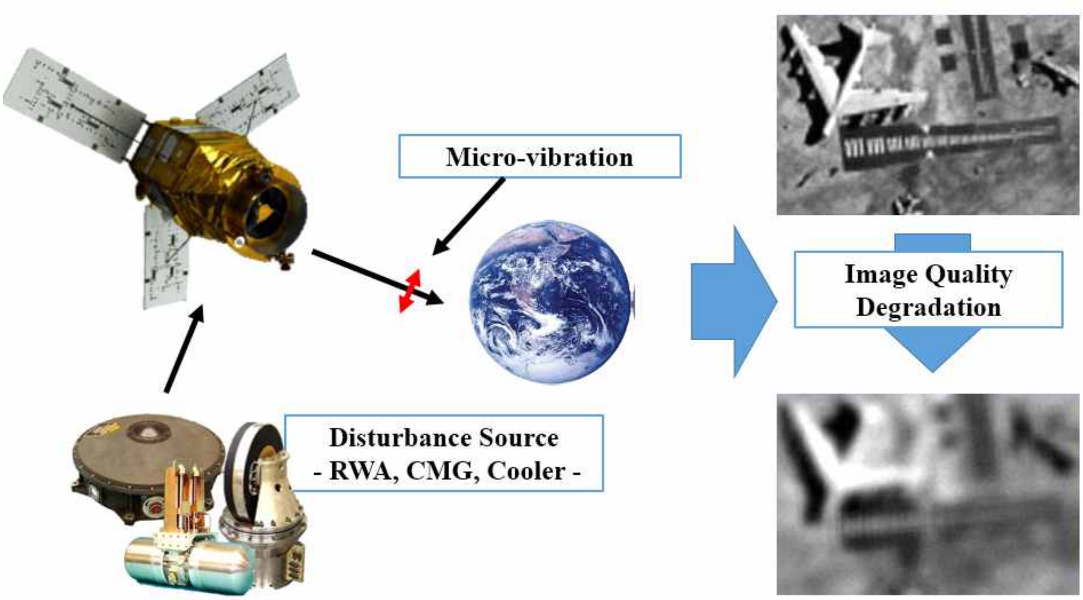

Fig. 5 Image Quality Degradation due to Micro-vibration Disturbance Sources

The internal jitter contributors of the satellite commonly have mechanical moving parts such as the reaction wheel assembly (RWA), the control moment gyroscope (CMG) for altitude control, the gimbal-type data link antenna for transmitting massive image data to a ground station, and the spaceborne cryocooler to cool the focal plane of an infrared imaging sensor. Micro-jitter is a term generally used in the spacecraft community to describe low amplitude vibrations, which are a main source of image quality degradations [3-10]. (See below Fig. 1)

To manage the micro-jitter induced by the aforementioned internal contributors, passive-type isolators are generally employed in space applications owing to their simplicity and reliability [11-20]. However, efforts to positively utilize the micro-jitter energy as a source of renewable energy have not been made in space applications but only forwarded to reducing the micro-jitter to obtain high-quality images from the observation satellite. At this point, we focus on the feasibility of positively utilizing the micro-jitter as a renewable power source by employing energy harvesting technology.

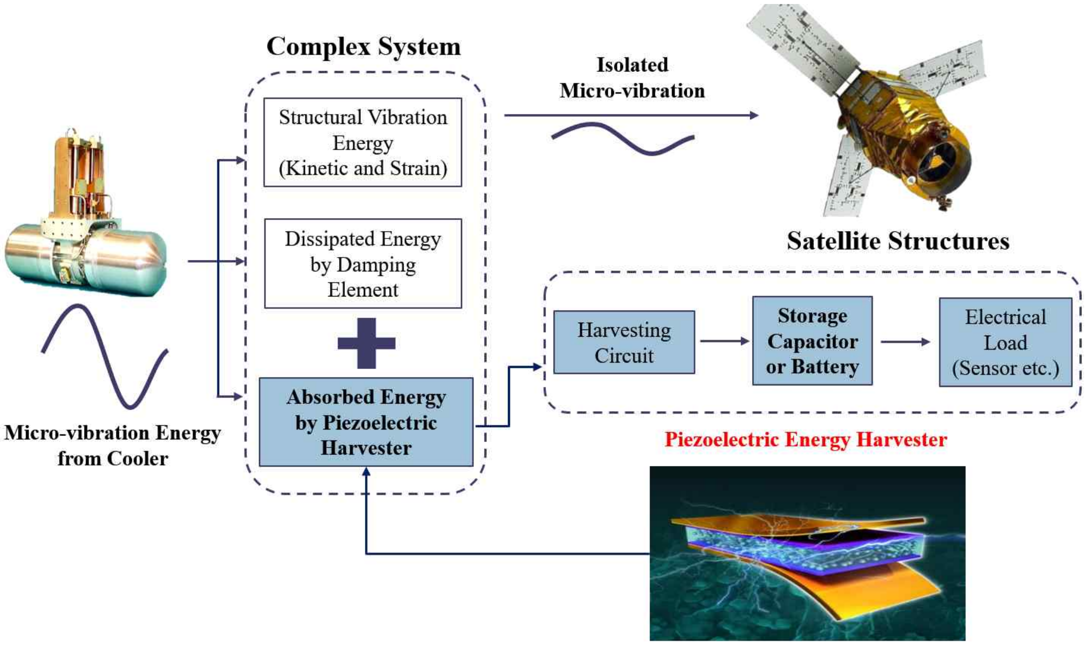

Fig. 6 Cooler-induced Micro-vibration and Its Applicability on Energy Harvester

The energy harvesting technology has recently received remarkable attention in the context of its increasing use in portable, implantable, and ubiquitous sensor nodes. Moreover, low power-consuming microsystems used in daily applications, as well as the increasing demand for self-powered health-monitoring sensor systems in extremely isolated environments have triggered a need for compact and efficient energy management. Hence, a great deal of research has been directed toward developing energy-harvesting systems over the past decade [21–24]. For example, Ylli et al. [21] reported two kinds of energy-harvesting system exploiting swing and shock excitations from the human motion. Each harvester was characterized under different motion speeds to maximize its energy-harvesting capability with respect to swing and heel strike motions. The effectiveness of the harvester was evaluated by incorporating numerical simulations and experiments in different motion speeds. Zhongjie et al. [22] proposed an energy-harvesting shock absorber with a mechanical motion rectifier. This application was able to recover the energy, otherwise, dissipate the suspension vibration of the vehicle while simultaneously suppressing the vibration induced by road roughness. This system can work as a vibration damper as well as an energy generator. The key component of the regenerative shock absorber was a unique motion mechanism, which was called the mechanical motion rectifier, to convert the oscillatory vibration of the suspension into the unidirectional rotation of the generator, which allows the harvester to directly regenerate DC power without applying an electrical rectifier circuit. The validity of the shock absorber was investigated through experiments on the smooth paved road. Thomas et al. [23] proposed a micro-power electromagnetic harvester to generate electrical power from the seismic motion of the human body. The purpose of the harvester was to power portable body-worn sensors and personal electric devices. The validity of the harvester design was investigated through practical experiments using human walking motions. Dibin et al. [24] reported a tunable vibration-based electromagnetic micro-generator, which had a wide tuning range that allowed it to produce wide-band electrical power over a wide range. They also evaluated the effectiveness of the generator design through theoretical analysis and experimental results.

As exemplified above, many studies have been conducted for on-ground energy harvesting applications. Several types of applications are even being implemented on a commercial scale. However, the efforts to facilitate their application in space were scarce. Because the low vibration amplitudes, regarded as micro-scale, has so far acted as an entry barrier for the harvesting technology. Thus, only a few basic studies have been reported for the space application. For example, Makihara et al. [25] proposed a semi-active energy-harvesting vibration-suppression system using a piezoelectric actuator. They verified its feasibility through a vibration-suppression test on a large truss structure. Kwon et al. [26-30] proposed a tuned mass damper-type electromagnetic energy harvester, for the spaceborne cooler. They verified the feasibility of using the harvested energy by driving a low power-consuming accelerometer to measure the cooler-induced vibration level itself. As a result, a self-powered standalone vibration sensor system was implemented by using the recycled energy from cooler-induced micro-vibrations.

On the other hand, the technological progress in sensor applications has triggered the development of nano-watt powered sensor systems. This advancement allows overcoming critical obstacles that prevent the realization of energy harvesting systems, especially on micro-vibration fields. Among the examples for the nano-watt powered sensors, Shimamura et al. [31] developed a nano-watt powered vibration sensor for ambient intelligence application. This sensor system barely dissipates power at the rate of 0.7 *n*W/h during the vibration sensing mode, and its feasibility was verified through an experimental approach. Besides, micro-electromechanical systems (MEMS)-based sensor are being increasingly evaluated for an attractive technology, as the use of such MEMS-based sensor results in drastic reduction in power consumptions enabled by the miniaturization of components [32]. As a result, the power requirements of MEMS-based devices can be substantially minimized such that the energy harvesting technology can be a high potential alternative, contributing to the increase of power budget and reducing the overall mass of the system. As well as such a low power-consuming MEMS-based sensor system has triggered the use of energy harvesting technology toward space applications.

In terms of energy harvesting methods, piezoelectric elements, in particular, have received considerable attention because of their high-power density and promising integration potential, as well as widely available vibratory energy sources in various fields [33–34], to the extent that several researchers have dealt with the piezoelectric element as promising potential energy harvesting applications. In line with the increased attention on piezoelectric elements, various technical efforts to enhance their energy harvesting capability have been made as well. For example, Guyomar et al. [1] proposed a non-linear harvesting technique, called synchronized switch harvesting on inductor (SSHI). The proposed SSHI technique has garnered considerable attention on account of its practical applicability and superiority in harvesting performance, such that various spawned research based on the SSHI technique have been reported, i.e., self-powered SSHI (SP-SSHI) [35], velocity control SSHI (V-SSHI) [36], and synchronous electric charge extraction (SECE) [37].

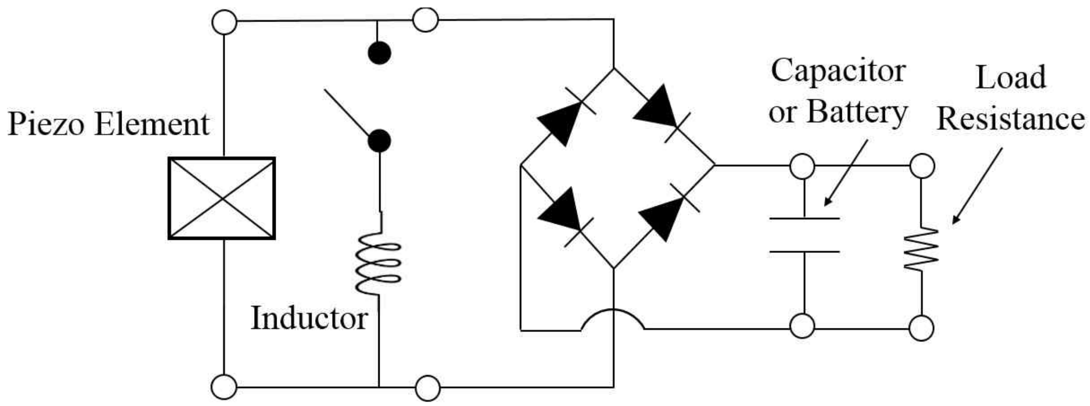

Fig. 7 Synchronized Switch Harvesting on Inductor (SSHI) Toplogy [1]

Among abovementioned examples, the SSHI topology optimizes the power output of a piezoelectric element. As seen in the electrical equivalent circuit, the piezoelectric element has a capacitance which will cause a 90° phase shift between the voltage and the current. The main idea of the technique is to eliminate the phase shift between the piezo-induced current and voltage by making the voltage self commutate and thus optimize the energy output. The SSHI method utilizes an inductor to remove this phase shift, by temporarily switching it with the piezoelectric capacitance and letting it oscillate with the capacitance only for half a period, i.e. until the piezoelectric voltage is inverted. As shown in Fig. 3, the inductor is connected with the piezo element when the switch is closed. The switch is open until maximum displacement in the transducer occurs, which correspond to a maximum bend in the material and to the maximum voltage generated. At this instance the switch gets closed briefly and the inductor will oscillate together with the capacitance of the piezo. The switch opens again after half a period of the oscillation frequency between the inductor and piezoelectric capacitor. Then the piezo voltage is reversed.

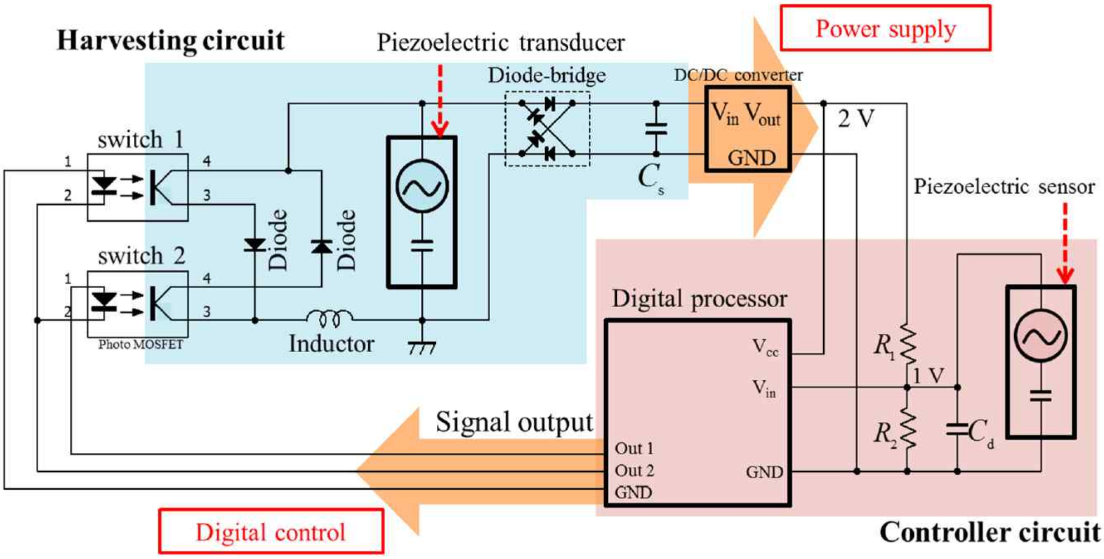

Fig. 8 Self-powered SSHI Topology that includes a Digital Processor [35]

A self-powered energy harvester based on SSHI (SP-SSHI) topology [35] was also researched and below Fig. 4 shows a representative circuit topoloty of the SP-SSHI which mainly consists of a digital processor and a piezoelectric sensor, which allows the application of a technical method to improve the energy-conversion efficiency. The method was implemented by measuring the vibration displacements, processing the data digitally, and adequately regulating electric switches. These operations were managed by a built-in digital processor. The driving power for the digital processor was satisfied with a part of the energy harvested from structural vibrations. Thus, the harvester operates flexibly with the digital processor to enhance electrical energy generation, and requires neither batteries nor an external power supply.

The velocity control SSHI (V-SSHI) topology [36] shown in Fig. 5 was proposed to compensate the phase lag which resulted from the peak detector implemented in the conventional SSHI [1]. Such a phase lag always existed between the peak voltage of the piezoelectric element and the actual switching time, thereby the harvesting performance of the conventional SSHI was inevitably degraded. However, V-SSHI topology actively determines the switching instant via observing the velocity state such that there was no phase lag, contributing to the improvement of the harvesting performance.

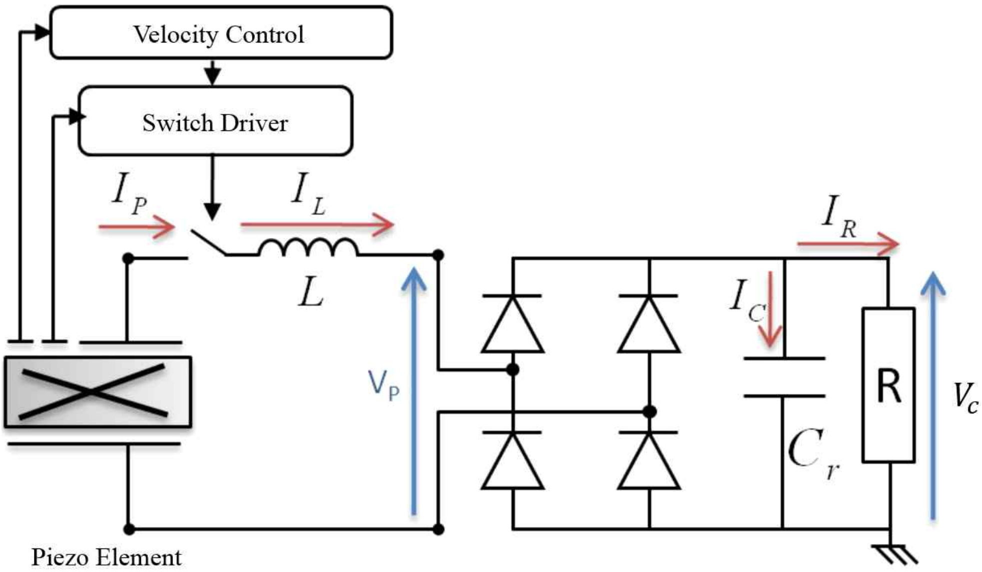

Fig. 9 Velocity Control SSHI Topology [36]

The synchronous electric charge extraction (SECE) converter topology [37] is shown in Fig. 6. In this topology, the switch turns ON at every voltage peak and all the energy stored in the piezoelectric capacitor is transferred as magnetic energy to the inductor. When the piezoelectric voltage reaches zero, the switch turns OFF and the energy flows from inductor to the load. It can be argued that this technique is less efficient than the SSHI strategy [1] due to the fact that the piezoelectric element absorbs the vibration energy for extracting the charge when the piezoelectric voltage becomes higher or lower based on zero, suppressing the vibration amplitudes. Otherwise, the SSHI helps the movement of the piezoelectric harvester, contributing to the flow of charge out easier.

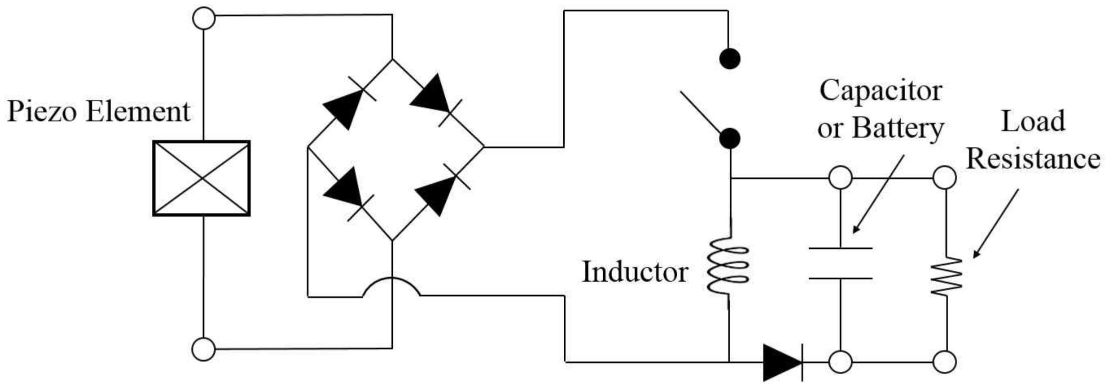

Fig. 10 Synchronized Charge Extraction Harvesting Topology [37]

These various techniques were efficient in boosting the voltage produced by the piezoelectric harvester. However, such addressed techniques could only bring their advantages, provided that the amplitude of vibratory source is large enough to generate a piezo-induced voltage in which its level can overcome the threshold voltage accompanied by rectifying diodes and existing voltage in storage device, i.e. capacitor or battery. Hence, the micro-scale vibration acts as an entry barrier for such harvesting techniques. In addition, above addressed techniques could only yield a reasonable harvesting performance under the periodic vibration condition, i.e. sinusoidal vibration, due to their switching mechanism that must be synchronized with the vibratory movements of the piezoelectric harvester for their optimal performances. As a result, these techniques require feedback controller and state-observer to implement the synchronized switch, negatively causing system complexity and reliability. Hence, such a synchronized method could not be applied in random vibration conditions because the vibration status cannot be characterized at every single moment. Thereby, no reasonable harvesting capability can be expected under the random vibration.

To overcome above mentioned drawbacks of the conventional synchronized switching strategy, a novel switching strategy that exploits the full potential of the surging phenomenon has been proposed. This switching strategy locates the synchronous switch on a different position compared with the conventional SSHI, such that the inductor employed in the proposed strategy acts as a charge-pump unlike its role in the conventional SSHI in which the inductor only executes voltage-inverting actions at each switching instant. In the proposed surge-inducing switching scheme, the current from the piezoelectric element flows toward the inductor at the switching instant and the current is suddenly discharged right after the switching off. In here, the switching duration was intentionally shorter compared with the optimal switching duration of the conventional SSHI [1] to induce sudden current transits in the inductor. Thereby, the piezoelectric voltage can be substantially boosted over the threshold voltage accompanied by the forward voltage drop of the diode, even if the vibration amplitudes are regarded as micro-scale in which its value is too small to charge the storage device when using the conventional SSHI technique. The energy harvesting capability of the surge-inducing strategy can be further enhanced by employing an optimal switching duration. In this study, the effectiveness of the surge-inducing switching strategy, which we called the surge-inducing synchronized-switch harvesting on inductor (S^3HI) strategy, has been demonstrated through a numerical simulation and the functional performance of the surge-inducing switching strategy are then experimentally assessed by implementing a cantilever type piezoelectric harvester. In addition, the validity of using S^3HI in random vibration harvesting has been demonstrated.

On the other hand, above mentioned surge-inducing strategy inevitably suffers from a series of energy losses in the inductor at every instance of switching, due to its relatively shorter switching duration compared with conventional SSHI. To overcome such a drawback of the surge-inducing switching strategy while still striving to induce surge phenomena to exploit their full potential from the point of view of energy harvesting capability, an advanced strategy that combines high-frequency switching with the surge-inducing switching is proposed in this study as well. The basic concept of the proposed strategy is to make the switching duration relatively longer than the above mentioned surge-inducing strategy, while finely splitting it up to realize high-frequency switching. Thereby, both the demands of maximizing the incoming energy in the inductor and maintaining the surge-inducing mechanism can be satisfied by the proposed strategy, which we called the high-frequency-included surge-inducing synchronized-switch harvesting (H-S^3HI) strategy. To investigate the feasibility of the proposed switching strategy, numerical simulations were performed based on the output of basic characteristic tests. The effectiveness of the H-S^3HI strategy was then demonstrated via performance evaluation tests with a simple cantilever-type piezoelectric energy harvester, and its output was compared with that of switching strategies, i.e., SSHI [1] and S^3HI. In addition, the validity of using H-S^3HI in random vibration harvesting has been experimentally demonstrated.

Based on numerical and experimental output resulted of the surge-inducing strategies, i.e., S^3HI and H-S^3HI, with a cantilever-type piezoelectric energy harvester, the feasibility of harvesting the cooler-induced miro-vibration energy has been evaluated under the complex system level which comprises the cooler, the passive vibration isolator, a pair of piezoelectric harvester, and surge-inducing switching circuit. The complex system level performance evaluations were performed with regard to the electrical connection of the piezoelectric harvesters in either parallel or series. Then, its outputs were assessed in terms of harvesting energy and vibration isolation performances.

This paper has demonstrated the “Surge-inducing Synchronous Switching Strategy for Spaceborne Cooler-induced Micro-vibration Harvesting on Piezoelectric System” and proceeded as followings:

The chapter II introduces the spaceborne cooler as a renewable energy target and the piezoelectric element.

The chapter III introduces the surge-inducing switching strategy, called S^3HI. In addition, numerical and experimental demonstrations of the S^3HI strategy has been addressed.

The chapter IV introduces the high-frequency-included surge-inducing synchronized-switch harvesting on inductor strategy, called H-S^3HI. In addition, numerical and experimental demonstrations of the H-S^3HI strategy has been addressed.

The chapter V introduces the complex system. In addition, the feasibility of harvesting the cooler-induced micro-vibrations by employing the proposed strategies, i.e., S^3HI and H-S^3HI, has been numerically and experimentally investigated.

The final chapter deals with the conclusion, the future study, and the reference

II. Energy Harvesting Target and Piezoelectricity

A. Pulse-tube Type Spaceborne Cooler

In space applications, pulse-tube type coolers shown in Fig. 7, that mainly comprise the transfer line for transferring the cryogenic helium gas and the cold finger for making a connection between the cooler and the mission payload, are widely used to cool down the focal plane of an IR imaging sensor to low cryogenic temperatures, on account of their advantages of simplicity, low cost, and high reliability [38-39]. The major advantage of such cooler in comparison with stirling-type coolers [40] is the absence of any moving part in the cold finger, which results in a considerably longer mean time to failure (MTFF). Another advantage of such cooler is that their vibration output is lower than that of stirling-type coolers as shown in Fig. 8, which is an essential requirement for high-resolution observation satellites. However, such a cooler also produces undesirable micro-vibration during its on-orbit operations, which seriously affects the image quality of high-resolution observation satellites. Therefore, to obtain high-quality images from high-resolution observation satellites, the micro-vibration induced by spaceborne cooler has been always subjected to an isolation objective

However, in this study, a pulse-tube type cooler has been selected as a renewable energy source target, due to its several advantages in terms of energy-harvesting system. For instance, the harvester can continuously generate electrical power because the cooler is continuously operated over the entire orbit, except during the safe-hold mode when the cooler is powered off. In addition, the singular operating frequency of the cooler is easy to characterize, which is advantageous for designing the energy harvester.

The major characteristics of the pulse-tube type cooler used in this study are 3.8 kg, main excitation frequency 40 Hz, and maximum force 2.5 N, respectively.

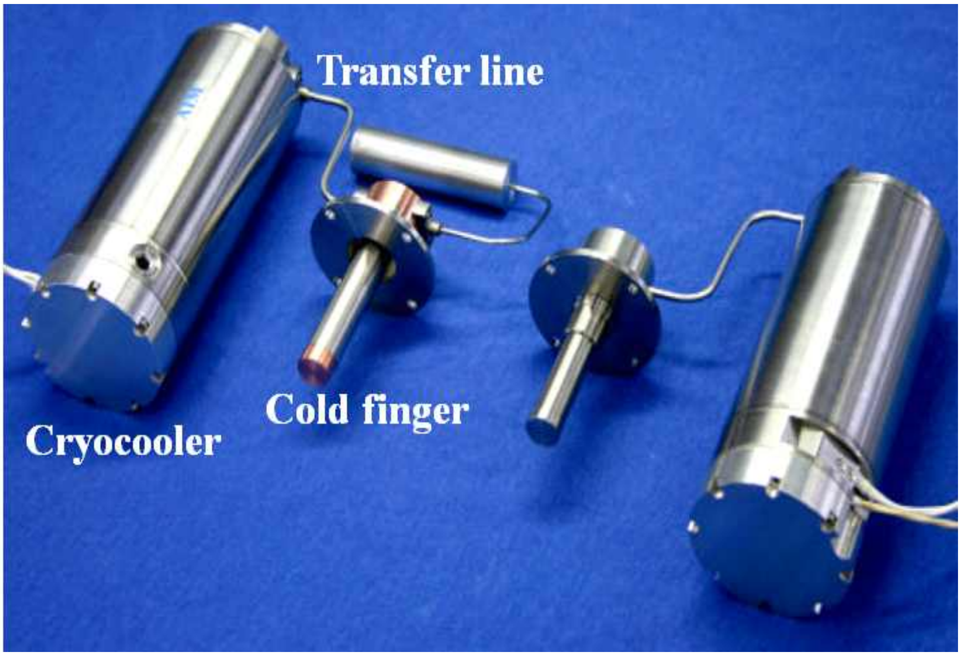

Fig. 11 Pulse-tube Type Cooler [38]

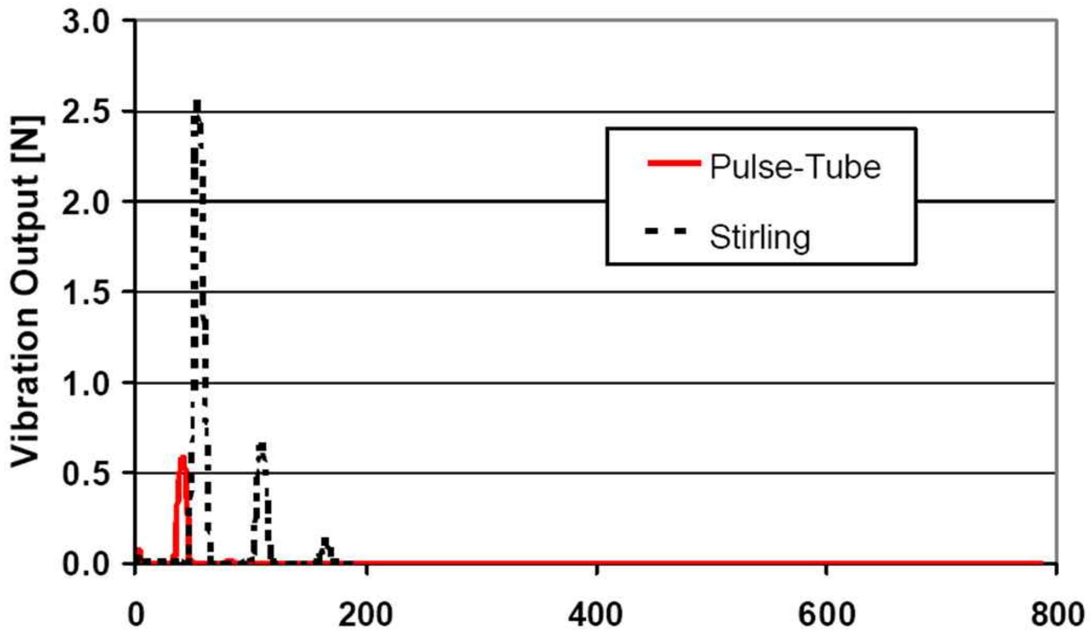

Fig. 12 Vibration Outputs of Pulse-tube and Stirling Type Coolers [39]

B. Piezoelectric Element

The piezoelectric effect refers to a coupling between strain and polarization for certain materials due to their crystalline structure. When a material with piezoelectric properties is mechanically strained, either in compression or tension, an electric potential is induced in the material [41]. This property, illustrated in Fig. 9, is referred to as the direct piezoelectric effect. Piezoelectricity is a reciprocal property, meaning that an applied electric potential induces a mechanical strain in the material. This is referred to as the indirect piezoelectric effect. For harvesting vibration energy, the direct piezoelectric effect is utilized to convert energy from the mechanical domain to the electrical domain.

The presence of piezoelectric behavior in a material is determined by its crystal structure. Crystalline materials have atomic structures where the atoms are arranged in a periodic lattice. The smallest arrangement of atoms that can accurately represent the lattice is referred to as a unit cell [42]. In order for a material to exhibit piezoelectricity, the crystalline structure must be non-centro-symmetric, meaning that there is no center of symmetry within a unit cell. When a piezoelectric crystal is mechanically deformed, the lack of symmetry leads to the formation of electric dipoles which induce an electric field in the material [43]. Electrodes placed on the surface of the material experience a voltage differential as a result of the induced field. This effect was first demonstrated in quartz by Pierre and Jacques Curie in 1880 [44]. In addition to quartz, common piezoelectric materials include, lead zirconate titanate (PZT), aluminum nitride (AlN), zinc oxide (ZnO), and polyvinyldine fluoride (PVDF). Materials with piezoelectric properties are dielectrics, meaning that they are electrical insulators and hence conduct current poorly. As such, when electrodes are placed on the surface of a piezoelectric layer, the resulting device is essentially a capacitor. Applied stress induces a voltage across the piezoelectric capacitor. However, piezoelectric materials are not perfect insulators, and the induced voltage decays with time [45].

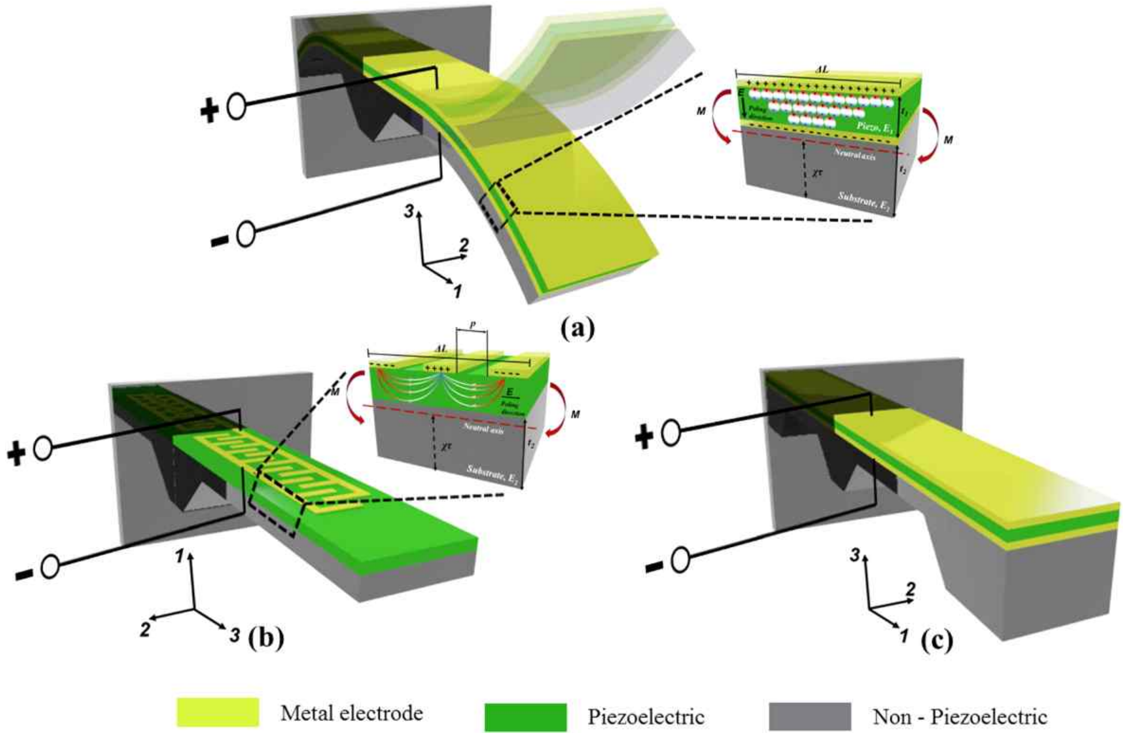

Fig. 13 Schematic of Common Cantilever Configurations for Piezoelectric Energy Harvester: [(a): Cantilever in d31 Configuration, (b): Cantilever with IDEs Electrodes in d33 Configuration, (c): d31 Cantilever with Added Proof Mass]

For a linear piezoelectric material, the electro-mechanical coupling can be expressed quantitatively by the following constitutive equations:

$$\{S\} = [s^E]\{T\} + [d]^{tr}\{E\} \tag{2-1}$$

$$\{D\} = [d]\{T\} + [\varepsilon^T]\{E\} \tag{2-2}$$

where $\{S\}$ is the strain vector, $[s^E]$ is the compliance matrix, $\{T\}$ is the stress vector, $[d]$ is the piezoelectric coefficient matrix, $\{E\}$ is the electric field vector, $\{D\}$ is the electric displacement vector, and $[\varepsilon^T]$ is the permittivity matrix. The superscripts ^{E} and ^{T} indicate that the compliance and permittivity matrices are calculated with constant electric field and stress conditions, respectively. The superscript ^{tr} indicates a matrix transpose. If $[d]$ is all zero, indicating no coupling between the mechanical and electrical domains, then Eqs. (2-1) and (2-2) reduce to the uncoupled equations for an elastic dielectric material [46]. When using piezoelectric materials for vibration energy harvesting, there are two available modes of electro-mechanical coupling, namely the 31 and 33 modes. The numbers are used to represent the different modes, 1, 2 and 3, which refer to the orthogonal axes of a 3-dimensional coordinate system. By convention, the 3-direction refers to the direction of polarization of the piezoelectric material. The 31 mode therefore describes a transducer where strain is applied in the 1-direction, and the electric potential is generated in the 3-direction. Similarly, the 33 mode is characterized by strain in the the 3-direction and an electric potential also in the 3-direction. Both modes, i.e. 31 and 33, are shown in Fig. 10. The geometry of the piezoelectric material and placement of the electrodes will ultimately determine which electro-mechanical mode is harnessed for transduction.

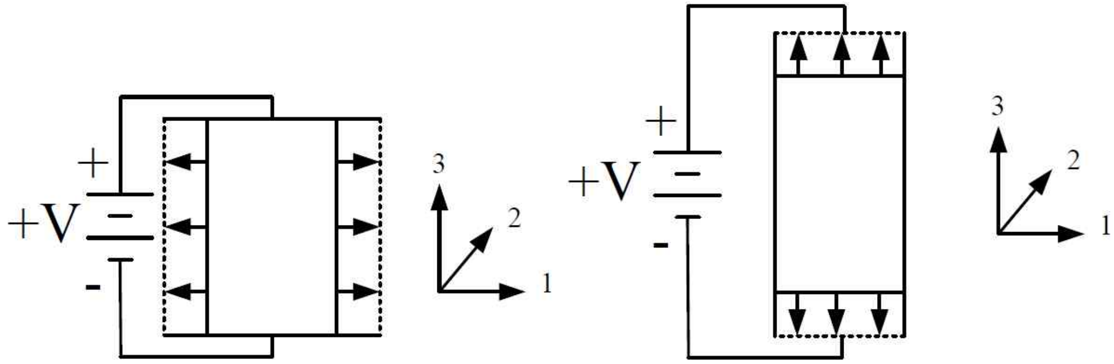

(a) (b)

Fig. 14 Schematics of the Piezoelectric Harvester's Common Operating Modes: [(a): 31 mode, (b): 33 mode]

For energy harvesters using the 31 mode, simple cantilever beam geometries are typically implemented. The cantilever beam is either clamped at one end, or clamped at both ends to provide clamped-clamped boundary conditions. Piezoelectrics with this geometry can be further divided into unimorph and bimorph types. Unimorphs have a single piezoelectric layer, while bimorphs have top and bottom layers with opposing polarities. More layers can be implemented, changing the output current to voltage ratio, but if the total thickness of piezoelectric material does not change, the total harvested power is not affected. A typical 31 cantilevered beam unimorph transducer is shown in Fig. 9. As the free end of the cantilever is displaced relative to the fixed end, strain is developed in the substrate and piezoelectric layer in the 1-direction. The electrodes, placed on the top and bottom of the piezoelectric material, produce an electric field in the 3-direction. For this mode, assuming a transversely isotropic material, e.g. PZT, the constitutive equation given by Eqs. (2-1) and (2-2), reduces to as followings:

$$S_1 = s_{11} T_1 + d_{31} E_3 \tag{2–3}$$

$$D_3 = d_{31} T_1 + \varepsilon_{33} E_3. \tag{2–4}$$

The stress and electrical displacement in Eqs. (2–3) and (2–4) are coupled by the d_{31} piezoelectric coefficient. Meanwhile, since many piezoelectric materials are comprised of brittle ceramics, the piezoelectric and electrodes are bonded to a substrate to prevent the transducer from cracking or snapping as it is vibrates. A proof mass can be included to add more mass at the tip, thus increasing the strain induced in the piezoelectric. It also provides additional degrees of freedom for tuning the resonant frequency of the transducer. Similarly to the 31 mode, a cantilevered beam configuration is shown to demonstrate the operation of 33 mode transducers. Figure 10 shows the geometry of the 33 mode transducer. The displacement of the free end of the cantilever, relative to the fixed end, causes strain to be induced in the piezoelectric layer in the 3-direction. For this mode of operation, the constitutive equations reduce to followings:

$$S_3 = s_{33}T_3 + d_{33}E_3 \tag{2-5}$$

$$D_3 = d_{33}T_3 + \varepsilon_{33}E_3. \tag{2-6}$$

In the 33 mode, the coupling is therefore determined by the d_{33} piezoelectric coefficient.

On the other hand, one of the main advantage of piezoelectric energy harvesting methods are the ability to produce significant output voltages, compared with the electro-magnetic methods that are typically confined to the mV range. Otherwise, the piezoelectric harvester can be capable of producing voltages in the ranges of 10 to 100 V. This is quitely useful in minimizing the effects of voltage drops resulted from the typical rectification. In general, single crystal piezoelectric materials provide good electro-mechanical coupling properties, but are very expensive to fabricate. In order to batch fabricate piezoelectric transducers, thin films are available. However, such thin films tend to have poor piezoelectric properties. When choosing a piezoelectric material for a specific application, the piezoelectric coefficient, i.e. d_{31} or d_{33}, is often considered first, since it heavily relates both deformation to applied voltage, namely direct piezoelectric effect, and induced charge to applied strain, naemly indirect piezoelectric effect. Table 1 shows the representative d_{31} and d_{33} with regard to the material compositions of the piezoelectric harvester. However, for energy harvesting applications, it is also important to consider the electro-mechanical coupling coefficient κ^2, which quantifies the ratio of energy transferred from one energy domain to another [47]. Specifically, in vibration energy harvesting field, κ^2 describes the transfer of energy from the mechanical domain to the electrical domain. For a single sheet of piezoelectric material, the value of κ^2 is a material property given by:

$$\kappa^2 = \frac{d^2 E}{\epsilon} \tag{2-7}$$

Table 1 Representative d_{31} and d_{33} with regard to Material Compositions of Piezoelectric Harvester

	ZnO	AIN	PVDF	PZT	PMN-PT
d31 (pC/N)	-2.3 ~ -4.7	-2	-8	-171 ~ 340	-777 ~ 977
d33 (pC/N)	0.19	-	0.12	0.22 ~ 0.41	0.52

1. Design Driver of the Piezoelectric Harvester

The piezoelectric harvester, in particular, have received considerable attention because of their high-power density and promising integration potential, as well as widely available vibratory energy sources in various fields. Thus, piezoelectric harvester was selected as an energy harvester in this study. As a design driver, the 1^{st} eigenfrequency of the piezoelectric harvester should meet the main excitation frequency of the cooler, namely 40 Hz, in order to obtain mechanical resonant effects on the piezoelectric harvester. In this manner, substantial deflections on the piezoelectric layer occur and thereby significant electrical potentials in the piezoelectric layer are produced, which can be implied in above Eq. (2-2). Based on these addressed design driver, a simple cantilever-type piezoelectric harvester was designed. Figure 11 shows the finite element model (FEM) of the piezoelectric harvester established. In this model, ceramic-based piezoelectric material composed of lead zirconium titanate (PZT) was considered due to its high piezoelectric coefficient, contributing to high voltages in the piezoelectric harvester. This piezoelectric layer has a size of 50 mm $\times$ 28 mm $\times$ 0.2 mm and is bonded on a sus-based substrate to prevent it from cracking or snapping as a result of vibration itself. The substrate has a size of 100 mm $\times$ 30 mm $\times$ 0.8 mm and has bolt interfaces at one end to implement a cantilever configuration. The substrate also has a tip mass interface to include a proof mass at the tip, enabling easier tuning of the 1^{st} eigenfrequency of the piezoelectric harvester by adjusting the proof mass. From the preliminary study, the proof mass was determined to be 27.7 gram and the 1^{st} modal analysis result with the above mentioned configuration was shown in Fig. 12. As can be seen this figure, the piezoelectric harvester in combination with the proof mass of 27.7 gram has a 1^{st} eigenfrequency of approximately 40 Hz, which coincides with the main excitation frequency of the cooler.

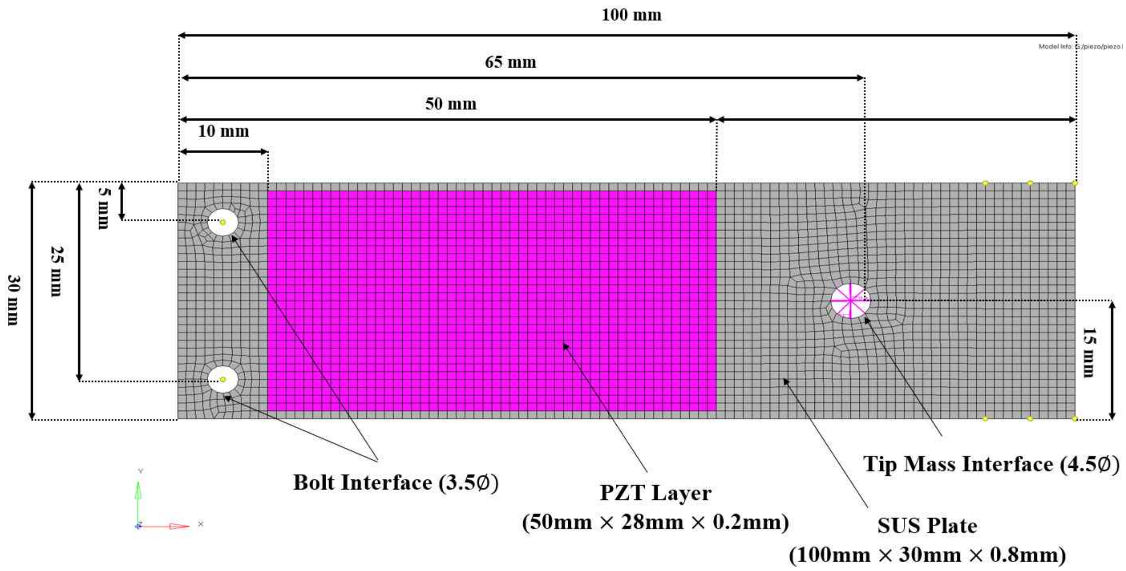

Fig. 15 Finite Element Model of Piezoelectric Harvester

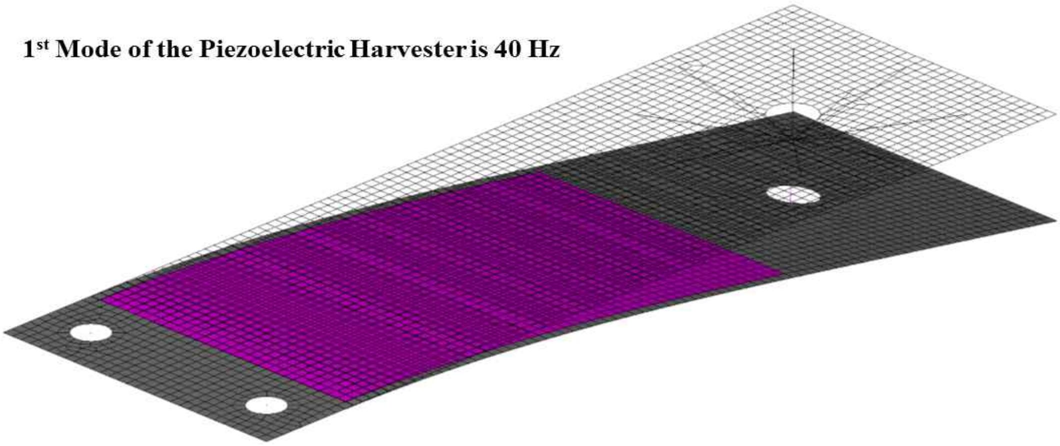

Fig. 16 1st Mode of Piezoelectric Harvester, 40 Hz coincided with Main Excitation Frequency of Cooler

2. Basic Characteristic

To investigate the basic characteristics of the manufactured piezoelectric harvester based on above design driver section, basic characteristic test was performed by using the test setup shown in Fig. 13. This test setup was mainly composed of a cantilever-type piezoelectric harvester, permanent magnets attached at both end sides of the piezoelectric harvester, a strain gauge, a electromagnetic-based vibration exciter, and laser displacement sensor (OptoNCDT 2300), respectively. In here, the strain gauge was dedicatedly employed in the test setup to obtain the induced force on the piezoelectric harvester. The strain data obtained from the strain gauge was converted to the force by multiplying the calibration factor which was preliminary determined from the initial calibration tests, thereby the force acting on the piezoelectric harvester can be achieved. In this test configuration, a sinusoidal signal was inputted to the electromagnetic-based vibration exciter; the piezoelectric harvester was thereby oscillated correspondingly due to electromagnetic force accompanied by the combination between the wound coil on the exciter and the magnets attached at the piezoelectric harvester. As a result, piezo-induced voltage, force, and displacement resulting from the oscillating movements of the piezoelectric harvester can be achieved.

Figure 14 shows the force–voltage relations of the piezoelectric harvester. The slope of the red-dotted line indicates the equivalent mechanical–electrical transformation factor α of the piezoelectric harvester and its value derived from the linear fitting curve is 0.105 N/V.

Figure 15 shows the force–displacement relations of the piezoelectric harvester. In this figure, the slope of the red-dotted line indicates the equivalent stiffness k of the piezoelectric harvester and the identified value is approximately 1.918 N/mm. Thereby, the expected 1st eigenfrequency of the piezoelectric harvester in combination with the proof mass, 27.7 grams, is 41.8 Hz and its value is nearly identical to the desirable frequency of 40 Hz. Meanwhile, the energy harvesting capability of the piezoelectric harvester is also affected by the mechanical damping, which can be obtained from the area enclosed by the hysteresis curve of the figure.

Thereby, we use the equivalent linearization method, wherein the non-linear stiffness and damping coefficients are translated into linear ones according to the energy-balancing principle, to calculate the damping coefficient of the harvester [48]. The following equation is used to determine the damping coefficient, c, of the piezoelectric harvester:

$$c = \frac{\triangle E}{\pi a_0^2} \sqrt{\frac{m}{k}} \tag{2-8}$$

where, $\triangle E$ is the area of the closed loop of the hysteresis curve, and a_0 is the displacement amplitude, m and k are the equivalent mass and stiffness of the piezoelectric harvester. Based on Eq. (2-8), the calculated damping coefficient of the piezoelectric harvester is 0.1728 Nsec/m.

Table 2 summarized the specifications for the piezoelectric harvester. In here, the basic characteristics, i.e. stiffness k, damping coefficient c, and mechanical-electrical transformation factor α, were obtained from basic characteristic tests addressed above. Otherwise, the other specifications were provided by the manufacturer.

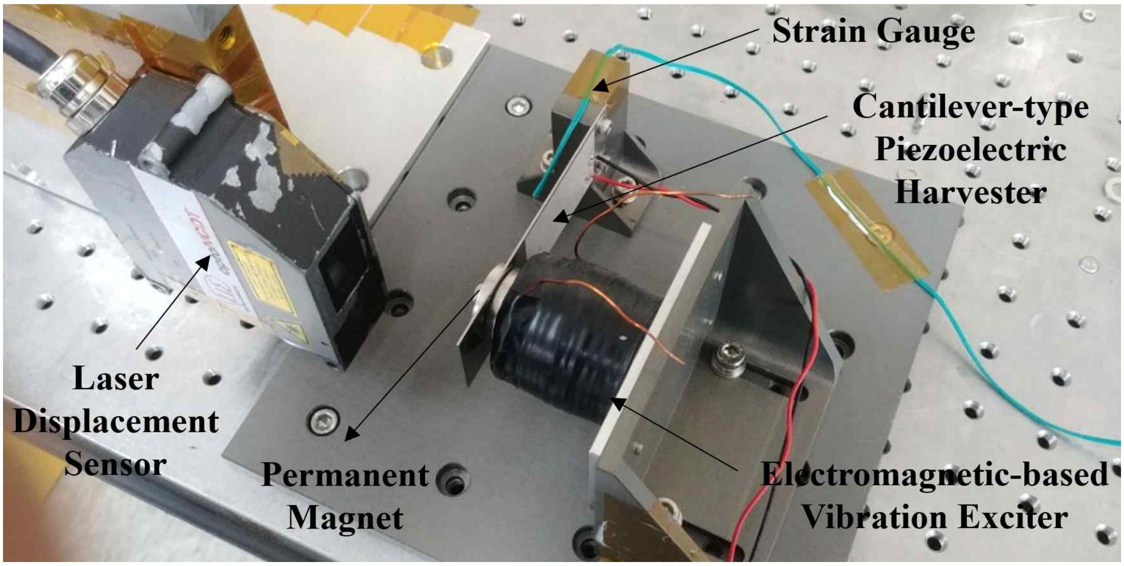

Fig. 17 Basic Characteristic Test Setup for Cantilever-type Piezoelectric Harvester

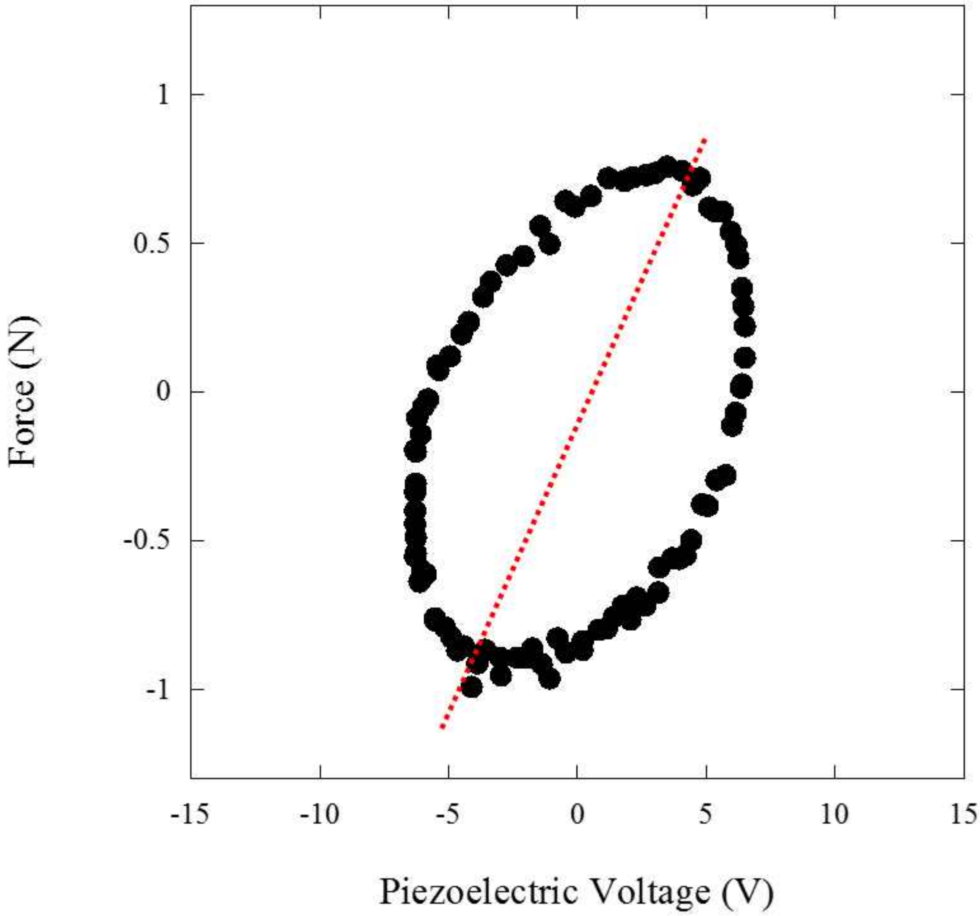

Fig. 18 Force-Voltage Relations of Piezoelectric Harvester

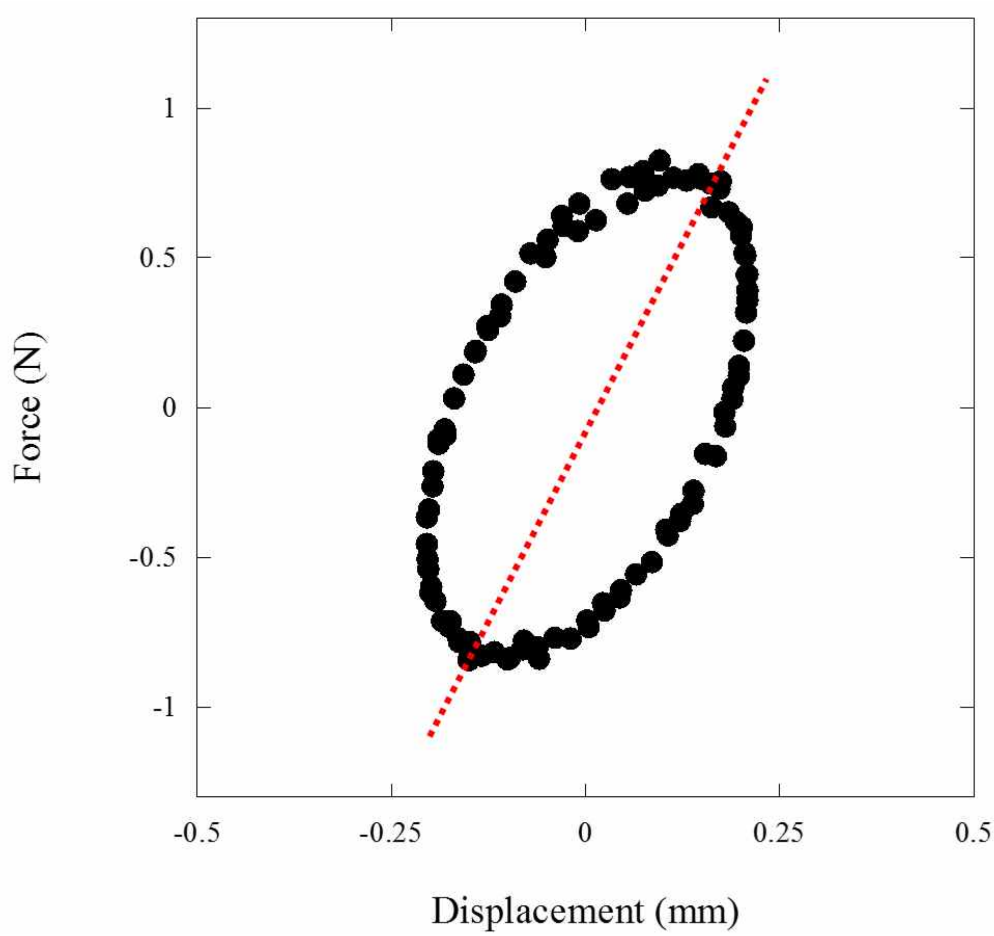

Fig. 19 Force-Displacement Relations of Piezoelectric Harvester

Table 2 Specifications of Piezoelectric Harvester

Property	Symbol	Values
Density (g/cm^3)	ρ	7.60
Curie temperature (℃)	T_c	260
Dielectric Constants	$\varepsilon_{33}^T/\varepsilon_0$	2,300
Dissipation Factor (%)	tgδ	1.5
Coupling Coefficients (%)	K_p	71.0
	K_t	51.0
	K_{31}	38.0
Frequency constants (m·Hz)	N_p	2,080
	Nt	2,040
	N_L	1,545
Mechanical Quality Factor	Q_m	80
Piezoelectric Charge Constants ($\times 10^{-12}$M/V)	d_{33}	450
	d_{31}	- 200
Piezoelectric Voltage Constants ($\times 10^{-3}$Vm/N)	g_{33}	22.1
	g_{31}	- 11.1
Elastic Constants ($\times 10^{-12}$m2/N)	S^E_{11}	13.8
	S^D_{11}	11.8
Capacitance (nF)	C_p	127.9
Equivalent Stiffness (N/mm)	k	1.918
Equivalent Damping Coefficient (Nsec/m)	c	0.1728
Mechanical Electrical Transformation Factor (N/V)	α	0.105

III. Performance Evaluation on Piezoelectric Harvester Level for S^{3}HI Strategy

A. System Configuration

1. Switching Design Driver

Guyomar et al. [1] proposed a non-linear harvesting technique, called synchronized switch harvesting on inductor (SSHI). The proposed SSHI technique has garnered considerable attention on account of its practical applicability and superiority in harvesting performance, such that various spawned research based on the SSHI technique have been reported. However, such addressed technique could only bring its advantages, provided that the amplitude of vibratory source is large enough to generate a piezo-induced voltage in which its level can overcome the threshold voltage accompanied by rectifying diodes and existing voltage in storage device, i.e. capacitor or battery. Hence, the micro-scale vibration has acted as an entry barrier so far for energy harvesting techniques.

To overcome above mentioned drawbacks of the conventional synchronized switching strategy, a novel switching strategy that exploits the full potential of the surging phenomenon has been proposed. This switching strategy locates the synchronous switch on a different position compared with the conventional SSHI, such that the inductor employed in the proposed strategy acts as a charge-pump unlike its role in the conventional SSHI in which the inductor only executes voltage-inverting actions at each switching instant. In the proposed surge-inducing switching scheme, the current from the piezoelectric element flows toward the inductor at the switching instant and the current is suddenly discharged right after the switching off. To investigate the feasibility of the surge-inducing synchronous switching harvesting strategy (S^{3}HI) proposed in this study, we established a numerical simulation model, as shown in Fig. 16. This model is mainly composed of a piezoelectric energy harvester, which is represented by a single degree of freedom (SDOF) model, and the harvesting circuits, i.e., circuits A, B, and C. In this model, Circuit A describes the standard harvesting circuit that does not implement any switching strategy; Circuit B is dedicated to the conventional SSHI strategy; Circuit C is dedicated to the surge-inducing switching strategy. In here, the circuit A and B are employed to assess the superiority of the proposed S^3HI strategy. In this model, m indicates the tip mass of the piezoelectric harvester, and the dashpot element, c, and the spring element, k, indicate the stiffness and the damping coefficient of the piezoelectric harvester, respectively. Moreover, the piezoelectric harvester comprises a mechanical-electrical transformer, α, that converts mechanical displacement, x, into an electrical potential, and the clamped capacitance, C_p. Here, the electrical potential is instantaneously accumulated in the capacitance, C_p, of the piezoelectric harvester. As a result, the piezoelectric voltage, V_p is generated across the piezoelectric harvester.

Moreover, the piezoelectric harvester is connected to the above mentioned harvesting circuits and can be categorized as followings: First, the piezoelectric harvester is connected to circuit A for the standard harvesting method, which simply includes a bridge diode, D, and a storage capacitor, C_s; Second, the piezoelectric harvester is connected to circuit B for the conventional SSHI strategy, which includes a bridge diode, D, an inductor, L_I, a switch, and a storage capacitor, C_s; Third, the piezoelectric harvester is connected to circuit C for the S^3HI strategy. In the last manner, the switch is located on a different position compared with circuit B, such that the inductor employed in circuit C acts as a charge pump unlike its role in the conventional SSHI strategy with circuit B, in which the inductor only executes voltage-inverting actions at the switching instants. Thus, circuit C positively utilizes the surge phenomenon of the inductor in combination with the dedicated circuit C. Thereby, the energy harvested from micro-scale vibrations can be effectively delivered to the storage capacitor. The details for proposed strategy are discussed in the following section.

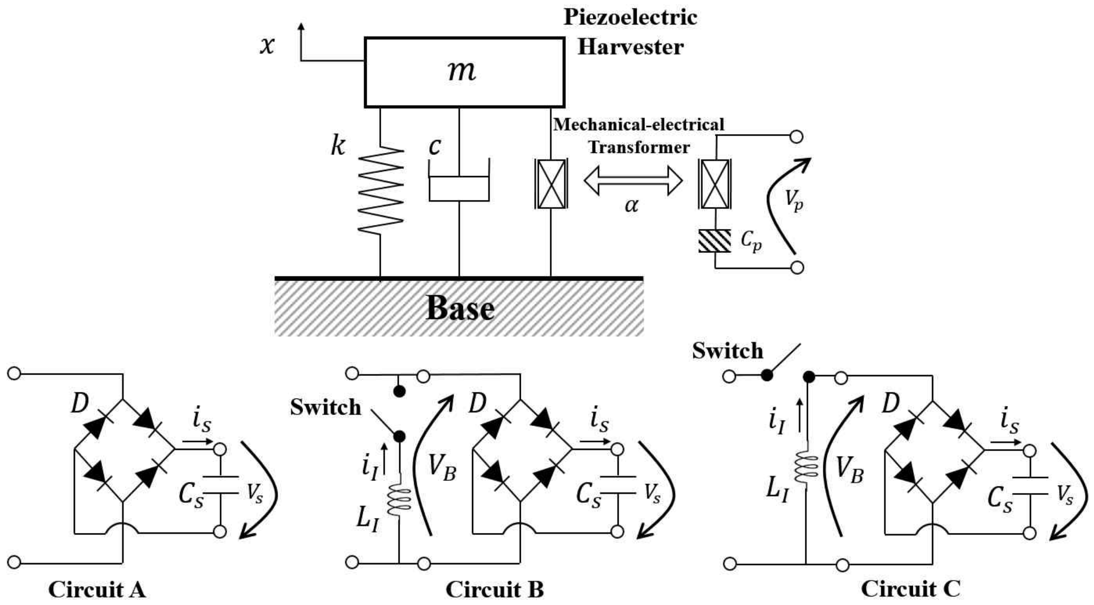

Fig. 20 SDOF Piezoelectric Energy Harvester with Harvesting Circuits, i.e., Circuit A for Standard Harvesting, Circuit B for Conventional SSHI [1], and Circuit C for S^{3}HI

2. Governing Equation of Motions

The equations of motion of the piezoelectric energy harvesting system are derived, based on Fig. 16, to assess the energy harvesting capabilities of the S^{3}HI. In this study, the micro-vibration source is just assumed to be a singular frequency and given by the following:

$$f = f_0 e^{iwt}, \tag{3-1}$$

where, f_0 and w denote the amplitude and excitation frequency of the vibration source, respectively. In this scheme, the governing equation of motion for the piezoelectric harvester can be defined as following:

$$m\ddot{x} + c\dot{x} + kx = f - \alpha V_p \tag{3-2}$$

$$i_p = \alpha\dot{x} - C_p \dot{V}_p \tag{3-3}$$

where, x and i_p denote the deflection of the piezoelectric harvester and the current out of the piezoelectric harvester, respectively. On the other hand, when the piezoelectric harvester is connected with the circuit C, the electrical dynamics can be categorized in two phases according to its switching on and off states. When the switch is turned on, the electrical current produced by the piezoelectric harvester starts to flow forward to an inductor such that a series connection of the piezoelectric capacitance, C_p, inductor, L_I, and switch resistance, R_{sw}, is established. Under such a series connection, the electrical equations of motion can be represented as follows:

$$L_I \ddot{Q}_p + R_{sw} \dot{Q}_p + C_p^{-1} Q_p = 0 \tag{3-4}$$

where, Q_p depicts the electrical charge in the piezoelectric capacitance, and its differential of $\dot{Q}_p$ depicts the electrical current, i_I, flowing through the $L_I - R_{sw} - C_p$ components. In this state, an induced electrical oscillation occurs in the circuit C for the specified switching duration. This means, that an electrical energy exchange between L_I and C_p occurs.

On the other hand, when the switch is turned off, a connection between L_I and C_s is implemented via the bridge diode. As a result, the inductor is subjected to a non-zero current at that instant, immediately after the switch is turned off. It means that the current, i_I, across the inductor cannot be instantaneously cancelled. This phenomenon results in extremely amplified surge voltage that can overcome the threshold voltage accompanied by the summation of the forward voltage drop and storage voltage, i.e. $V_{fw} + V_s$. Consequently, the harvested energy can flow toward the storage capacitor, C_s, via the bridge diode. In this state, the electrical equations of motion can be represented as follows:

$$L_I \ddot{Q}_s + R_D \dot{Q}_s + C_s^{-1} Q_s = 0 \tag{3-5}$$

where, Q_s depicts the electrical charge in the storage capacitor, C_s, and its differential, $\dot{Q}_s$, depicts the current, i_s, flowing toward C_s. In line with this state, the piezoelectric harvester can be regarded as an open-circuit condition until the switch is turned on. Therefore, the electrical current in the piezoelectric element cannot flow, namely $i_p = 0$, and the electrical charge, Q_p, stored in the piezoelectric element becomes constant provided that the switch is kept open. On this basis, the open-circuit piezoelectric voltage is derived and can be calculated from Eq. (3-2), as follows:

$$V_p = \frac{\alpha}{C_p} x + \frac{Q_p}{C_p} \tag{3-6}$$

In a previous study, SSHI [1] was controlled to be turned on at each maximum and minimum instances of the piezoelectric deflection. Furthermore, the switch is controlled to be turned off after a short duration, τ, and its duration can be optimally tuned to have the greatest energy harvesting capability. The optimal τ can be expressed as a half-electrical oscillation period accompanied by the inductor, L_I, and piezoelectric capacitance, C_p. This strategy can be implemented by the following control law:

$$\text{Switch} = \text{on} \qquad \text{when } t_{on} = t_{|x_{\max}|}$$

$$\text{Switch} = \text{off} \qquad \text{when } t_{off} = t_{on} + \pi\sqrt{L_I C_p} \tag{3-7}$$

where, $t_{|x_{\max}|}$ indicates the time instant when the piezoelectric deflection, x, is maximum or minimum and $\pi\sqrt{L_I C_p}$ indicates the optimal switching duration, τ_{opt}. In this manner, the current flowing through the inductor, i_I, during τ_{opt} can be represented as a half-sine curve, as shown in Fig. 17.

On the other hand, to induce a surge phenomenon in S^3HI, a sudden transient current, i.e., $d\dot{Q}_p/dt$, should be taken provided that the current flows in the inductor, as can be seen in Eq. (3-4) and Fig. 18. Therefore, the switching duration, τ, should be shorter or longer than the optimal duration, τ_{opt}, shown in Eq. (3-7). Thereby, a switching duration factor, β, is multiplied to τ_{opt}. Here, the range of β is determined in advance from the trade-off simulation to be from 0.6–1.4, where the optimal value exists. This switching control strategy for S^3HI can be implemented as follows:

$$\text{Switch} = \text{on} \qquad \text{when } t_{on} = t_{|x_{\max}|}$$

$$\text{Switch} = \text{off} \qquad \text{when } t_{off} = t_{on} + \tau_{opt}\beta \tag{3-8}$$

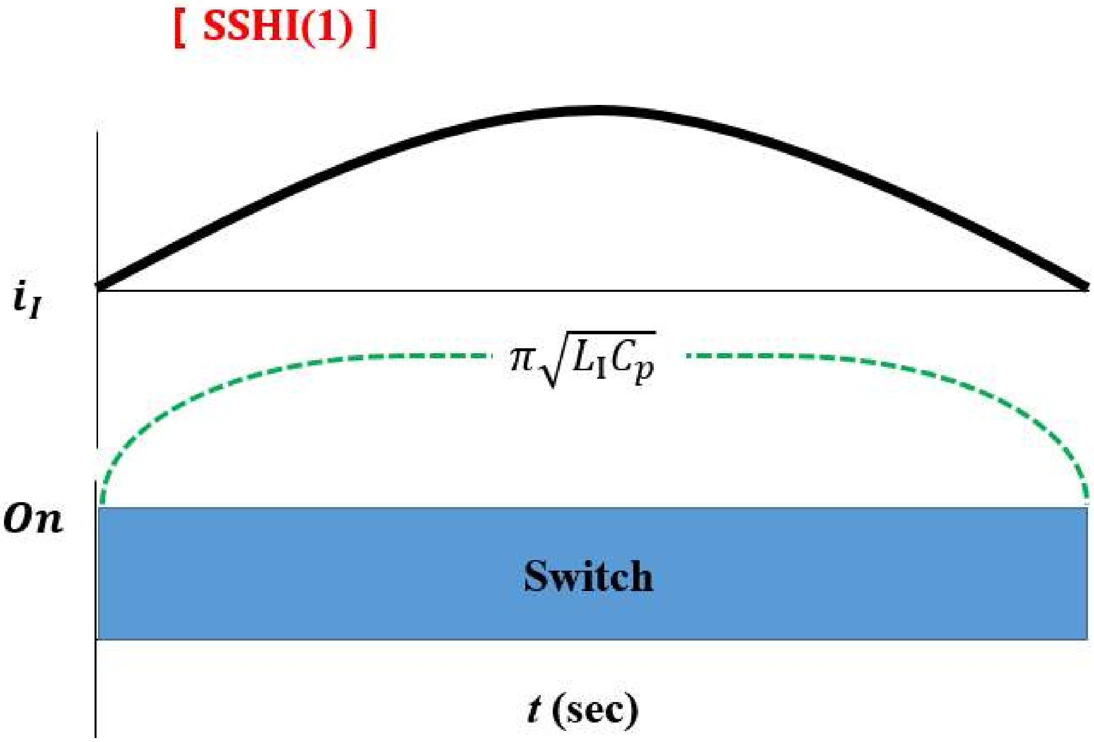

Fig. 21 Shape of Electrical Current i_I flowing though Inductor with respect to SSHI [1] Strategy

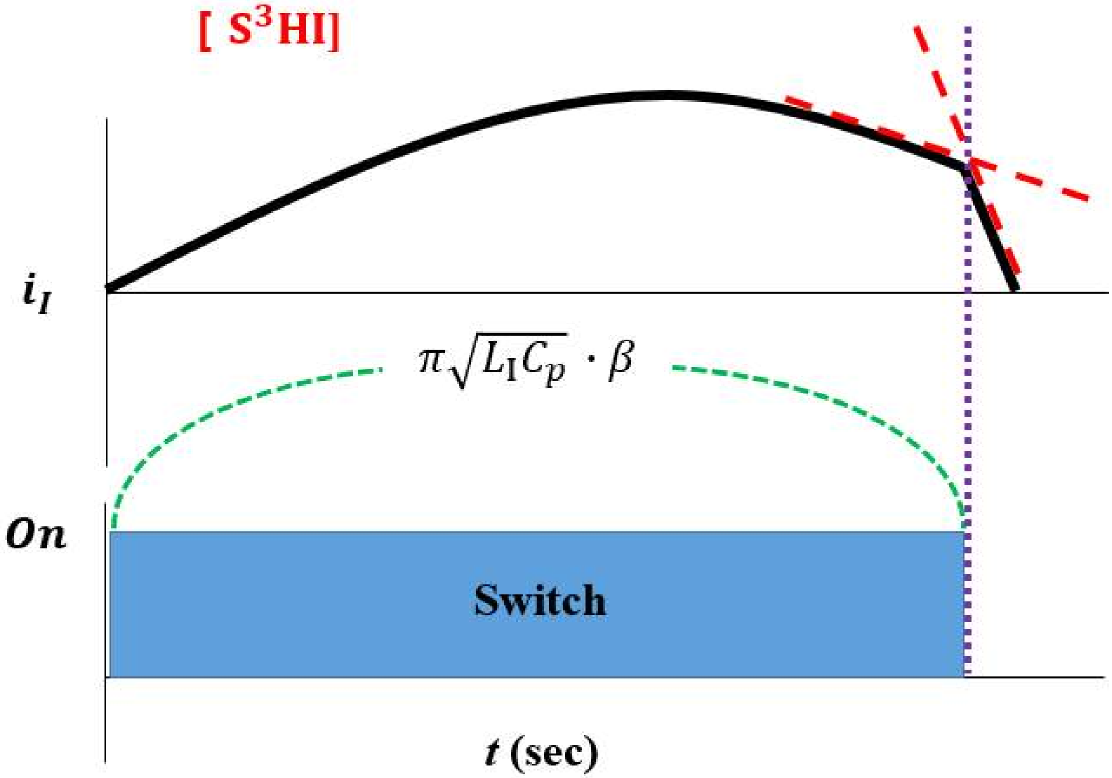

Fig. 22 Shape of Electrical Current i_I flowing though Inductor with respect to S^3HI Strategy

B. Numerical Simulation

1. Simulation Model Establishment

To investigate the feasibility of the surge-inducing synchronous switching harvesting strategy, namely S^{3}HI, proposed in this study, the theoretical equations in section 2 above are established in Matlab/Simulink, as shown in Fig. 19. This model includes mainly two modules, e.g. mechanical state-space model and electrical simulink model. Among these mechanical and electrical models, the electrical model can be extended to a subsystem as shown in Fig. 20. This electrical subsystem can be divided into mainly three categories, e.g. a switch controller, piezoelectric harvester, and electrical circuit. In here, the piezoelectric harvester can be simply modelled by a controlled current source block proportional to the mechanical velocity of the piezoelectric harvester $\dot{x}$ and the mechanical-electrical transformer α [49]. The switch controller determines the switching signal with regard to the switching control schemes defined in Eqs. (3-7) and (3-8) for SSHI and S^{3}HI. This switching controller can be modeled, as shown in Fig. 21, and the desirable switching duration with respect to the switching control scheme, i.e. SSHI or S^{3}HI, can be adjusted by using the off-delay block. The switching trigger signal determined from switching controller is then moved toward the electrical circuit. Figures 22, 23, and 24 show circuit A, B, and C, respectively. In here, standard harvesting circuit shown in Fig. 22 is simply designed with the bridge diode, the storage capacitor and the load resistor, respectively. Otherwise, circuits B and C for SSHI and S^{3}HI additionally employ the switch and inductor to exploit the full potential of the inductor, although each circuit places the switch on a different position due to different harvesting mechanism, as addressed in above section.

Table 3 summarizes the specifications of the electrical parts used in the numerical simulations. In this table, the values for inductor L_I, switch resistance R_{sw}, storage capacitance C_s, forward voltage drop of the bridge diode V_{fw}, and diode resistance R_D are based on the data sheets, because these components are all commercial products and will be applied to the circuit design (More details will be described in next section). Among given parameter values, it can be noted from the piezoelectric capacitance, $C_p = 127.9$ nF, and inductance, $L_I = 225$ mH, that the optimal switching duration τ_{opt} calculated using the abovementioned Eq. (3-7), $\pi\sqrt{L_I C_p}$, is approximately 530 μs. Thus, the calculated switching duration of 530 μs is used for the SSHI strategy to obtain the optimal harvesting performance. Otherwise, the optimal switching duration for the S^3HI is still unknown since a switching duration factor, β, should be considered to induce a surge phenomenon as the study intended. The optimal value of β will be discussed in the next simulation result section.

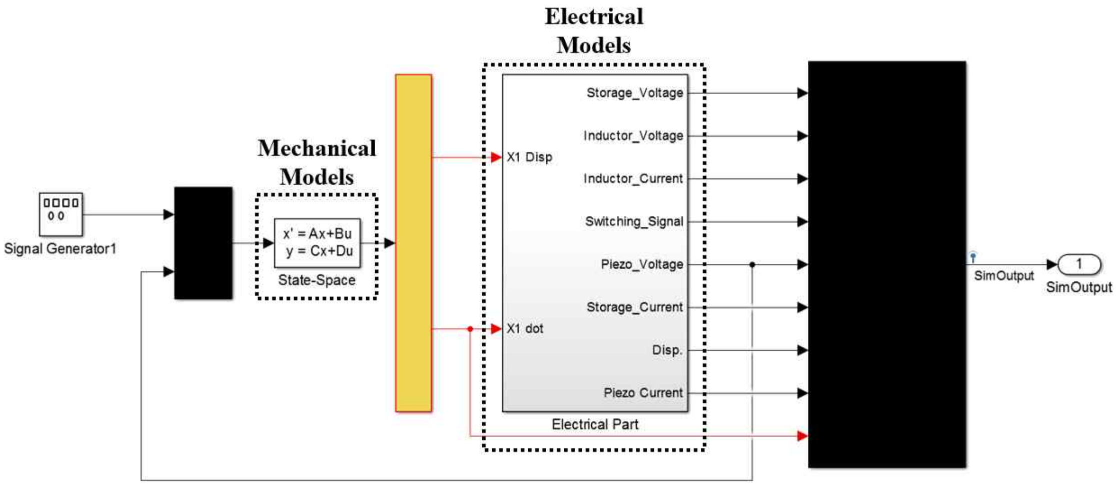

Fig. 23 Top-level Matlab/Simulink Model of Piezoelectric Harvester

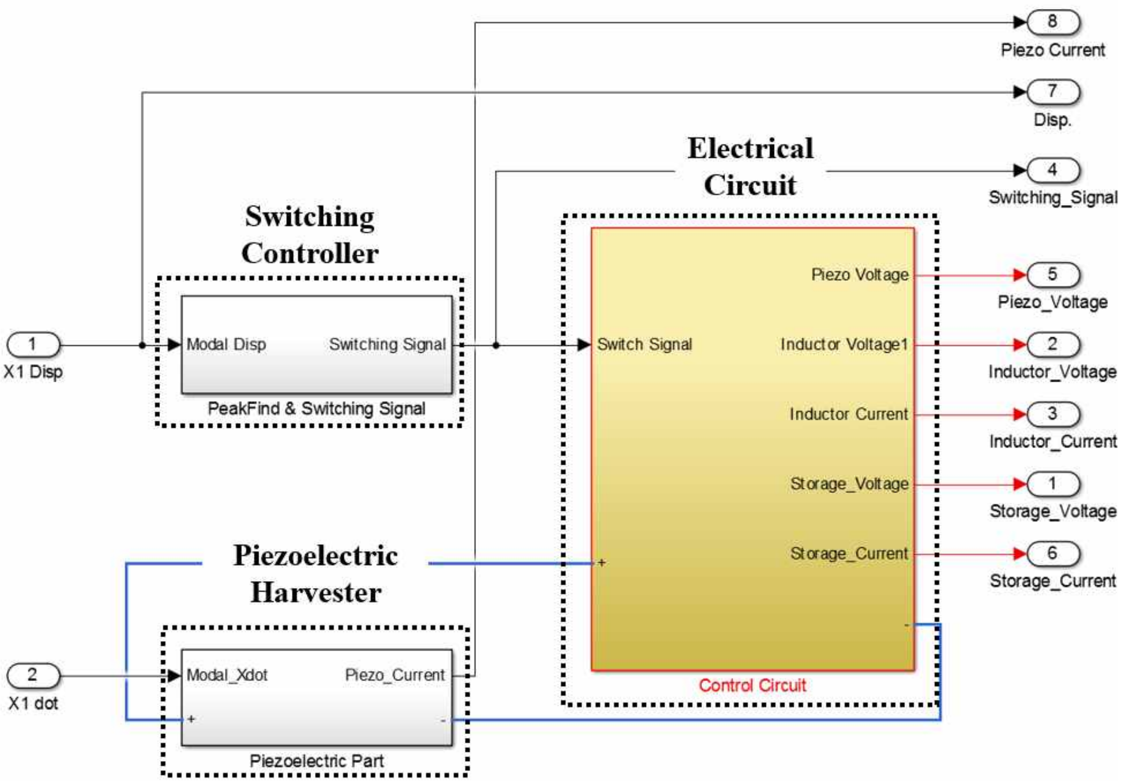

Fig. 24 Electrical Subsystem Model composed of Switching Controller, Piezoelectric Harvester, and Control Circuit.

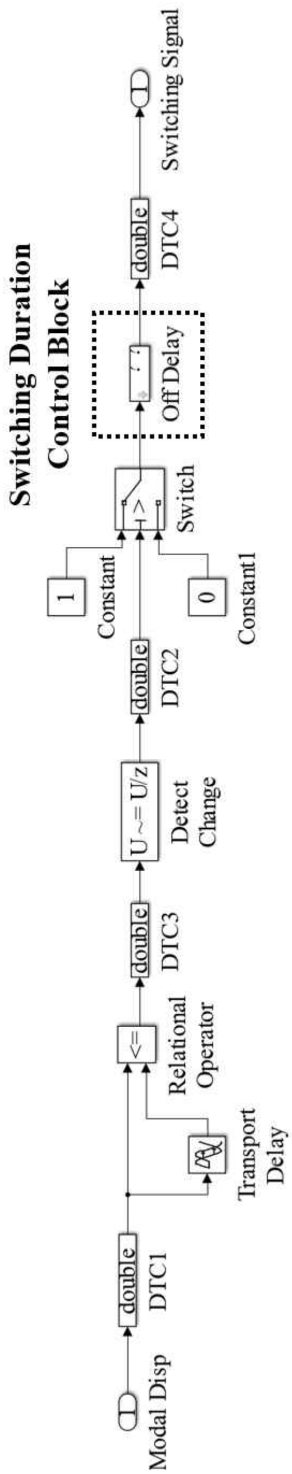

Fig. 25 Switching Controller Subsystem Block

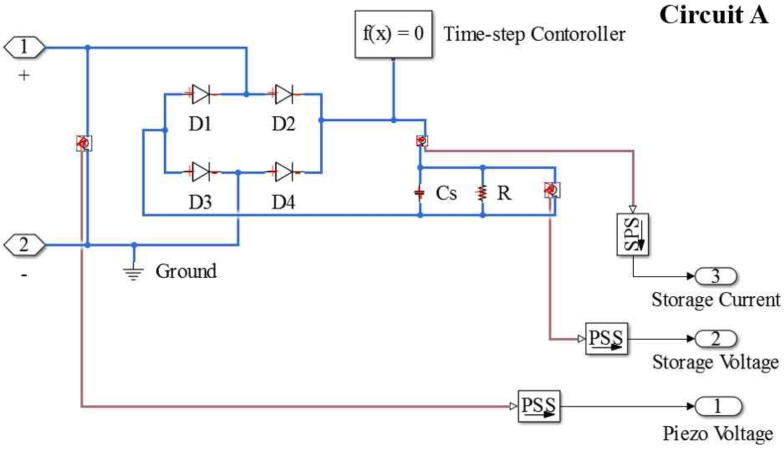

Fig. 26 Circuit A Model for Standard Harvesting Strategy

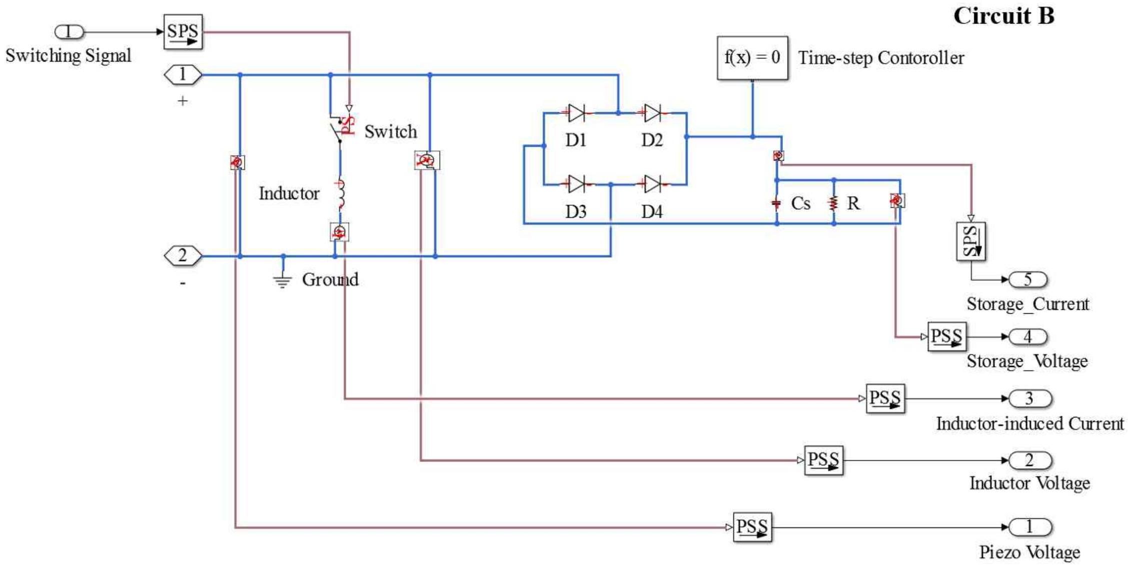

Fig. 27 Circuit B Model for SSHI Strategy

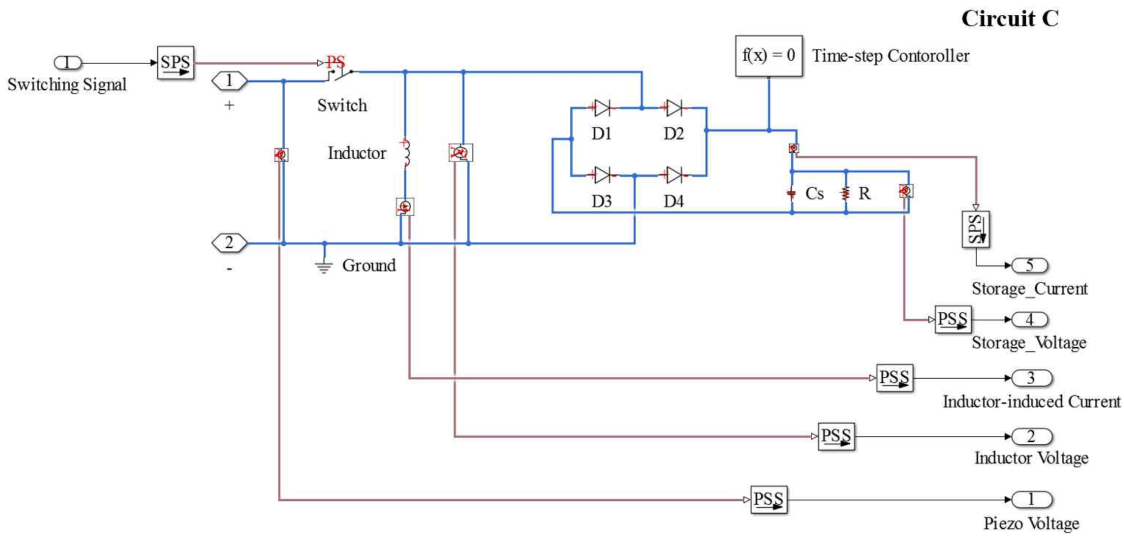

Fig. 28 Circuit C Model for S^3HI Strategy

Table 3 Specifications of Electrical Parts used in Simulation

Property	Symbol	Values
Inductor	L_I	225 mH
Bridge Diode Forward Voltage Drop	V_{fw}	0.96 V
Bridge Diode Resistance	R_D	0.3
Storage Capacitance	C_s	4.7 uF
Switch Resistance	R_{sw}	15

2. Simulation Result

To assess the feasibility of the S^3HI strategy, a numerical simulation was performed based on the equations of motion shown above. The parameters used in the simulation are summarized in Table 3. The external force, f , was defined as 0.5 N with an excitation frequency of 40 Hz, which corresponds to the major excitation frequency of the cooler.

Figure 25 shows the maximum storage voltage for circuit C that is dedicated to the S^3HI strategy. In the simulation, the switching duration factor, β, is selected as a function of the harvesting performance. In this figure, it can be seen that circuit C shows the highest performance at a switching duration factor of β = 0.67, which is relatively shorter than the optimal switching duration for the SSHI strategy as referred in Eq. (3-8). These facts indicate that circuit C with the S^3HI strategy assures an optimal performance when the switching duration is relatively shorter than a half electrical oscillation period, as mentioned above, in contrast to circuit B whose performance is significantly degraded by a shorter or longer switching duration [1]. On the other hand, S^3HI strategy shows slightly asymmetric trends between shorter and longer switching durations. When the switching duration factor is shifted out toward the relatively lower value than the optimal β, i.e. β = 0.4, the maximum storage voltage is 5 V. Otherwise when the switching duration factor becomes higher than the optimal β, i.e. β = 1, the maximum storage voltage is 4.6 V. This performance discrepancy is caused by dissipated energies into the switch resistance during switch on states, meaning that as the switching duration becomes longer, more electrical energy becomes dissipated in the switch resistance, R_{sw}. As a result, it can be said that the decrease trend with longer switching duration factors is much steeper than the shorter case. Hence, the shorter case can guarantee unsusceptible harvesting performance at lower switching duration factors.

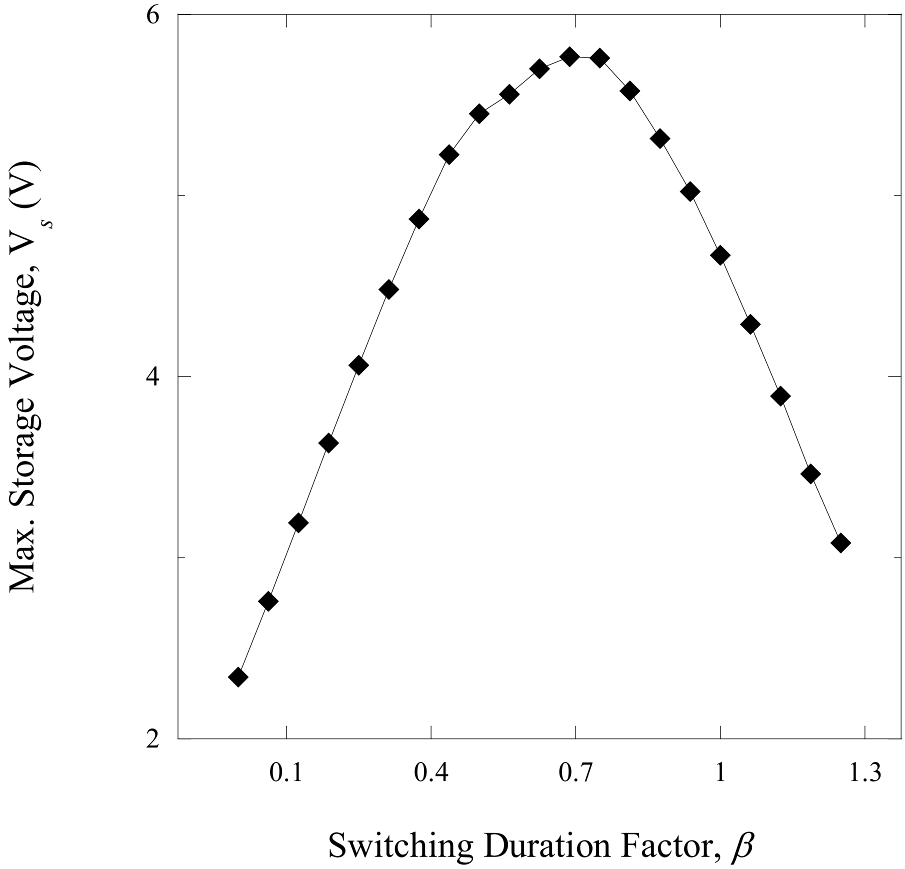

Fig. 29 Max. Storage Voltage for S^3HI Strategy as a Function of Switching Duration Factor

The overall and close-up views of time histories of S^{3}HI strategy for displacement, x, piezo-induced voltage, V_p, and storage voltage, V_s, for S^{3}HI, with respect to variations of the switching duration factor, β, are shown in Figs. 26 and 27. As can be observed in Fig. 26, the trends of x, V_p, and V_s, with variations in β, exhibit an entirely different behavior because the affection of $L_I - R_{sw} - C_p$ induced electrical oscillations on the system dynamics is different with regard to variations of β value. On the other hand, it can be clearly observed in the close-up view of Fig. 27 that the trends of maximum $|x|$ and $|V_p|$ are opposite. As indicated in Eq. (3-7), the condition, e.g. $\beta = 1$, corresponds to the optimal switching duration, τ_{opt}, of the conventional SSHI strategy and results in the half electrical oscillations. Thus, the piezoelectric voltage, V_p, is the highest compared with those in the other conditions, where relatively shorter or longer values of β impose detrimental effects on amplitudes of V_p. However, as can be seen in Eq. (3-2), V_p also acts as a control force that restrains the mechanical displacement, x, of the piezoelectric harvester. Hence, a higher V_p inevitably results in decreasing the amplitude of x, commonly designated as the vibration suppression effect but at a cost of energy harvesting capability. In a previous study, there was an effort to minimize such a vibration suppression effect resulting from switching actions, while keeping the vibration amplitudes as high as its original level. For example, Makihara et al. [50] reported an SSHI-based switching pause strategy that skipped several switching instances to minimize the suppression effect of the $L_I - R_{sw} - C_p$ -induced electrical oscillations. Hence, they could achieve a relatively greater harvesting performance than the conventional SSHI. In this manner, the larger amplitude of x is always preferable because it is proportional to the current, i_p, from the piezoelectric harvester, by considering Eq. (3-3). Thus, a shorter or a longer switching duration than τ_{opt} is preferable in terms of energy harvesting performance. This fact is quite an opposite trend when compared with the conventional SSHI strategy, which only guarantees optimal harvesting performance when $\beta = 1$, commonly designated as τ_{opt}. In this context, it can be noticed that the case with $\beta = 0.67$ shows the highest storage voltage compared with that of the other cases. In fact, its maximum voltage is 9.33V and its level is approximately 1.6 times higher than that when the case is $\beta = 1$. Therefore, in this study, $\beta = 0.67$ is defined as an optimal value for the S^3HI strategy. Hereafter, S^3HI with $\beta = 0.67$ is referred to as an optimal S^3HI.

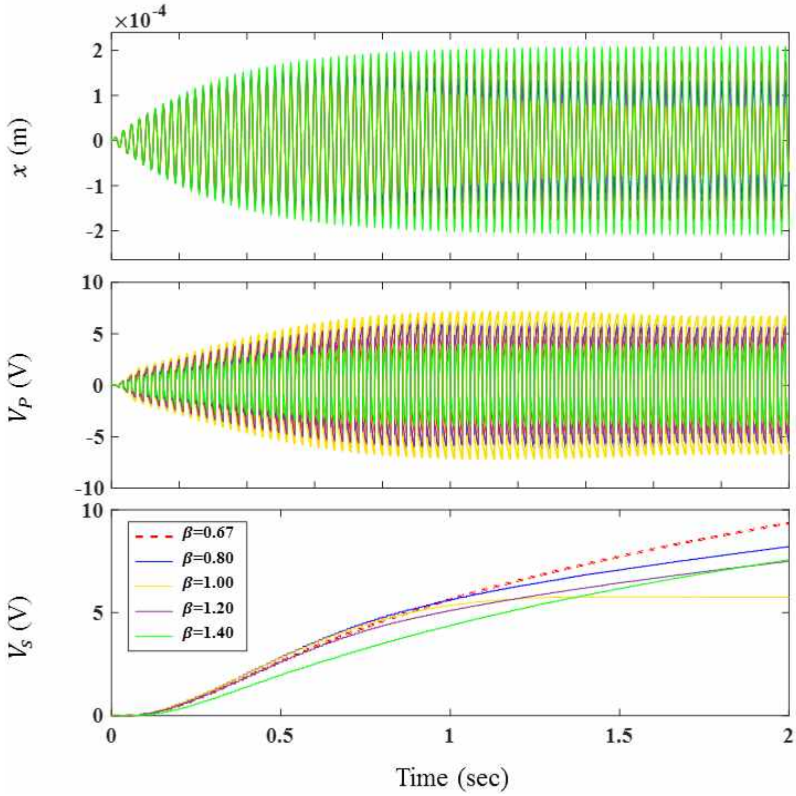

Fig. 30 Overall Time Histories of Displacement, x, Piezo-induced Voltage, V_p, and Storage Voltage, V_s, for S^{3}HI with respect to Variations of β

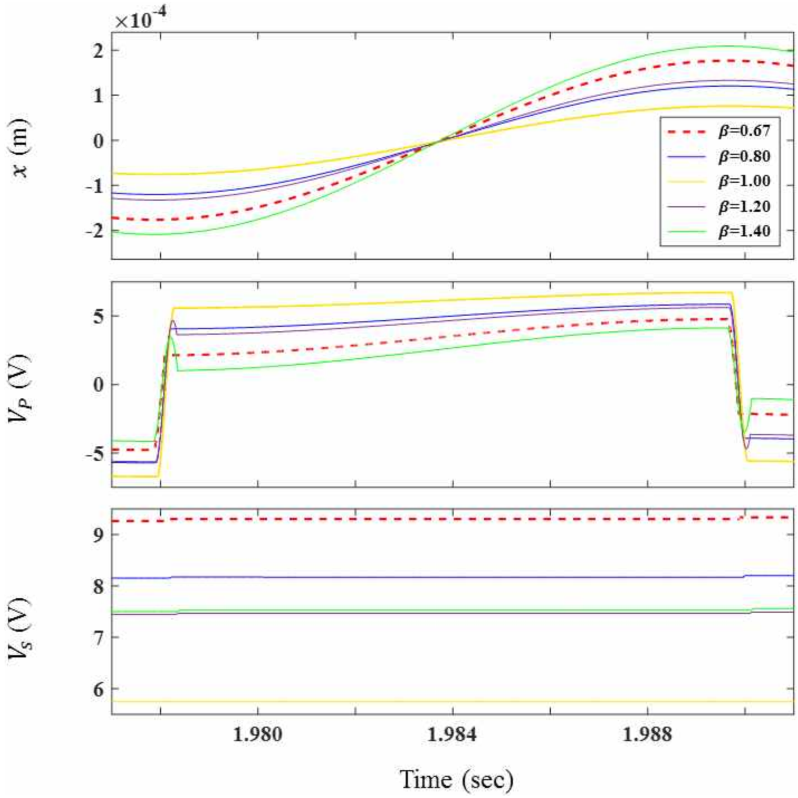

Fig. 31 Closed-up Time Histories of Displacement, x, Piezo-induced Voltage, V_p, and Storage Voltage, V_s, for S^{3}HI with respect to Variations of β

The root-mean-square of displacement, x_{rms}, and maximum storage voltage, V_s, with respect to variations of β are shown in Fig. 28. These values of x_{rms} and V_s are based on above Fig. 26. In this figure, it can be seen that the aforementioned x_{rms} and V_s generally show similar tendencies. For example, x_{rms} and V_s show the lowest values under the condition that $\beta = 1$. Otherwise, those values gradually increase when the condition becomes $\beta < 1$ or $\beta > 1$. This is because of the different impacts of the $L_I - R_{sw} - C_p$-induced electrical oscillation on the system dynamics according to the value of β. On the other hand, it can be noticed that the increasing trends of V_s between $\beta < 1$ and $\beta > 1$ are quite different. Under the condition of $\beta < 1$, x_{rms} and V_s gradually increases as β decreases. However, when $\beta > 1$, V_s reaches a saturation point even if the amplitude of x_{rms} constantly increases. Because the energy dissipated in the switch resistance, R_{sw}, also increases as the switching duration increases. Hence, a relatively shorter switching duration with the condition $\beta < 1$ is preferred for the S^{3}HI strategy.

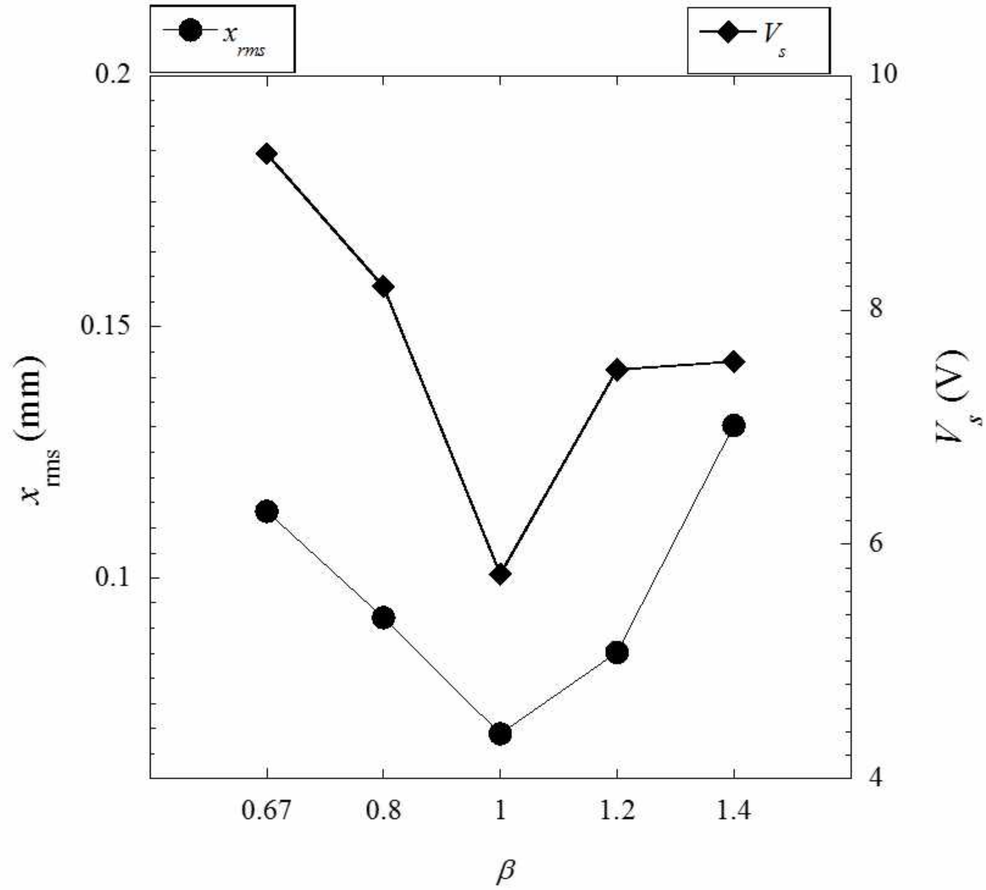

Fig. 32 Displacement x_{rms} and Storage Voltage V_s Relations with respect to Variations of β of S[3]HI Strategy

The close-up view of the time histories of the standard, optimal SSHI, and optimal S^3HI for displacement, x, piezoelectric voltage, V_p, inductor-induced voltage, V_B, current across the inductor, i_I, storage voltage, V_s, current forwarded to the storage capacitor, i_s, and switch, are shown in Fig. 29. In this simulation, the optimal SSHI strategy is based on Eq. (3-7). Otherwise, the optimal S^3HI strategy is based on Eq. (3-8), respectively. In this figure, the occurrence of the electrical current flow, i_s, directed to the storage capacitor, C_s, reveals that V_B exceeds the threshold voltage accompanied by the diode forward voltage drop, V_{fw}, and existing storage voltage, V_s, i.e., $|V_B| > V_{fw} + V_s$. Consequently, the existence of i_s means that the storage capacitor is being charged. In this result, the overall dynamics for each of the strategies are compared before and after the switching actions. In the case of the displacement, x, the standard case shows the highest value compared to the other cases because no negating effect on the vibration amplitude exists, which differs from those of the optimal SSHI and S^3HI. However, its storage voltage, V_s, is the lowest because of the small vibration level. In the cases of the optimal SSHI and S^3HI, the trends of V_B are quite different. In the case of optimal SSHI, its electrical dynamics during the switch on state can be represented by Eq. (3-4) and voltage V_B becomes inverted as much as the inversion factor of the inductor [51]. When the switch is turned-off, the connection between the inductor, L_I, and storage capacitor, C_s, is broken. Thus, V_B is only affected by the voltage going out of the piezoelectric element. During this state, V_B slightly increases by as much as $\alpha x / C_p$, as described in Eq. (3-6). If the absolute value of $|V_B|$ is larger than $V_{fw} + V_s$ as a result of the variations of x, the current, i_s, flows toward the storage capacitor, C_s. However, when V_s has sufficiently increased, $|V_p|$ cannot exceed $V_{fw} + V_s$, and i_s does not flow toward the storage capacitor, C_s. Thus, the storage capacitor can no longer be charged when using the optimal SSHI, as can be observed in Fig. 29. To utilize the optimal SSHI in the micro-scale vibration energy harvesting, a bigger value of the inversion factor of the inductor or a relatively larger vibration source is required. However, these alternatives could not be the proper technical solution because of limitations in the real application. On the other hand, in the case of optimal S^3HI, the current flow of i_s is observed, meaning that this strategy can charge the storage capacitor in compliance with the battery charging requirement, i.e., $|V_B| > V_{fw} + V_s$. In this strategy, an electrical potential coming out of the piezoelectric element directly affects the inductor as soon as the switch is turned on. Then, V_B increases as high as the level of V_p. Subsequently, a voltage inversion behavior occurs at a value of $0.67 \cdot \tau_{opt}$, which can be represented by Eq. (3-4). Right after the switch-off state, the inductor is not affected by the voltage coming out of the piezoelectric element. However, it is still subjected to a closed-circuit condition with the storage capacitor via the bridge diode in which its electrical dynamics can be represented by Eq. (3-5). In this state, a sudden transient current that results in significant slope changes of i_I is observed. This transient current flow lasts during $\triangle t$ until it becomes zero, because the current flowing through the inductor cannot be instantaneously canceled. Consequently, highly boosted surge voltage induced by a sudden transient current in the inductor occurs, resulting in a high voltage that complies with the charging requirement $|V_B| > V_{fw} + V_s$. In this manner, i_s can flow forward to the storage capacitor; then it can be charged.

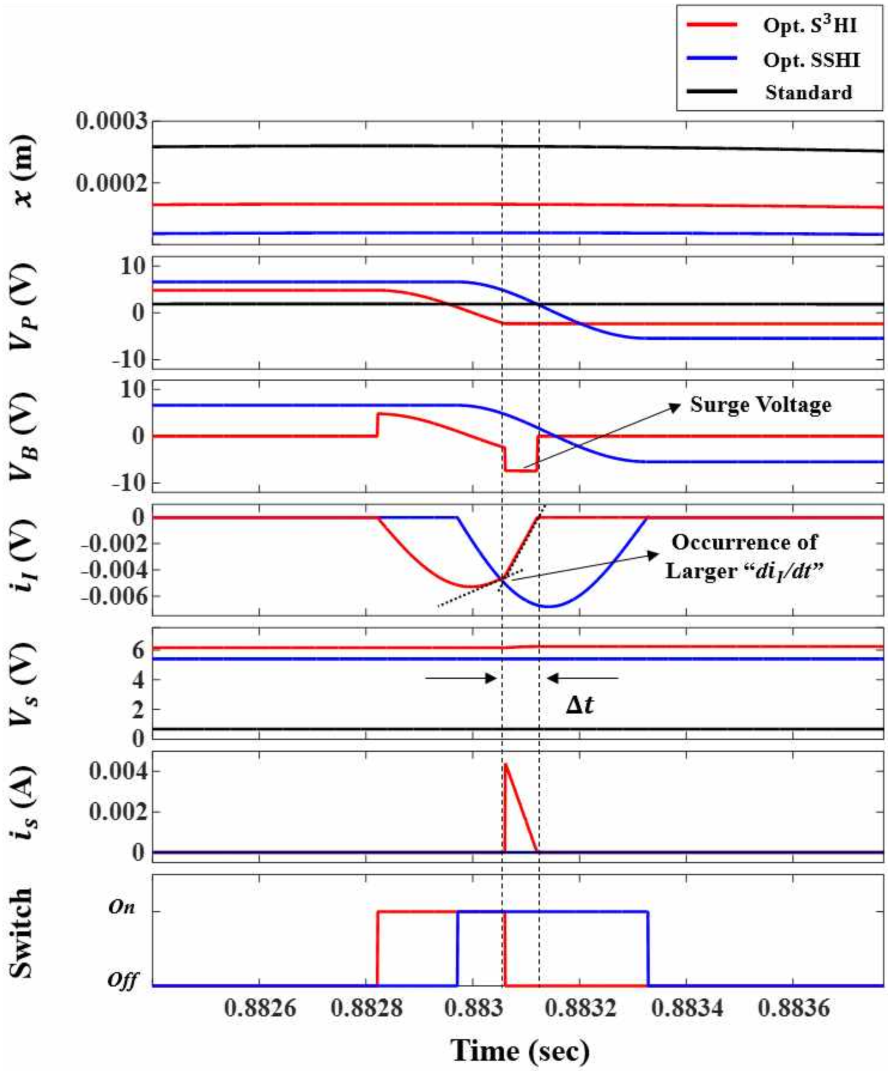

Fig. 33 Closed-up Time Histories of Standard, Optimal SSHI, and Optimal S^{3}HI Strategies for x, V_p, V_B, i_I, V_s, i_s and Switch, respectively

The time histories of i_p and V_p for the standard, optimal SSHI and S^{3}HI strategies are shown in Fig. 30. In these results, an order of 5 magnitude is multiplied to i_p for an easier comparison with V_p. In the case of the standard strategy, it has the highest i_p compared with the other cases because no switching action that suppresses the vibration amplitudes exists. However, its voltage level is the lowest and the phase of i_p and V_p do not match each other. Thus, no electrical coupling effect can be expected in this configuration. In contrast, the phases of i_p and V_p for optimal SSHI and S^{3}HI are well matched because of the synchronized switching action. Hence the electrical coupling effect occurs. However, because of the difference in the control scheme, each strategy has different amplitudes of i_p and V_p. As mentioned above, the switching duration for the optimal SSHI is defined as τ_{opt}, which is half the electrical oscillation periods accompanied by the inductor, L_I, and piezoelectric capacitance, C_p. This control scheme holds the switch relatively longer than the optimal S^{3}HI, such that the amplitude of the inversion voltage in the inductor becomes relatively higher than that of the optimal S^{3}HI. This larger inversion voltage results in a larger piezoelectric voltage, V_p. However, the larger V_p inevitably largely suppresses the vibration amplitudes as well. Thus, the amplitude of i_p with the optimal SSHI is relatively lower than that of the optimal S^{3}HI.

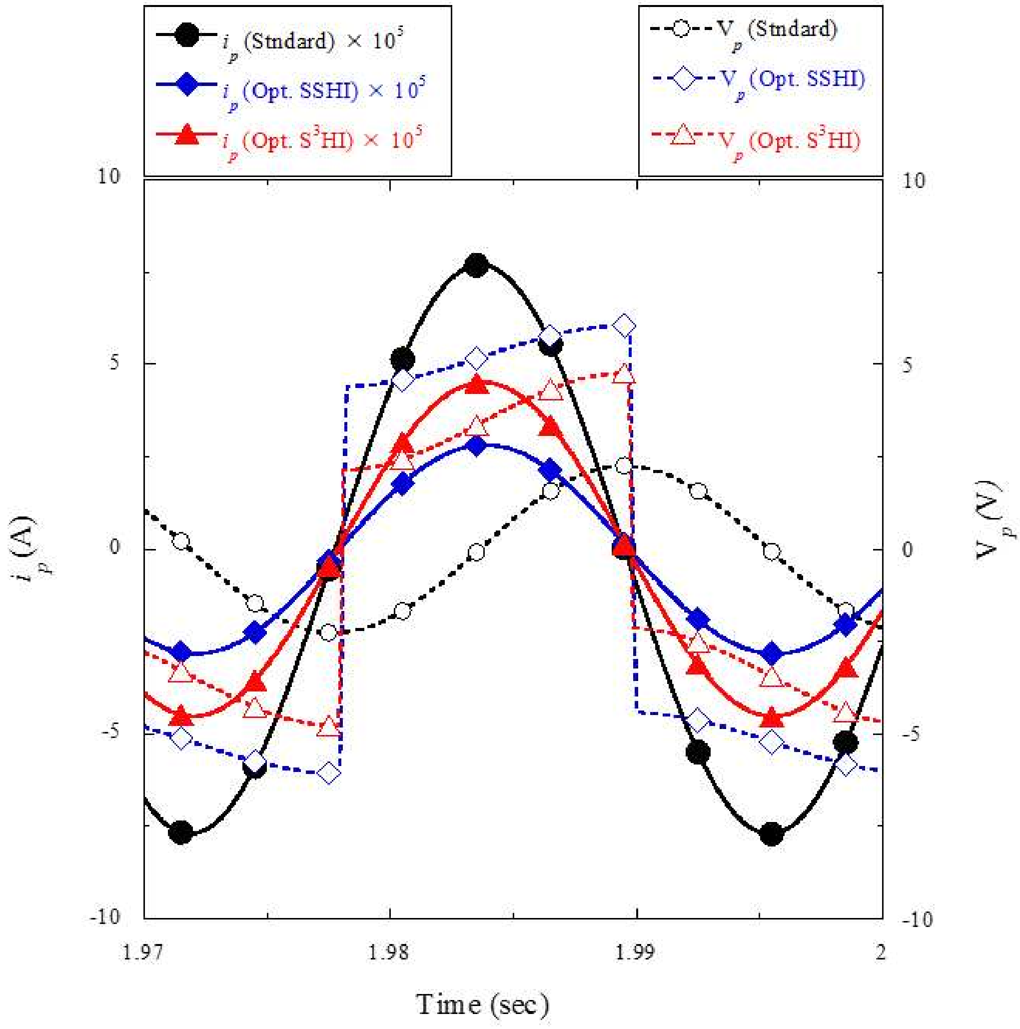

Fig. 34 Time Histories of i_p and V_p for Standard, Optimal SSHI and Optimal S^3HI Strategies.

The piezo-induced energy for standard, optimal SSHI, and optimal S^{3}HI strategies are shown in Fig. 31. Here, the piezo-induced energy can be calculated by multiplying i_p and V_p; its result is based on Fig. 30. As can be seen in the former figure, the standard case has a negative and positive energy because the phases of i_p and V_p are not electrically coupled. On the other hand, the optimal SSHI and S^{3}HI only have positive energy that can be entirely harvested. However, these strategies exhibit different energy levels because of the quantitatively different negating effects of the switching action. Consequently, based on this figure, it can be said that the switching action of the optimal S^{3}HI is less detrimental on the vibration amplitudes compared with that of the optimal SSHI. For example, the maximum instantaneous energy of the S^{3}HI is 167 uW and its level is approximately 112% higher than that of the optimal SSHI. Thus, it can be concluded that the optimal S^{3}HI guarantees much higher energy harvesting performance from the piezoelectric element.

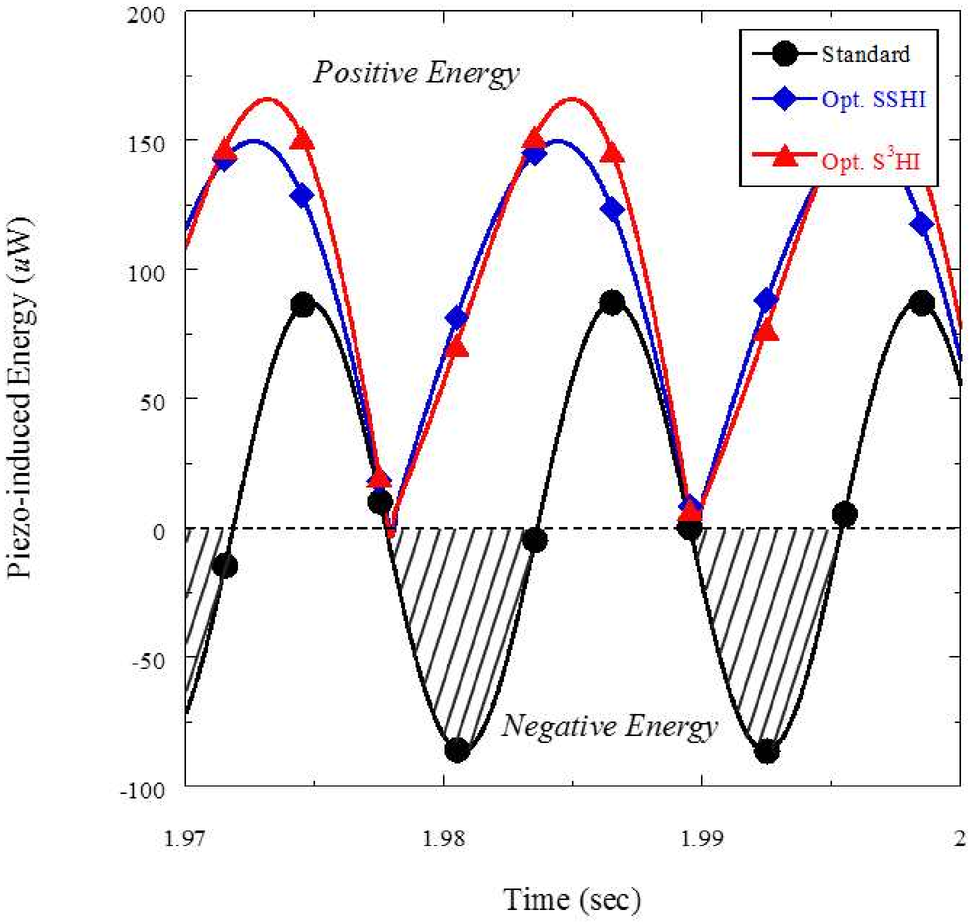

Fig. 35 Piezo-induced Energy for Standard, Optimal SSHI and Optimal S^3HI Strategies.

The accumulated energy in electrical resistance, P_{ce}, inductor, P_{in}, and storage capacitor, P_{sc}, for optimal SSHI and S^{3}HI are shown in Fig. 32. In practice, P_{ce} denotes the energy loss in the circuit resistance, i.e., R_{sw} and R_D. These addressed temrs can then be calculated from following.

$$P_{ce} = \frac{1}{t-0}\int_0^t [(i_I^2(t)R_{sw}) + (i_s^2(t)R_D)]dt \tag{3-9}$$

The energy absorbed in the inductor, P_{in}, can be calculated as

$$P_{in} = \frac{1}{t-0}\int_0^t V_B(t)i_I(t)dt \tag{3-10}$$

The net energy harvested in the storage capacitor, P_{sc}, can be calculated as,

$$P_{sc} = \frac{1}{t-0}\int_0^t V_s(t)i_s(t)dt \tag{3-11}$$

In the aforementioned figure, it can be seen that the optimal SSHI has a relatively higher P_{ce} compared with that of the optimal S^{3}HI. This fact means that the optimal SSHI dissipates considerably more energy into the resistances because of the relatively longer switching duration. This also explains why the condition $\beta > 1$ has a saturation point for V_s even if the amplitude of x_{rms} becomes constantly higher. Here, the longer switching duration also results in the energy being absorbed by the inductor, P_{in}. In this manner, the optimal SSHI has a higher P_{in} compared with the optimal S^{3}HI. Accordingly, all the absorbed energy by the inductor is utilized to invert the voltage. However, when considering the net energy harvested in the storage capacitor, P_{sc}, the accumulated energy in the optimal SSHI for 2 s is approximately 30 uW. Otherwise, its value is 3.8 times lower than that of the optimal S^{3}HI. If a considerably longer simulation time is considered, the above value of 3.8 could considerably increase because the surge phenomenon of the optimal S^3HI is still striving to harvest the energy, as can be seen in Fig. 32. For instance, the slope of P_{sc} is maintained at the end of simulation time. Otherwise, the slope of P_{sc} for the optimal SSHI is saturated from approximately 1.3 s onward. Accordingly, no energy harvesting performance can be expected with the optimal SSHI. From these facts, it can be said that the S^3HI strategy is considerably powerful for energy harvesting.

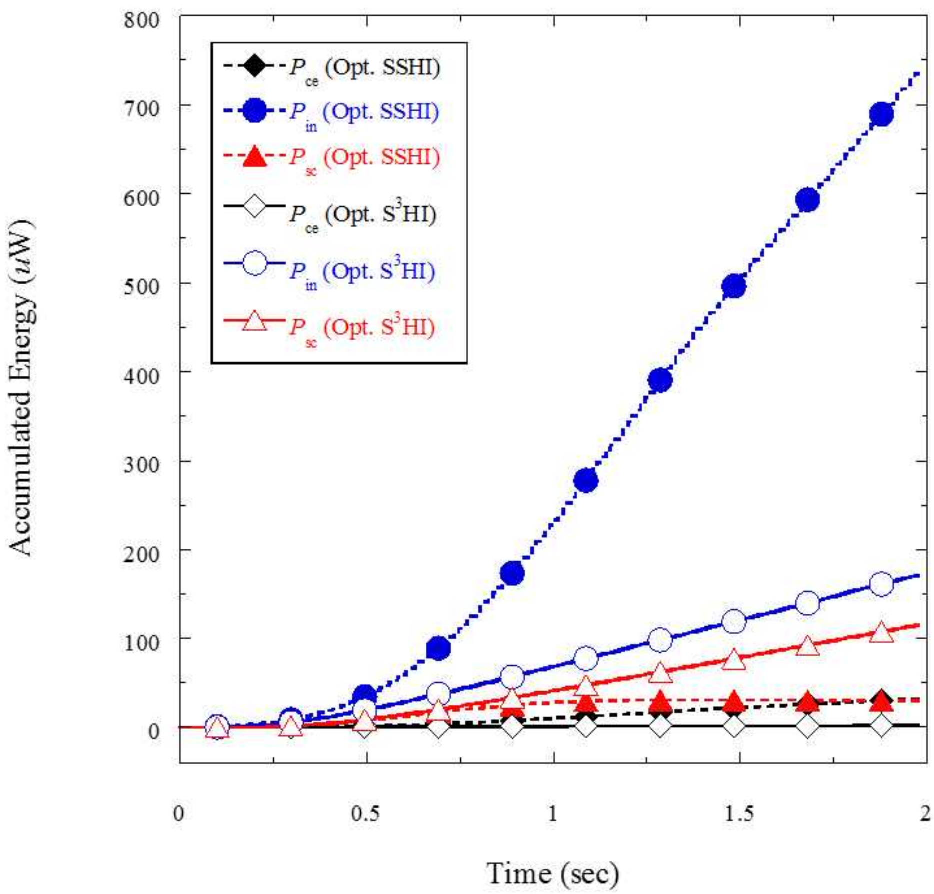

Fig. 36 Accumulated Energy in Electrical Resistance, P_{ce}, Inductor, P_{in}, and Storage Capacitor, P_{sc}, for Optimal SSHI and Optimal S^{3}HI.

The maximum storage voltages of the standard, optimal SSHI, and optimal S^3HI for 2 *s*, as a function of the excitation force level, are shown in Fig. 33. In this figure, it can be noticed that the standard case cannot charge the storage capacitor at a vibration level of 0.006 N. However, in the case of the optimal SSHI, it can commence charging the storage capacitor from a smaller value of 0.002 N, and its charging performance is considerably higher compared to that of the standard case. However, it should also be noted that the optimal SSHI still has ineffective vibration ranges under a force condition smaller than 0.002 N. This means that no energy harvesting capability can be expected below the given range. However, the optimal S^3HI strategy can guarantee energy harvesting capability even in such a small vibration range, i.e., excitation force level < 0.002, in contrast with those of the other cases. In addition, it can be noticed that the difference of the storage voltage between the optimal SSHI and optimal S^3HI becomes larger as the vibration level increases. Consequently, these indicate that the optimal S^3HI is effective not only under small vibration levels but also under high vibration levels.

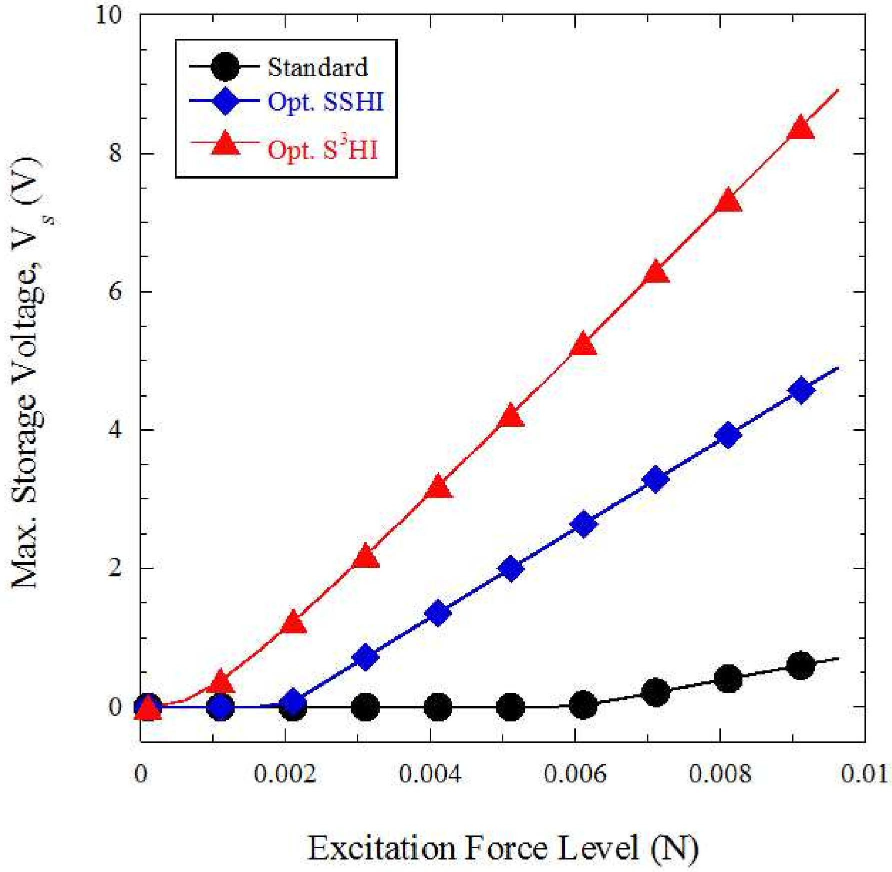

Fig. 37 Max. Storage Voltage for Standard, Optimal SSHI, and Optimal S^3HI, as a Function of Excitation Force Level.

C. Experimental Validation

1. Test Set-up

To investigate the performance of the proposed S^3HI strategy, a simple cantilever-type piezoelectric harvester and a switching circuit were prepared. Figure 34 shows the entire test setup. This test setup was mainly composed of the piezoelectric harvester assembly, a switching circuit for circuits B and C, an oscilloscope, a function generator, a power amplifier, and a DC/DC supply. Figure 35 shows a close-up view of the piezoelectric harvester assembly, which was mainly composed of a cantilever-type piezoelectric harvester and an electromagnetic based vibration exciter. Here, permanent magnets were attached to both sides of the piezoelectric harvester so that the eigenfrequency of the piezoelectric harvester could be tuned to the desired value of 40 Hz, which corresponds to the major excitation frequency of the cooler. In this configuration, the sinusoidal signal generated from the function generator and transmitted via the power amplifier was induced to the vibration exciter; the piezoelectric harvester thereby oscillated correspondingly. Then, the electrical harness of the piezoelectric harvester was connected to the switching circuit, as shown in Fig. 34; thus, the piezo-induced electrical energy resulting from the oscillating movement of the piezoelectric harvester could be forwarded to the switching circuit. Figure 36 shows a close-up view of the switching circuit for circuits B and C, dedicatedly manufactured for SSHI and S^3HI. An implementation for either circuit A or circuit B with this single circuit can be simply done by re-arranging a single harness. Figure 37 shows a detailed electrical schematic diagram of the switching circuit. As mentioned above, adapting the circuit for circuit B or circuit C can be simply done by making switch 1 point to either A or B. In this circuit, the switching signal for SSHI and S^3HI was directly provided by the function generator. Thus, this signal could be easily adjusted to get the desired switching frequency, duration, and phase. The switching trigger signal for each switching strategy was then forwarded to a MOSFET (IRF540PBF) switch via a photo coupler (K1010B). Here, the photo coupler was inserted to implement an electrical isolation between the trigger input of the function generator and the harvesting circuit. The alternating piezoelectric voltage resulted from the movement of the piezoelectric harvester was connected to the storage capacitor via a bridge diode. This bridge diode was a Schottky diode (PMEG2010), selected in order to minimize the threshold voltage caused by its forward voltage drop. The rectified voltage via the bridge diode was then stored in the storage capacitor, which had a capacitance of 4.7 uF, and its stored energy was slightly dissipated in the load resistor, which had a resistance of 500 $K\Omega$. The piezoelectric voltage, V_p, boosted voltage, V_B, and the stored voltage, V_s were then acquired using an oscilloscope via the operational amplifier (OPA445AP). In this experiment, the operational amplifier was used to avoid unwanted signal loss due to the low impedance of the oscilloscope. If the impedance of the data acquisition system is high enough, the operational amplifier can be neglected.

In this study, the abovementioned switching circuit and the peripherals were powered by an external DC/DC supply, as shown in Fig. 34, because the aim of this study was not to implement a stand-alone self-powered system, but to demonstrate the performance of the S^3HI strategy in comparison with conventional SSHI strategy.

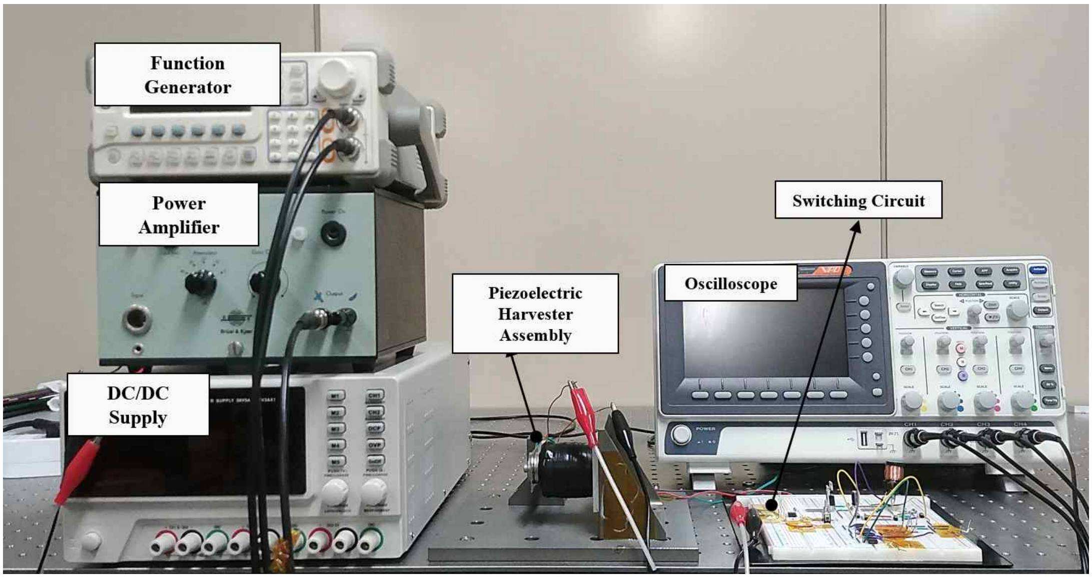

Fig. 38 Entire Test Set-up for Performance Test of S^3HI Strategy

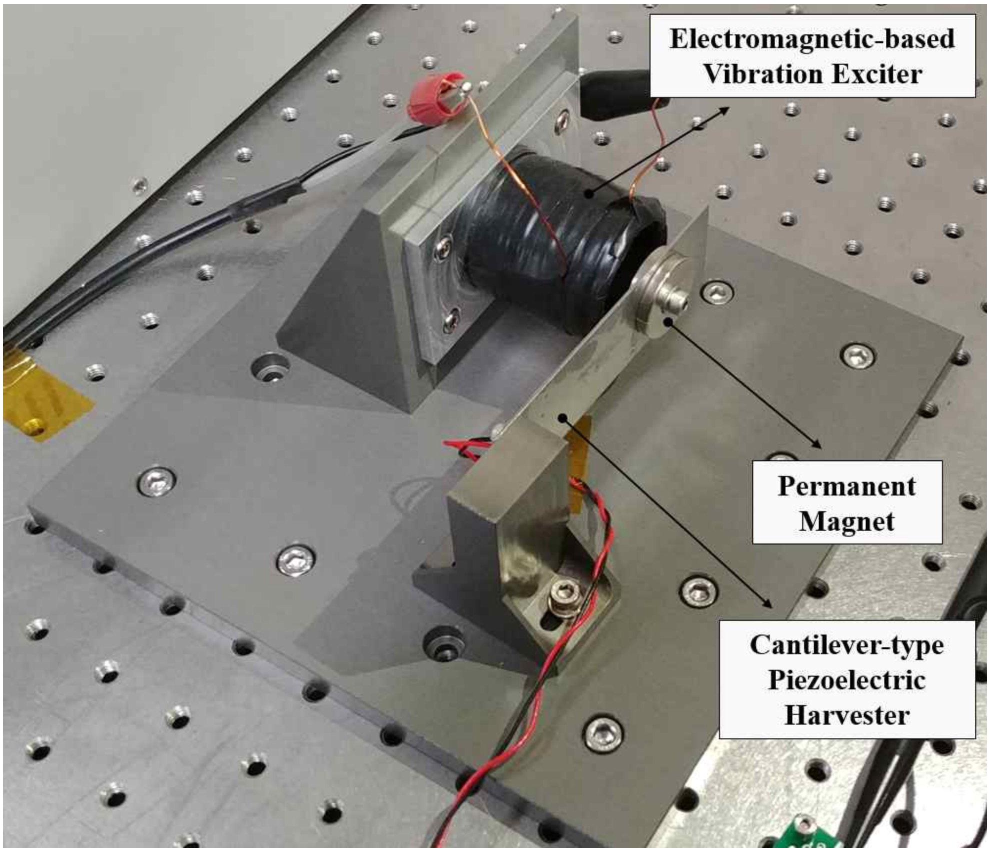

Fig. 39 Piezoelectric Harvester Assembly excited by Electromagnetic Vibration Exciter

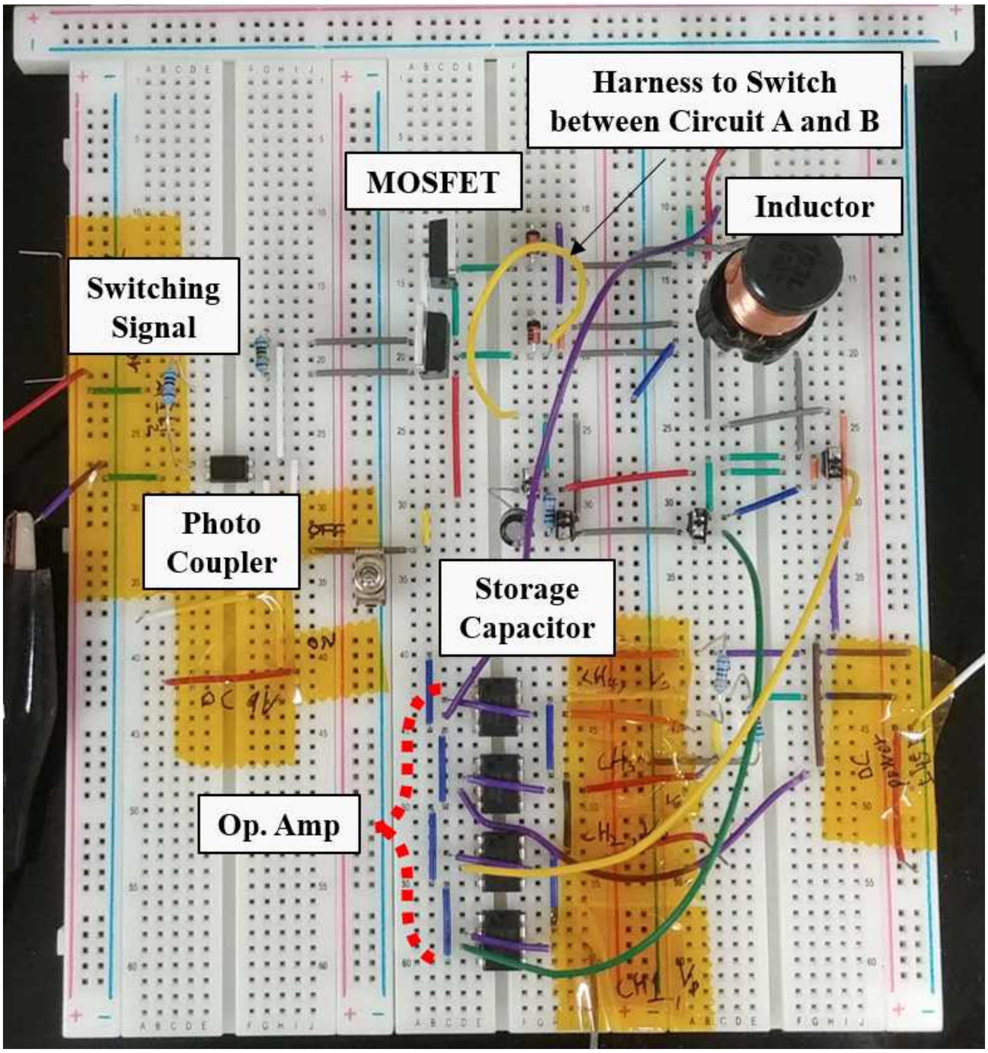

Fig. 40 Manufactured Switching Circuit for SSHI and S^3HI Strategies

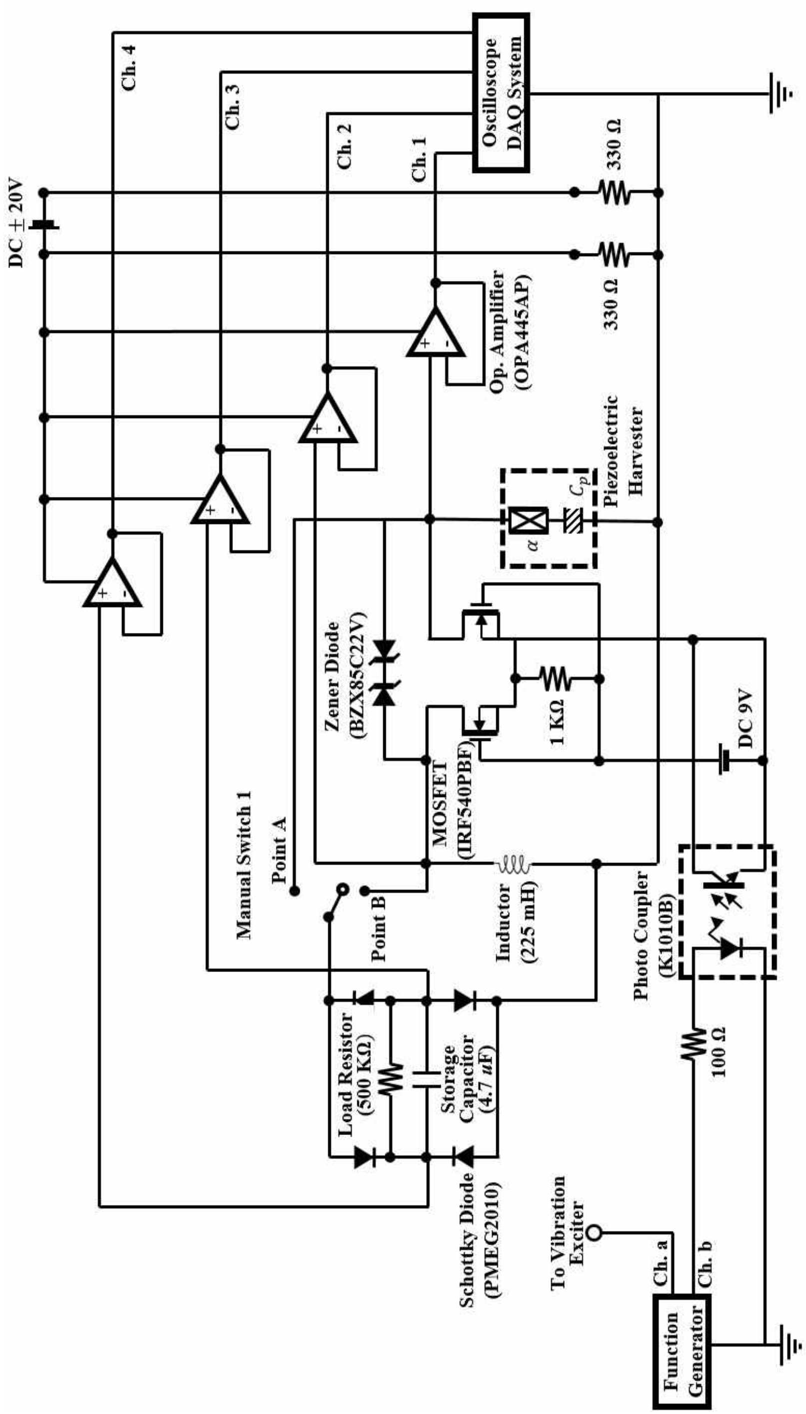

Fig. 41 Electrical Schematic Diagram of Switching Circuit

2. Test Result

Figure 38 shows the experimentally achieved maximum storage voltage for SSHI and S^3HI strategies during 10 s with respect to variations of β. During the test, the resolution of the switching system was limited to 5 ㎲, thereby more detailed investigations of the harvesting performance when β varies 3 place of decimals were impossible due to test system limitations. However, it was still worthy to observe how the harvesting performance could be affected by the variations of β in the test. In this figure, the SSHI strategy exhibits its maximum storage voltage under the condition of $\beta = 1$, as expected (in this condition, the switching duration was 530 ㎲); otherwise, its performance became significantly degraded when β was shifted out from the optimal condition of $\beta = 1$. This trend is almost the same as the result in a previous study [47] that reported the detrimental effect of the SSHI strategy when the switching duration was shifted out from the optimal value. However, the S^3HI strategy exhibits the greatest storage voltage under the condition of $\beta = 0.67$, and its maximum storage voltage of 6.3 V is much higher than the maximum storage voltage of SSHI by a factor of 1.26. This trend is almost all the similar with the numerical simulation results shown in Fig. 25 and indicates that the S^3HI strategy ensures a much higher performance when the switching duration is relatively shorter than a half electrical oscillation period, in contrast with the SSHI whose performance is degraded significantly by shorter or longer switching duration. However, under the longer switching duration for S^3HI, i.e., $\beta > 1$, the trend of maximum storage voltage gradually decreases. This behavior is caused by the largely dissipated energy in the circuit resistance during switch-on states. However, it can be concluded from the test results that the S^3HI strategy can guarantee higher harvesting performance when selecting the optimal switching duration, which is relatively shorter than the half-electrical oscillation period.

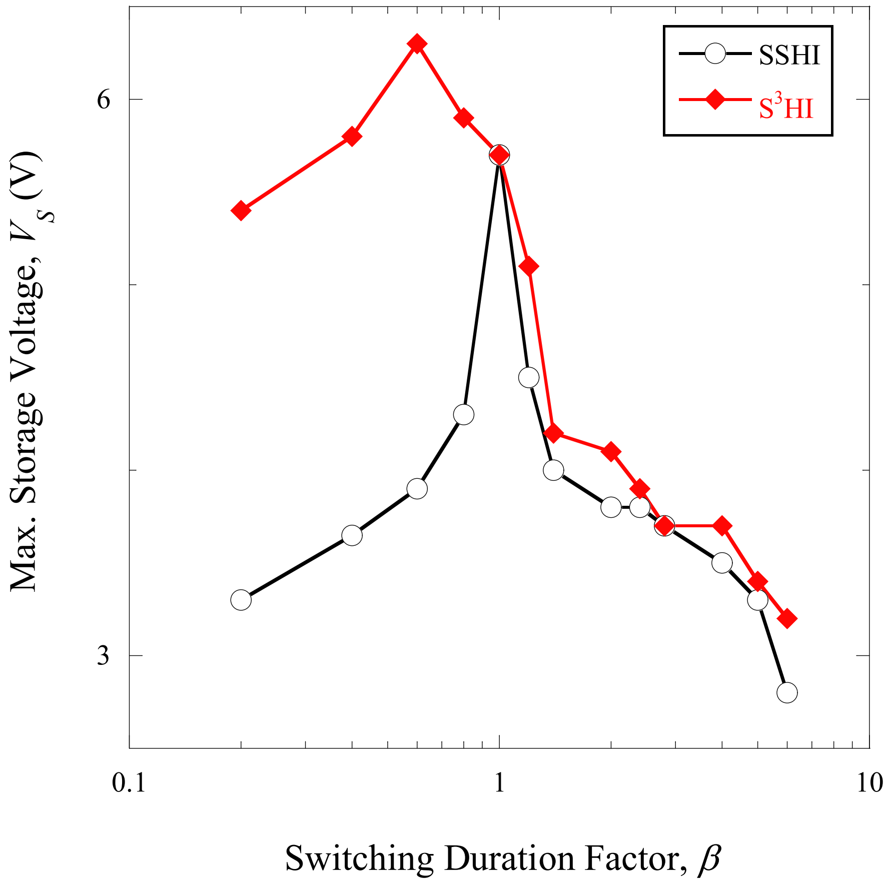

Fig. 42 Max. Storage Voltage V_s of SSHI and S^3HI Strategies with respect to Variations of β

Figure 39 shows the closed-up time histories of V_B and V_s for S^{3}HI, when different β are applied, e.g. $\beta = 0.67$ and 4.1, respectively. Here, $\beta = 0.67$ represents an optimal value, as indicated in Fig. 38, and $\beta = 4.1$ indicates an example case when β is largely shifted out from the optimal value. As can be seen, the case with optimal β exhibits a much higher voltage level at V_B right after the switching-off action. For instance, the optimal case yields approximately 60 V; otherwise, the shifted case yields 40 V, which is 1.5 times lower. In this manner, it can be seen from V_s that the optimal case possesses a much higher and larger effective charging curve than the opposite case. To investigate the charging performance between two cases quantitatively, an equation of $\sqrt{\int_{t_0}^{t_1} V_s^2 dt}$ is employed for each case. In this equation, t_0 and t_1 indicate the time immediately after switch-off and at the end of the experiment, respectively. In the optimal case, the calculated value is 0.08, and this value is by far greater than the shifted case by a factor of 2.9. Thus, an optimal value of β is always desirable to induce a greater surge phenomenon for enhancing harvesting performance.

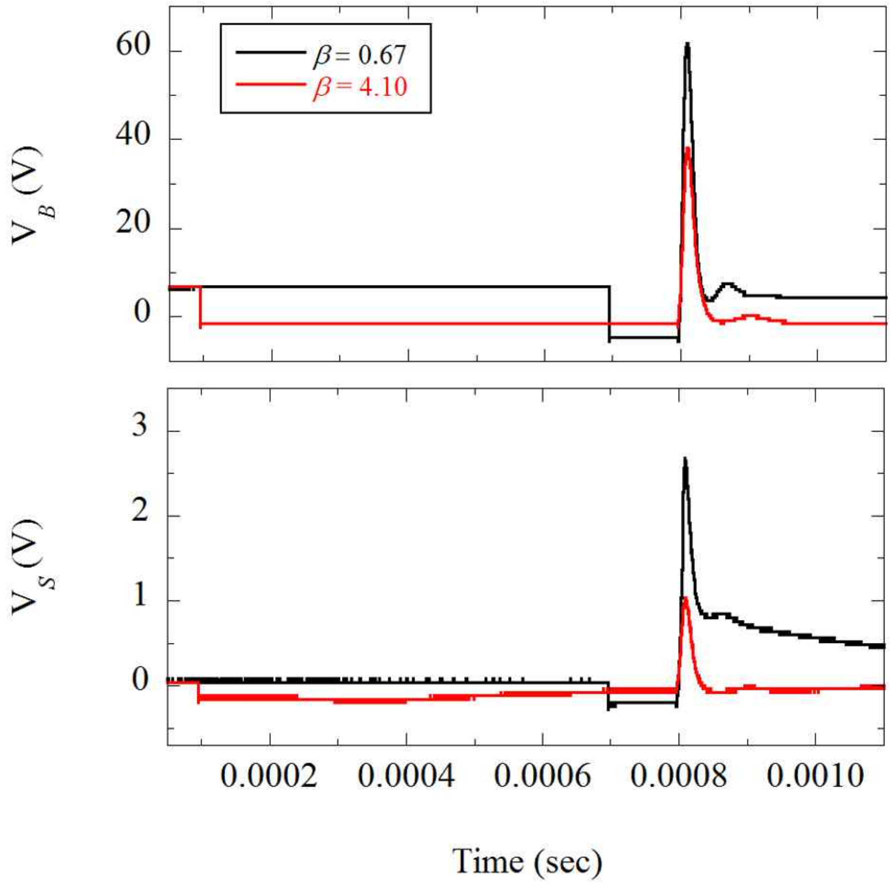

Fig. 43 Closed-up Time Histories of V_B and V_s for S^3HI, when different β are applied, e.g. $\beta =$ 0.67 and 4.1, respectively.

Figure 40 shows the experimentally achieved closed-up time histories of optimal SSHI and S^3HI strategies for piezoelectric voltage V_p, boosted voltage V_B, storage voltage V_s, and switch on–off states, respectively. In the test, the optimal SSHI applied the condition of $\beta = 1$; otherwise, the optimal S^3HI applied the condition of $\beta = 0.67$ according to the optimal schemes shown in the results in Fig. 38. In the fig. 40, the piezoelectric voltages V_p for optimal SSHI and S^3HI strategies are inverted during switch-on state, and the those strategies show almost all the similar behavior in V_p, even if the voltage inverting duration of the optimal S^3HI is relatively shorter then that of the optimal SSHI due to relatively shorter switching duration. Nevertheless, the boosted voltage V_B for optimal SSHI and S^3HI strategies shows quietly different behavior. For optimal SSHI, the trend is almost the same as V_p. Otherwise, the optimal S^3HI exhibits the surge voltage right after switch-off. Once the results of storage voltage V_s have been considered, no increase behavior can be observed for the optimal SSHI case. Meanwhile, the trend of increase in V_s represented by the black envelope curve is clearly observed in optimal S^3HI, meaning that this proposed strategy can charge the storage capacitor in compliance with the battery-charging requirement, i.e. $|V_B| > V_{fw} + V_s$. In this strategy, the major contributor to charge the storage capacitor is the surge phenomenon induced by sudden transient current in the inductor. These facts are well in agreement with the expected results from the simulation shown in Fig. 27.

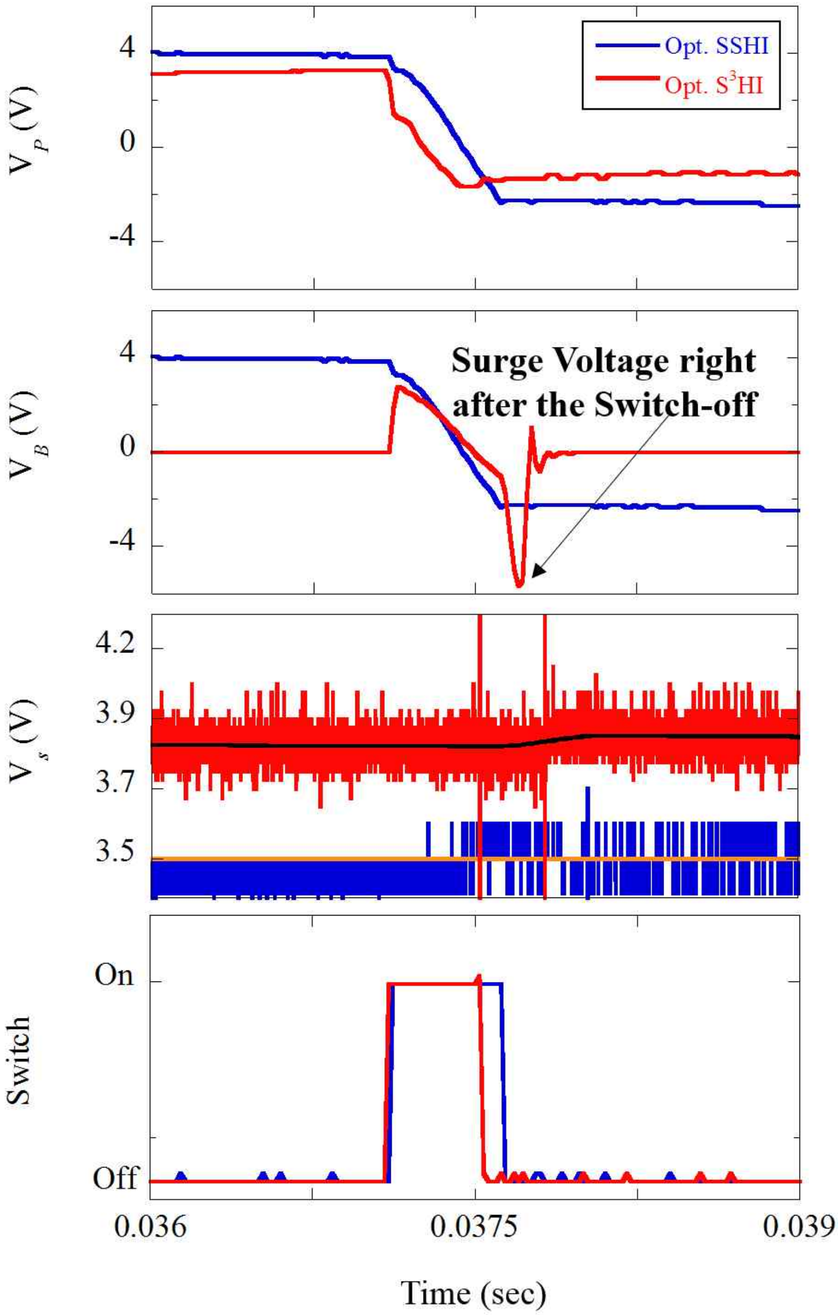

Fig. 44 Closed-up Time Histories of Optimal SSHI and S[3]HI Strategies for Piezoelectric Voltage V_p, Boosted Voltage V_B, Storage Voltage V_s, and Switch On–Off States, respectively

Figure 41 shows the storage voltage history for optimal SSHI and S^3HI strategies with respect to different storage capacitance, i.e. 4.7 ㎌ and 47 ㎌, respectively. As shown in the figure, the condition with optimal S^3HI shows relatively higher storage voltage levels compared with the optimal SSHI, regardless of the capacitance value. Considering the case when the storage capacitance is 4.7 ㎌, the optimal SSHI exhibits a storage voltage level of approximately 8 V at the end of charging time; otherwise, the optimal S^3HI exhibits 9.6 V, which represents a 1.2-fold increase over the optimal SSHI. In addition, the increasing trends of the storage voltage between optimal SSHI and S^3HI strategies are different. For example, the voltage for optimal SSHI increases until 5 *s*; otherwise, it gradually decreases at the end of the charging time. However, in case of optimal S^3HI, no saturation behavior can be seen, but it still strives to charge the storage capacitor. This means that the storage voltage level of the optimal S^3HI becomes much higher if the charging time becomes longer than the experimental result shown in Fig. 41. This superior harvesting capability of the optimal S^3HI is caused by the surge phenomenon already mentioned. However, comparing the results of optimal S^3HI with respect to storage capacitances, i.e. 4.7 ㎌ and 47 ㎌, a case with smaller capacitance shows a relatively higher storage voltage level by a factor of 2.4 within the given charging time. However, in terms of stored energy calculated from an equation of $(1/2)C_pV_s^2$, the case of 4.7 ㎌ yields 216.6 ㎼; otherwise the case of 47 ㎌ yields 376 ㎼. Obviously, the case of larger storage capacitance possesses larger stored energy and represents a 1.7-fold increases over the smaller capacitance case. Consequently, the optimal capacitance value depends on the application types. For instance, the case with a smaller capacitance is preferable when the charging time is important. Otherwise, the case with a larger capacitance is preferable when the amount of stored energy is important.

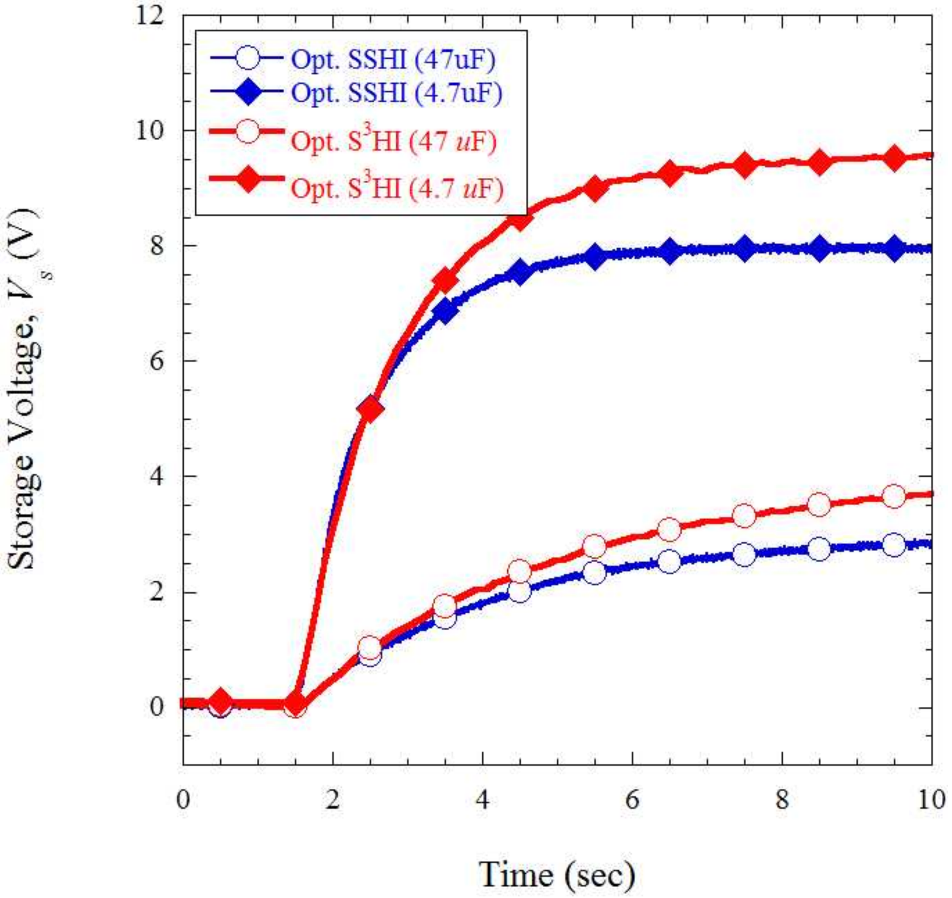

Fig. 45 Storage Voltage History for Optimal SSHI and S^{3}HI Strategies with respect to Different Storage Capacitance, i.e. 4.7 ㎌ and 47 ㎌, respectively

Figures 42 (a) and (b) show the LED on and off states for optimal SSHI and S^3HI strategies, respectively. In the test, an LED was employed to check the feasibility of turning the LED on by utilizing the harvested energy with respect to each switching strategy. The LED was connected in parallel with a storage capacitor that has a capacitance of 47 ㎌, and the LED had an operating voltage of 3.3 V and operating current of 20 mA. As shown in the figures, the LED in optimal SSHI was not turned on; however, it was clearly turned on in optimal S^3HI strategy. As shown in Fig. 41 above, the saturation level of the optimal SSHI is approximately 2.9 V, which is less than the operating voltage of the LED. However, the voltage level of the optimal S^3HI is calibrated at around 4 V, and its level is large enough to exceed the operating voltage of the LED.

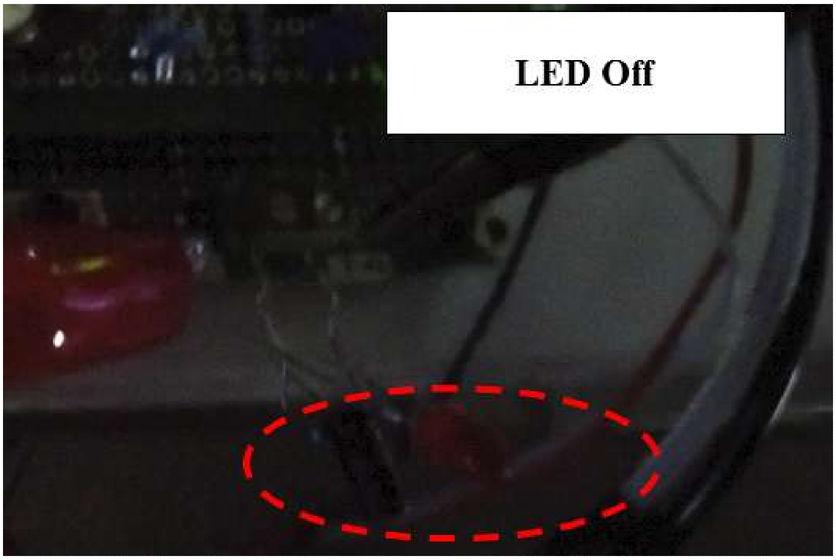

(a)

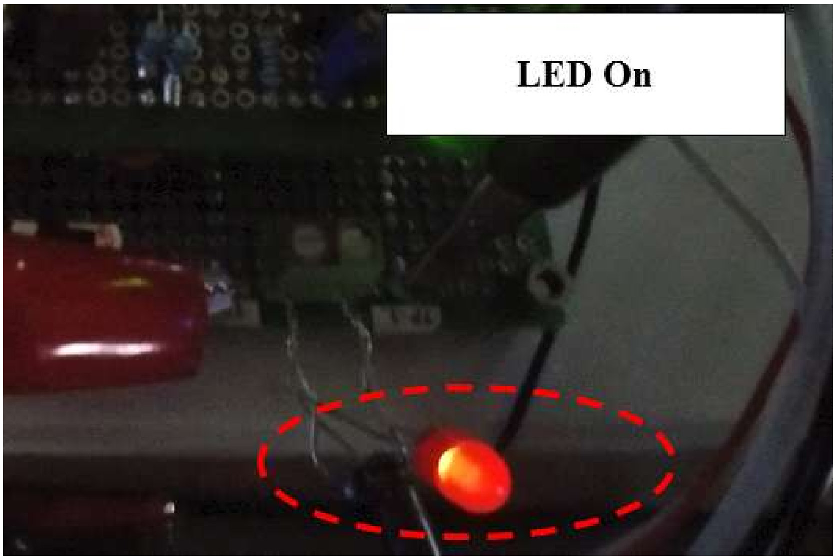

(b)

Fig. 46 LED On and Off States with respect to Switching Strategies [(a): Optimal SSHI, (b): Optimal S^3HI]

Figure 43 shows the experimentally achieved maximum storage voltage of optimal SSHI and S^3HI for 10 s, as a function of the vibration excitation level. In this result, the optimal SSHI has an ineffective harvesting range under the force condition, smaller than a value of 1 N. However, the optimal S^3HI can guarantee energy-harvesting capability, even in such a small vibration range, in contrast with the optimal SSHI strategy. In addition, the storage voltage level of the optimal S^3HI is by far higher than the optimal SSHI in all force ranges. These trends agree well with the expected result from the simulation results shown in Fig. 33. Consequently, it can be said that the optimal S^3HI strategy has a superior potential in various harvesting fields because of its effectiveness, not only in small vibration levels, but also in high vibration levels with higher harvesting performance compared with the SSHI strategy.

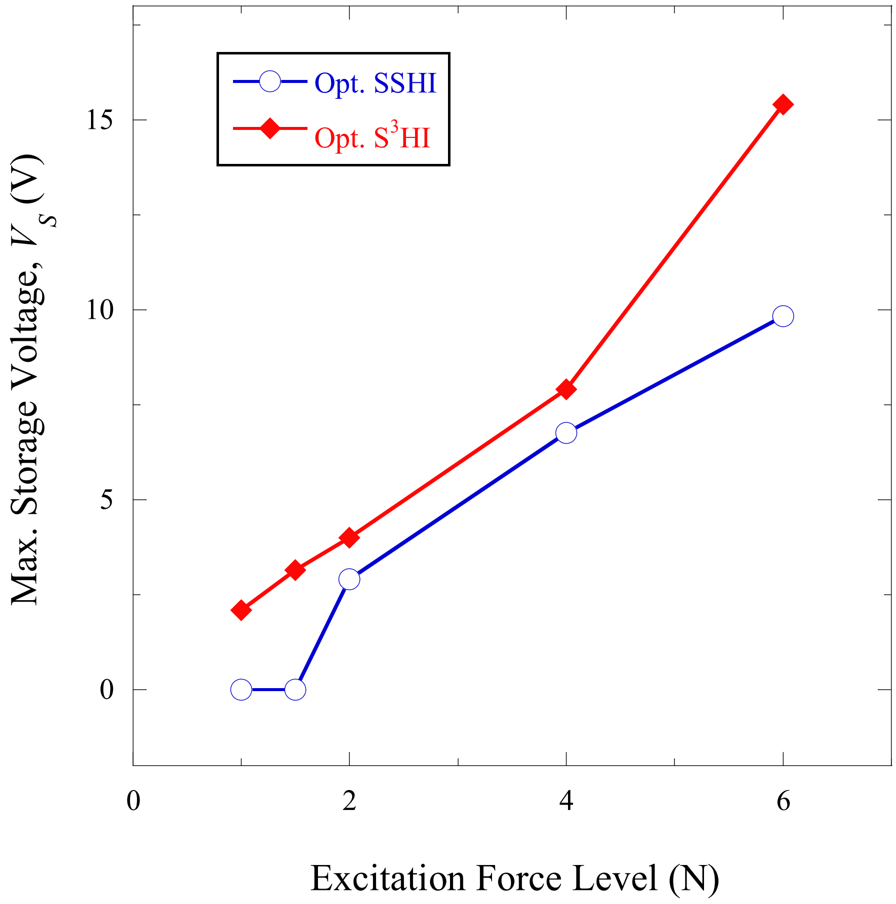

Fig. 47 Maximum Storage Voltage V_s of Optimal SSHI and S^3HI Strategies for 10 s, as a Function of Vibration Force Level.

IV. Performance Evaluation on Piezoelectric Harvester Level for H-S^3HI Strategy

A. System Configuration

1. Switching Design Driver

The effectiveness of the S^3HI strategy has been demonstrated in above section through incorporating numerical and experimental approaches. The main feature of the S^3HI strategy was inducing sudden current transits in an inductor by intentionally shortening the switching duration compared with the optimal switching duration of conventional SSHI [1]. However, such a strategy inevitably suffers from a series of energy losses in the inductor at every instance of switching, due to its relatively shorter switching duration compared with conventional SSHI.

To overcome the abovementioned drawbacks of the S^3HI strategy while still striving to induce surge phenomena to exploit their full potential from the point of view of energy harvesting capability, a novel strategy that combines high-frequency switching with the S^3HI switching is proposed. The basic concept of the proposed strategy is to make the switching duration relatively longer than the S^3HI strategy, while finely splitting it up to realize high-frequency switching. Thereby, both the demands of maximizing the incoming energy in the inductor and maintaining the surge-inducing mechanism can be satisfied by the proposed switching strategy, which we called the high-frequency-included surge-inducing synchronized-switch harvesting (H-S^3HI) strategy.

To investigate the feasibility of the H-S^3HI strategy combined with a piezoelectric energy harvester, we used the already established numerical simulation model shown in Fig. 16 and equations of motion shown in Eqs. (3-1) ~ (3-6). In this model, the circuit C dedicated to the surge-inducing mechanism was employed for the H-S^3HI strategy as well.

2. Control Logic

To implement the proposed H-S[3]HI strategy, it is essential that the switching duration should be long enough, as much as close to that of the SSHI strategy, while still striving to induce a sudden transit current in the inductor to trigger the surging phenomenon. This novel strategy can be implemented by splitting up the switching period in order to obtain high-frequency switching, and this high-frequency switching should last for τ_{opt}, as shown in Fig. 44. Consequently, both demands of maximizing the incoming energy in the inductor and maintaining the surge-inducing mechanism can be satisfied. This strategy can be implemented as follows:

$$\begin{aligned} &\text{High-Frequency Switch = on} &&\text{when } t_{on} = t_{|x_{\max}|} \\ &\text{High-Frequency Switch = off} &&\text{when } t_{off} = t_{on} + \tau_{opt} \end{aligned} \tag{4-1}$$

In this case, the high-frequency switch is kept on for $t_{on} \le t \le t_{off}$, and can be represented as a pulse-width modulation (PWM) signal as follows:

$$\begin{aligned} P_{Hi.Sw} &= 1/f_{Hi.Sw} \\ D_{Hi.Sw} &= 1/f_{Hi.Sw} \times \psi \end{aligned} \tag{4-2}$$

where $P_{Hi.Sw}$ and $f_{Hi.Sw}$ denote the high-frequency switching period and its frequency, respectively, $D_{Hi.Sw}$ denotes the duty cycle, and ψ denotes the high-frequency switching duration factor.

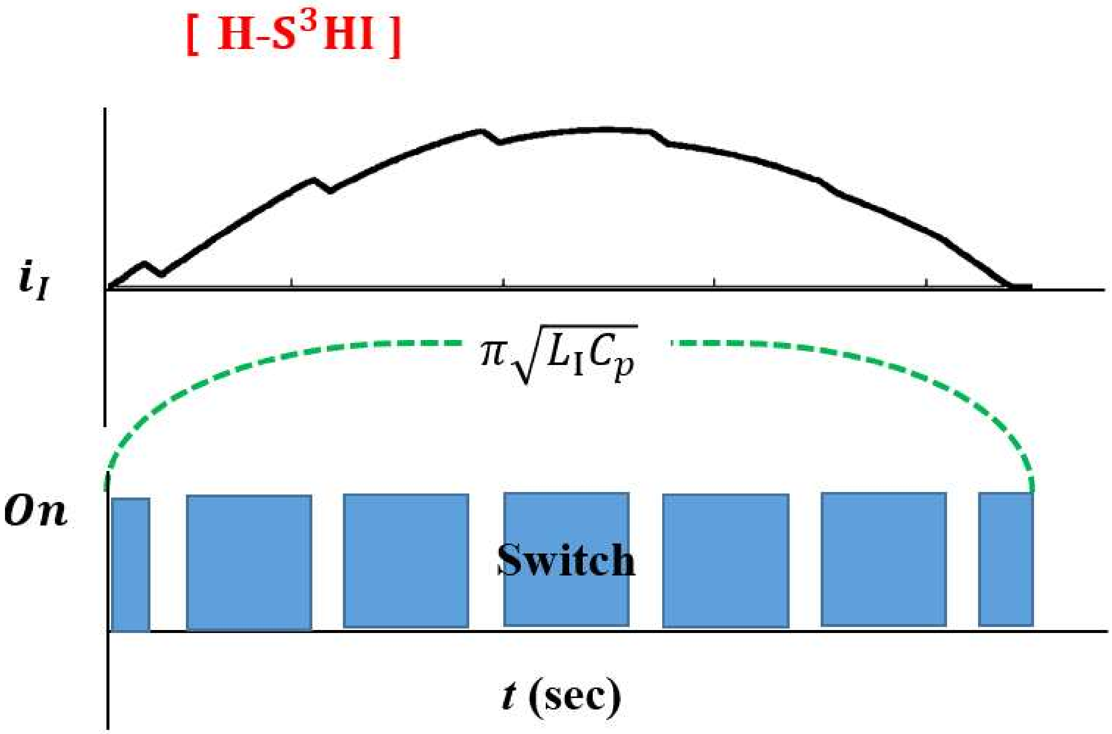

Fig. 48 Shape of Electrical Current i_I flowing though Inductor with respect to H-S³HI Strategy

B. Numerical Simulation

To investigate the feasibility of the high frequency-included surge-inducing synchronous switching harvesting strategy, namely H-S^{3}HI, proposed in this study, the Matlab/Simulink model shown in Fig. 19 is utilized. In this model, to implement the high frequency PWM switching as defined in above Eqs. (4-1) and (4-2), the switch controller additionally includes the high frequency PWM switching combination block as shown in Fig. 45. In addition, to make the switching duration as long as that of the SSHI strategy, the optimal switching duration of 530 μs calculated using the Eq. (3-7), $\pi\sqrt{L_I C_p}$, is applied. In addition, the optimal values of frequency of high-frequency PWM switching, $f_{Hi.Sw}$, and its duration factor, ψ, for the H-S^{3}HI strategy are determined in the next simulation result section. Aside from above facts, the other simulation parameters along with the external force, 0.5 N, and its excitation frequency, 40 Hz, are all the same with Table 3

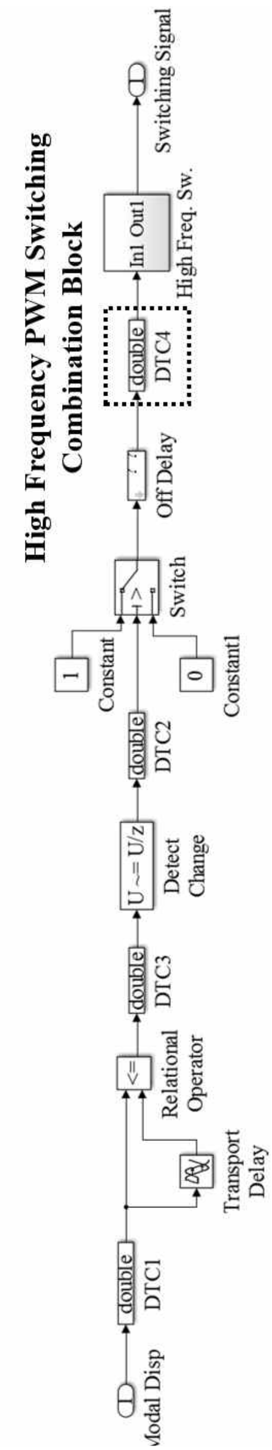

Fig. 49 Switching Controller Subsystem Block of H-S³HI Strategy in combination with High Frequency PWM Combination Block

1. Simulation Result

Figure 46 shows a 3D plot of the maximum stored voltage as a function of the frequency of high-frequency PWM switching, $f_{Hi.Sw}$, and its duration factor, ψ, for the H-S^{3}HI strategy. In this plot, it can be noted that the stored voltage level gradually goes up as the duration factor increases, because the energy incoming to the inductor during the switch-on state increases as the switching duration increases. However, the duration factor cannot take a value of 100 %, because no surging effects could be expected at that point anymore. On the other hand, it can also be noted that the H-S^{3}HI strategy exhibits the greatest stored voltage level at the specific point in which $f_{Hi.Sw}$ and ψ take their optimal values. In this study, the identified optimal values of ψ and ψ for an optimal harvesting performance with the H-S^{3}HI strategy are 4 kHz and 90 %, respectively. These identified values were used in the following numerical simulations and experiments.

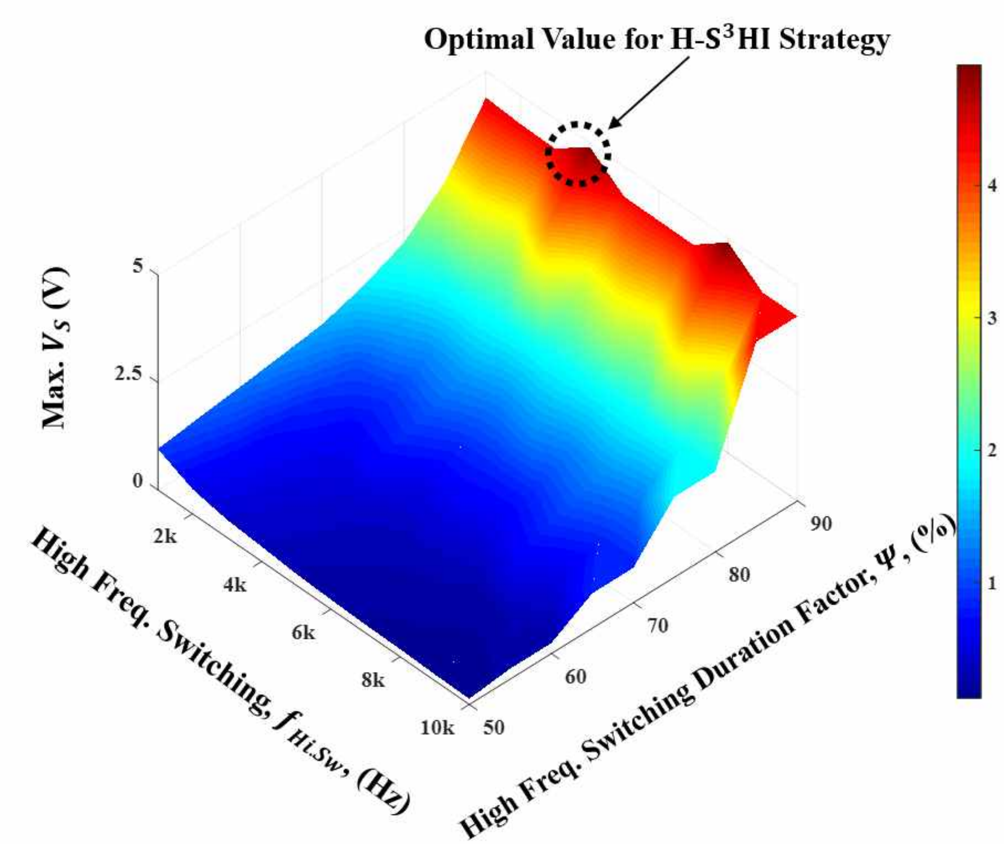

Fig. 50 3D Plot of Maximum Stored Voltage as a Function of High PWM-switching Frequency, $f_{Hi.Sw}$, and its Duration Factor, ψ, for H-S^3HI Strategy

Figures 47 and 48 show the overall and close-up views of the time histories for displacement, x, piezo-induced voltage, V_p, boosted voltage, V_B, electrical current flowing out from the inductor, i_I, stored voltage, V_s, electrical current towards the storage capacitor, i_s, and switch status for optimal SSHI, S^3HI, and H-S^3HI strategies, respectively. In this simulation, the optimal frequency values for high-frequency PWM switching, $f_{Hi.Sw}$, and the corresponding duration factor, ψ, for the H-S^3HI strategy were used based on the results shown in Fig. 46. On the other hand, as can be observed in Fig. 47, the trends of x for almost all switching cases exhibit a similar behavior. Meanwhile, the other trends show a clearly different behavior due to the different switching control scheme used. From this result, the occurrence of the electrical current flow, i_s, reveals that V_B exceeds the sum of the threshold voltage accompanied by the diode forward voltage drop, V_{fw}, and the existing stored voltage, V_s; i.e. $|V_B| \geq V_{fw} + V_s$. Consequently, the existence of i_s means that the storage capacitor is being charged. In contrast, no i_s is observed in the SSHI case, while the generation of i_s in S^3HI and H-S^3HI cases is clear, despite the differences in behavior of i_s, in which surge-inducing mechanisms are employed. By comparing the behavior of V_B, i.e. comparing SSHI with S^3HI and H-S^3HI, it can be seen that the trends are quite different. In the SSHI case, its electrical dynamics while the switch is on can be represented by Eq. (3-4), and voltage V_B becomes inverted by as much as the inversion factor of the inductor [51]. When the switch is off, the connection between inductor L_I and storage capacitor C_s is broken. Thus, V_B is only affected by the voltage being output from the piezoelectric element. During this state, V_B slightly increases by as much as $\alpha x / C_p$, as described in Eq. (3-6). If the absolute value of $|V_B|$ is larger than $V_{fw} + V_s$ as a result of the variations of x, current i_s flows toward C_s. However, when V_s becomes saturated, $|V_p|$ cannot exceed $V_{fw} + V_s$, and i_s does not flow toward C_s. Consequently, the storage capacitor can no longer be charged when using the SSHI strategy, as can be observed in Fig. 47. To use the SSHI strategy for micro-scale vibration energy harvesting, a higher inversion factor of the inductor or larger vibration amplitudes are required. However, these alternatives cannot be the proper technical solution to this problem because of limitations in real applications. On the other hand, in the S^{3}HI and H-S^{3}HI cases, the flow of i_s can be observed, meaning that these strategies can charge the storage capacitor by complying with the battery charging requirement, i.e. $|V_B| \geq V_{fw} + V_s$. In this way, the electrical potential being output by the piezoelectric element directly affects the inductor as soon as the switch is turned on. Then, V_B increases to a level as high as V_p. Subsequently, a voltage inversion behavior which lasts as long as optimal switching durations occurs. However, the S^{3}HI and H-S^{3}HI strategies show different voltage inversion levels. For example, the switching duration of H-S^{3}HI corresponds to the optimal switching duration, τ_{opt} calculated from $\pi\sqrt{L_I C_p}$, which results in exactly half of the electrical oscillation period. Thus, the piezoelectric voltage, V_p, is largely inverted for as long as the optimal duration. On the other hand, the S^{3}HI strategy, which has a relatively shorter switching duration, imposes detrimental effects on the amplitude of V_p. Meanwhile, right after switching to the off state, the inductor in circuit C is not affected by the voltage coming out of the piezoelectric element. However, it is still subjected to a closed-circuit condition with the storage capacitor via the bridge diode; it's the electrical dynamics in this state can be expressed as in Eq. (3-5) above. In this state, a sudden transient current that results in significant slope changes in i_I is observed, as can be seen in the close-up view of Fig. 48. This transient current flow lasts until it becomes zero, because the current flowing through the inductor cannot be instantaneously canceled. Consequently, a highly boosted surge voltage induced by the inductor occurs, resulting in a high voltage that complies with the charging requirement, $|V_B| \geq V_{fw} + V_s$. In this manner, more frequent appearances of the surging voltage, V_B, in line with electrical current flow forward to the storage capacitor, i_s, can be observed in the H-S^{3}HI case at each instance of high-frequency switching, compared with the S^{3}HI case. Moreover, it can be noted from Fig. 48 that the enclosed area of i_I in the H-S^{3}HI case is much bigger than for the other strategies. This means that H-S^{3}HI exploits the full potential of the inductor, as we intended in this study. Using the stored voltage as a performance index, it can be seen that H-S^{3}HI exhibits the highest stored voltage level compared with the other cases. For example, H-S^{3}HI charges the storage capacitor up to 3.3 V, and this value is 1.65 times higher than that of SSHI. If the simulation time was long enough, this ratio would become much larger.

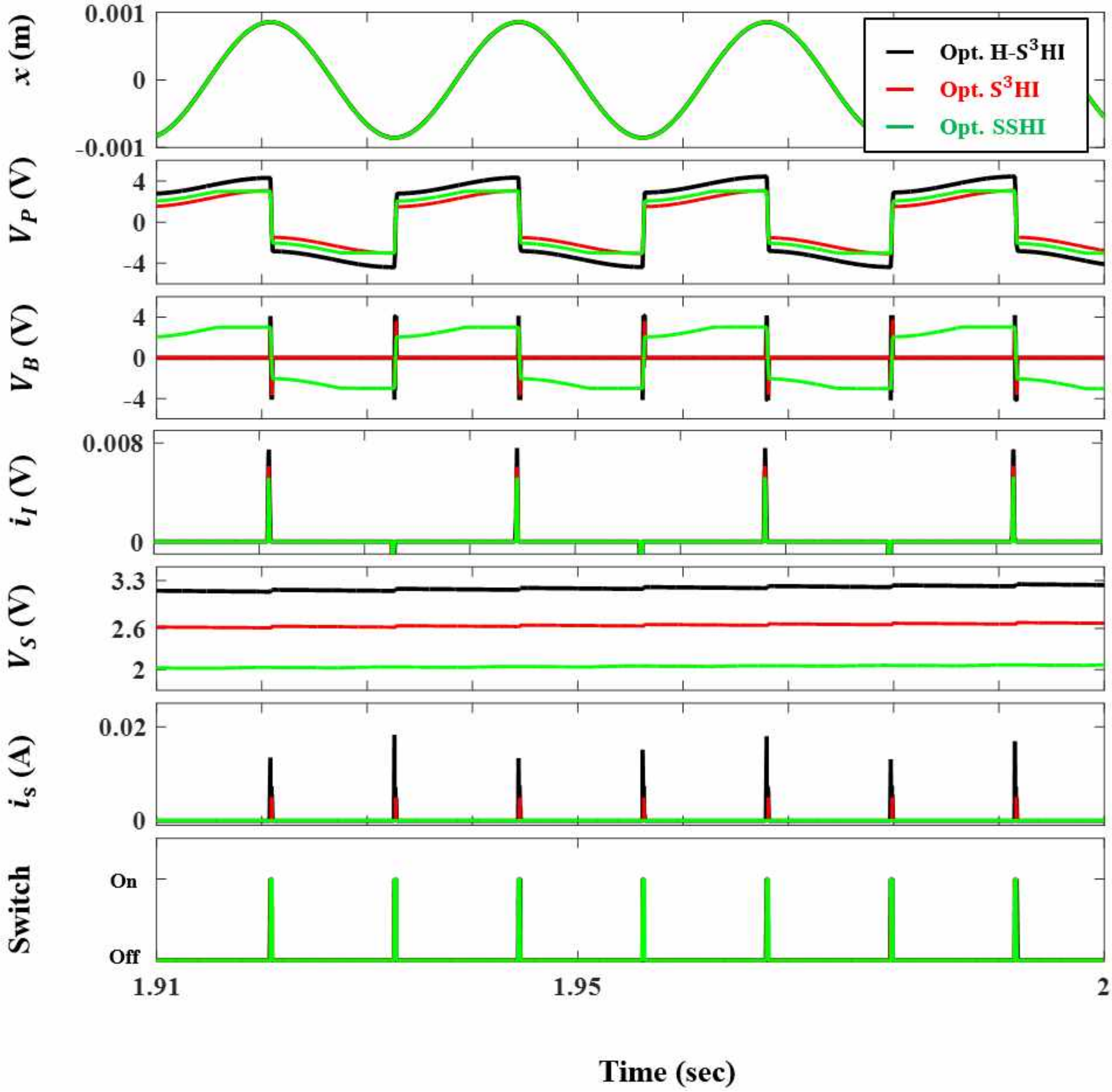

Fig. 51 Simulated Time Histories for Displacement, x, Piezo-induced Voltage, V_p, Boosted Voltage, V_B, Electrical Current flowing out of the Inductor, i_I, Storage Voltage, V_s, Electrical Current flowing towards Storage Capacitor, i_s, and Switch Status for SSHI, S^3HI, and H-S^3HI, respectively

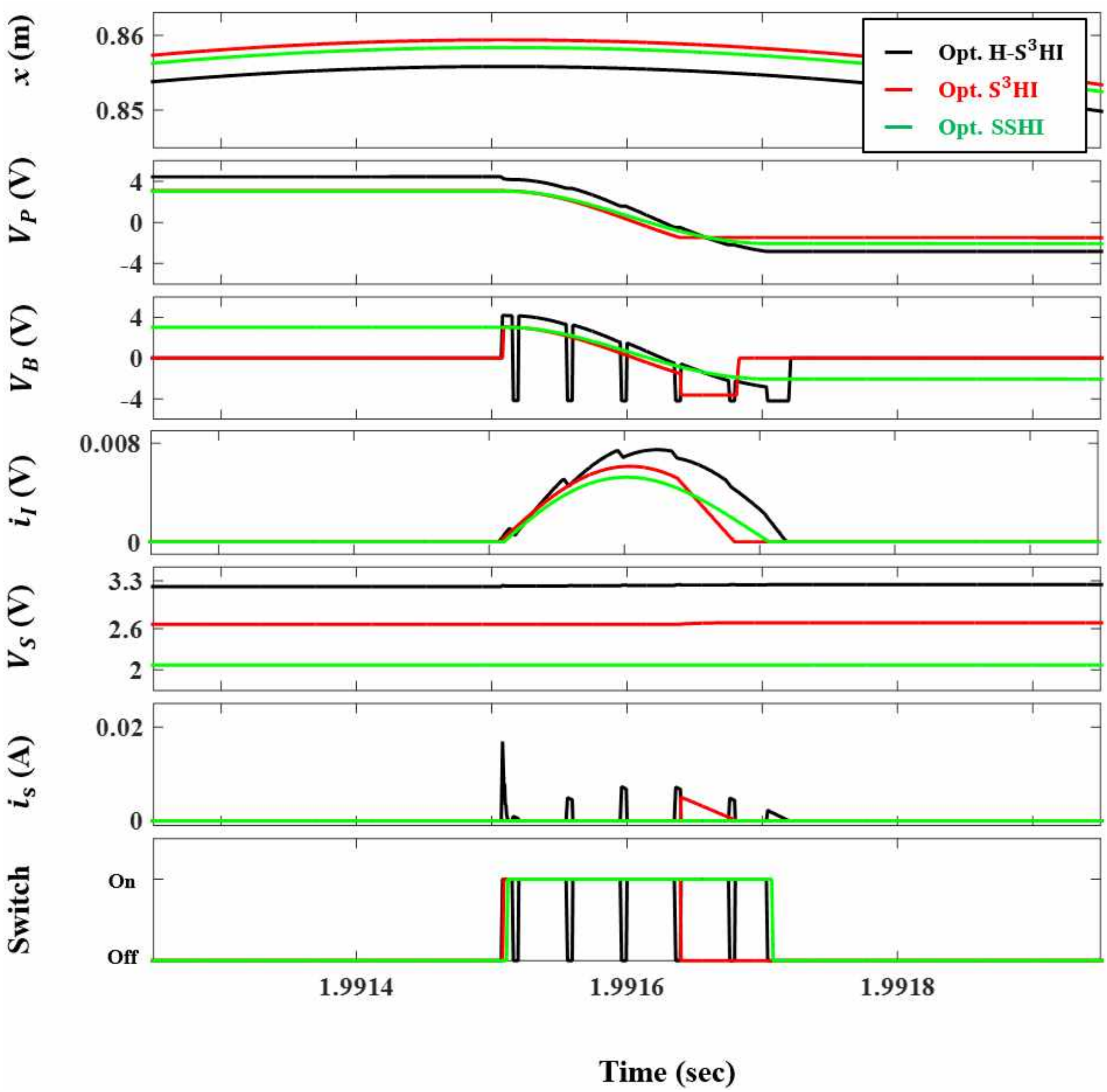

Fig. 52 Simulated Closed-up Time Histories for Displacement, x, Piezo-induced Voltage, V_p, Boosted Voltage, V_B, Electrical Current flowing out of Inductor, i_I, Storage Voltage, V_s, Electrical Current flowing towards Storage Capacitor, i_s, and Switch Status for SSHI, S^{3}HI, and H-S^{3}HI, respectively

Figure 49 shows the maximum stored voltages for the SSHI, S^3HI, and H-S^3HI strategies over 2 s, as a function of the vibration force level. In this figure, it can be noted that the SSHI strategy cannot be used to charge the storage capacitor up until the vibration level reaches 0.008 N. In contrast, the switching strategies, by exploiting the surging effects with dedicated circuit C, can guarantee their energy harvesting capabilities even in the small vibration range, i.e. excitation force levels below 0.008 N. In the S^3HI case, it can consistently charge the storage capacitor, no matter how low the excitation force level is. However, it should be noted that the slope of the maximum stored voltage in the H-S^3HI case increases dramatically for a force value of approximately 0.006 N and, as this force value increases, this strategy surpasses the S^3HI strategy for excitation force levels higher than 0.008 N. If the harvesting time becomes much longer, it can be expected that the H-S^3HI strategy might yield a higher stored voltage level for excitation force levels higher than 0.006 because of its greater harvesting potential compared with the S^3HI strategy. On the other hand, for forces in a smaller range, i.e. excitation force levels below 0.005 N, the H-S^3HI strategy definitely shows poor harvesting potential compared with S^3HI because most of the surge-induced energy occurring at each instance of high-frequency switching is dissipated in the resistors of the circuit. However, the effective force level for H-S^3HI is still regarded as a challenging level for conventional methods, i.e. circuit A for the standard harvesting method and conventional SSHI. Moreover, if circuit C could be controlled to switch between H-S^3HI and S^3HI in accordance with the given force levels, a much better harvesting performance would be achieved, though this method was not investigated in this study.

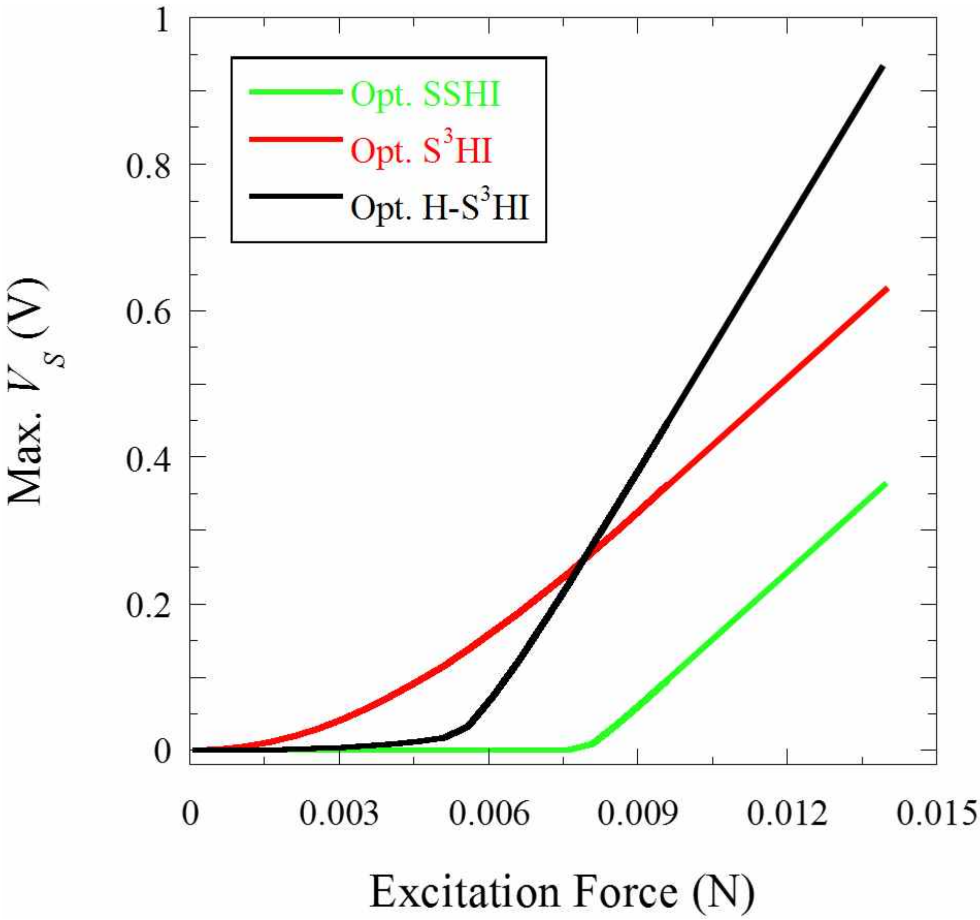

Fig. 53 Maximum Stored Voltages for SSHI, S^3HI, and H-S^3HI Strategies after 2 s, as a Function of Vibration Force Level

C. Experimental Validation

Figure 50 shows a electrical schematic diagram of the switching circuit that additionally includes the high frequency PWM switching module based on the existing switching circuit shown in Fig. 37. The high frequency PWM switching for H-S^3HI was made by combining the signal from the function generator and that of a high-frequency PWM IC chip (TL494). This signal combination could be executed in an AND gate (DM7408), provided that the manual switch 2 was turned on. Additionally, the high-frequency PWM signal could be adjusted via the adjustable resistor and capacitor, thereby desirable high-frequency switching $f_{Hi.Sw}$ and its duration factor ψ could be achieved. The other functions of the manufactured circuit are all the same with the descriptions noted in the test set-up above in section 2.

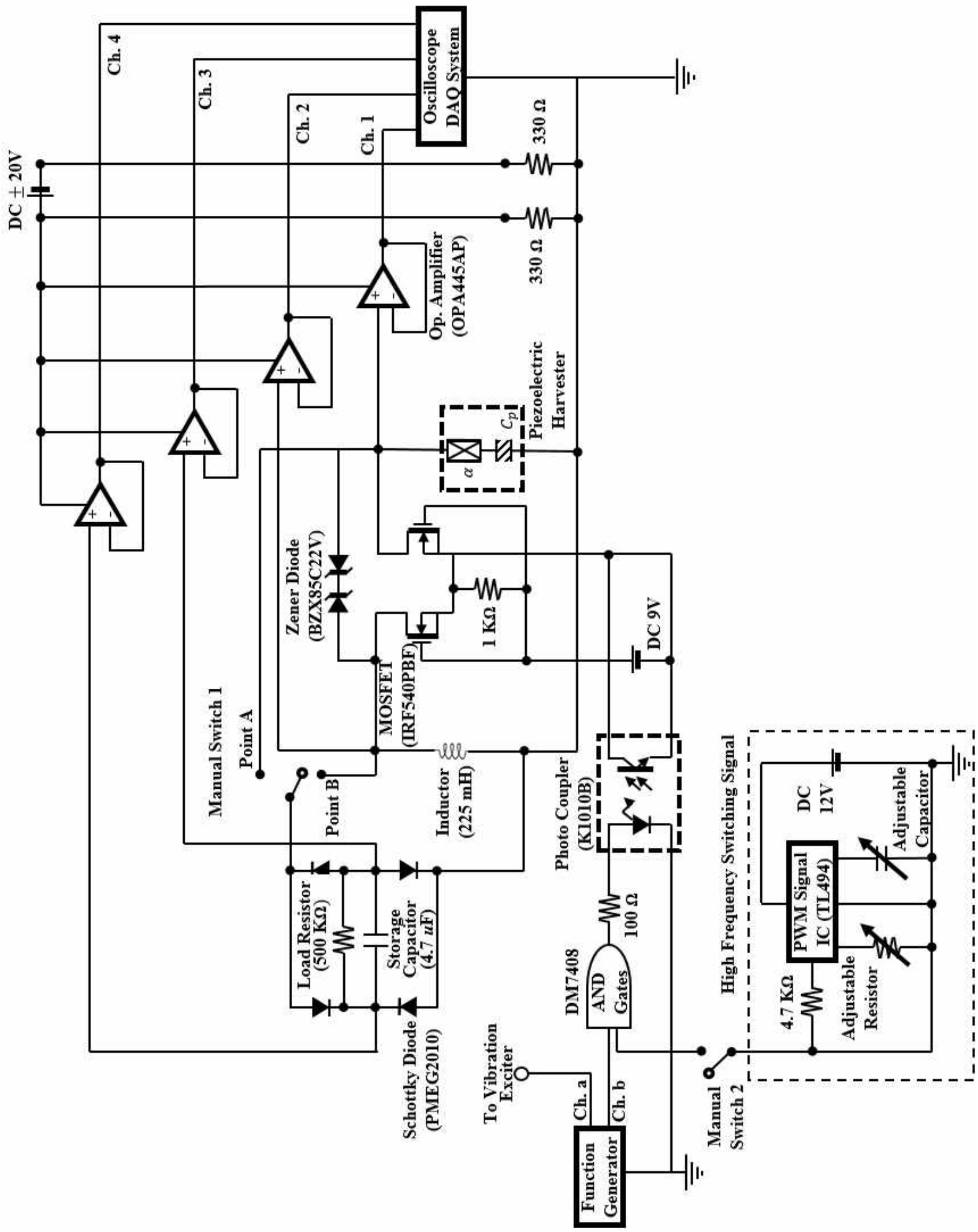

Fig. 54 Electrical Schematic Diagram of the Switching Circuit for H-S^{3}HI

1. Test Result

Figures 51 and 52 show close-up views of the time histories of the piezo-induced voltage, V_p, the boosted voltage, V_B, the stored voltage, V_s, and the switch status for the optimal S^3HI, and $H\text{-}S^3HI$ strategies, respectively. As can be seen in the figures, all switching strategies invert the piezoelectric voltage, V_p, while the switch is kept on for their corresponding optimal switching durations. However, according to the switching strategy, it can be observed that the behaviors of V_B are quite different from each other. For example, V_p and V_B in S^3HI and $H\text{-}S^3HI$ strategies, which use the circuit C to introduce the surging effects for energy harvesting, yield different behaviors. As can be seen in figure, the optimal $H\text{-}S^3HI$ strategy shows frequent occurrences of surging voltages at V_B in accordance with the high frequency PWM switching actions defined in Eq. (4-2). These phenomena that we have addressed are almost all coincident with the expected results we derived from numerical simulations, as can be seen in Fig. 48. In the experimental results, it can be also observed that the increasing trends of V_s for the optimal S^3HI and $H\text{-}S^3HI$ strategies are different. For example, V_s in the optimal S^3HI case goes up all at once when the surge voltage occurs. On the other hand, V_s in the $H\text{-}S^3HI$ case rises gradually as long as the high frequency switch is kept on. This voltage level reached a value of 0.035 V, which is by far the highest level compared with the other switching strategies. This increased level was approximately 1.8 times higher than that obtained with the optimal S^3HI strategy even though only one switching action was carried out; a much better charging performance can be expected for much longer harvesting times.

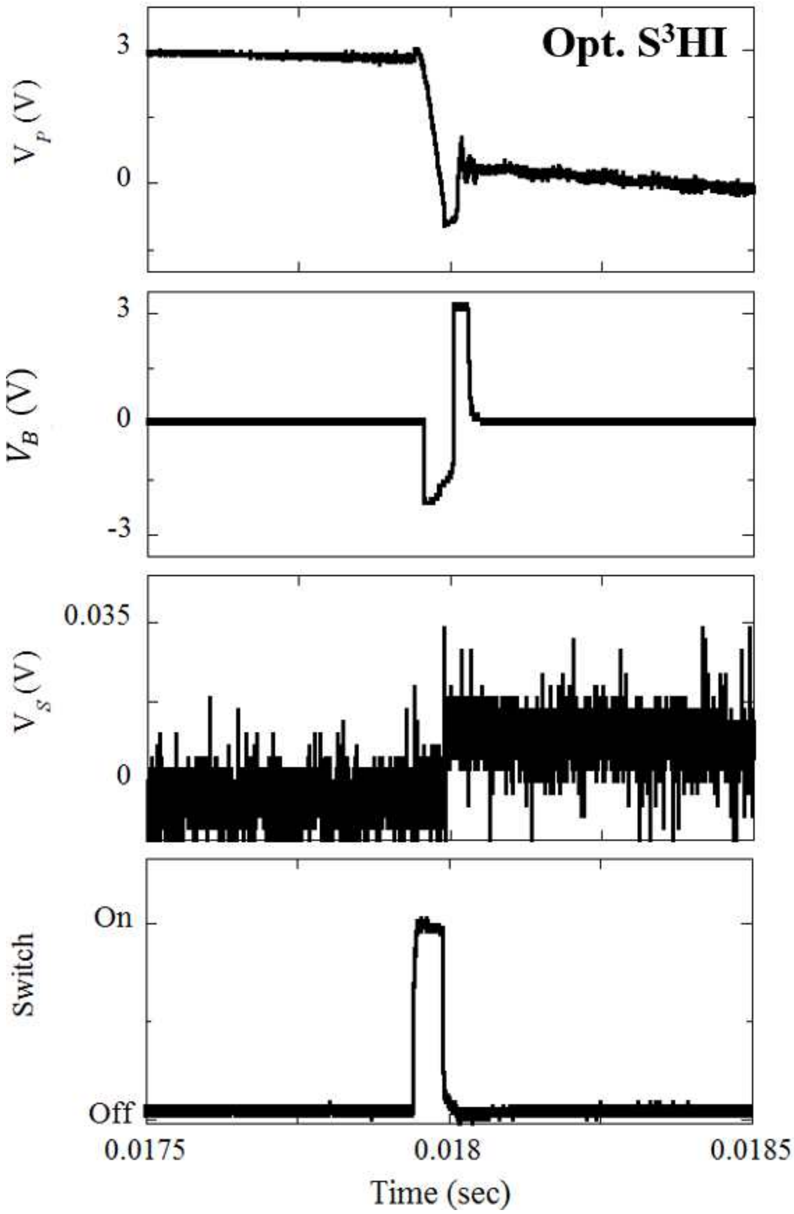

Fig. 55 Close-up Views of the Time Histories for Piezo-induced Voltage, V_p, Boosted Voltage, V_B, Stored Voltage, V_s, and Switch Status of S^3HI Strategy

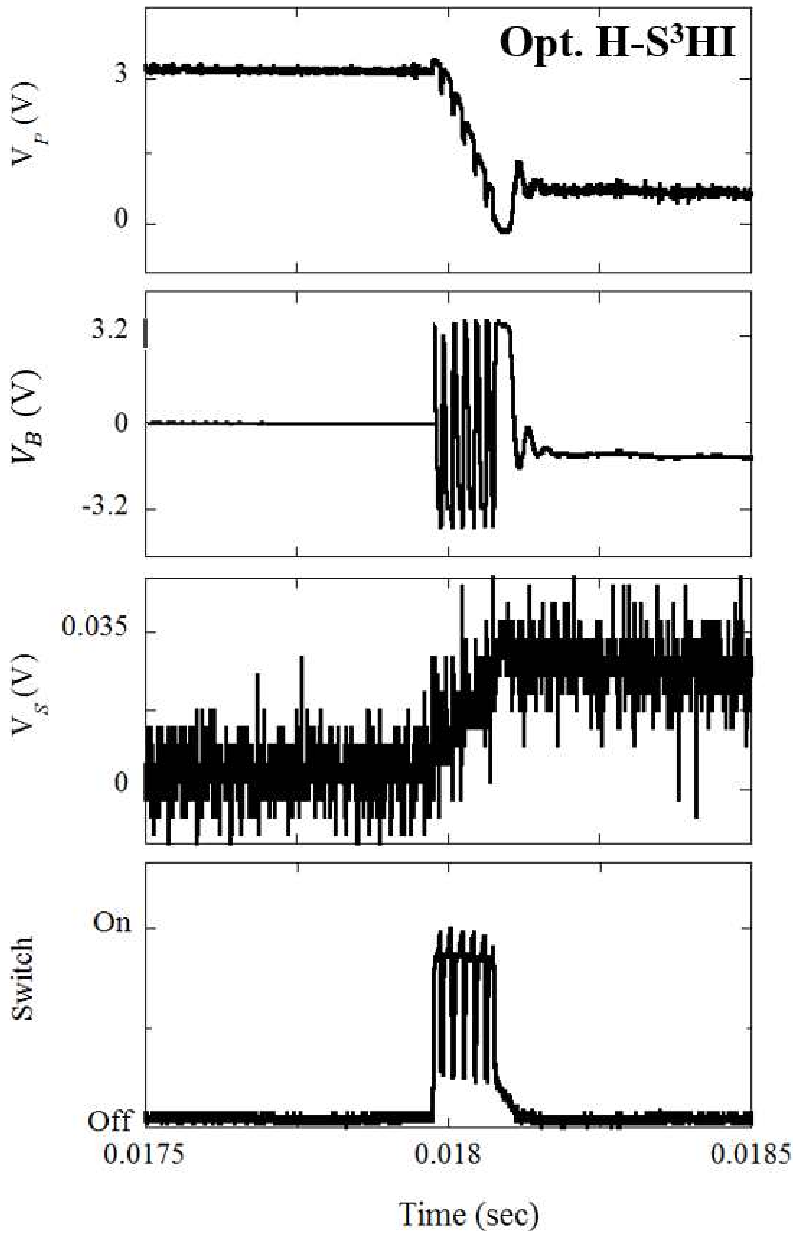

Fig. 56 Close-up Views of the Time Histories for Piezo-induced Voltage, V_p, Boosted Voltage, V_B, Stored Voltage, V_s, and Switch Status of H-S^{3}HI Strategy

Figure 53 shows the time history of the stored voltage, V_s, for each switching strategy. In addition, the numerical simulation results are also plotted in this figure to evaluate the validity of the numerical simulation model shown in Fig. 16. As can be seen in Fig. 53, the overall tendencies of the numerical simulation results are in good agreement with the experimental results. Therefore, the established simulation model can be further used to predict the overall harvesting capability of the proposed switching strategy in combination with the piezoelectric harvester. On the other hand, after analyzing the experimental results, we concluded that the SSHI strategy can be used to charge the stored voltage up to approximately 3.1 V at approximately 1.5 s, subsequently it gradually goes down. This phenomenon in which the storage voltage decreases indicates that the energy balance between charge and discharge is disproportionate on account of the energy dissipation because of the load resistance and the weak harvesting capability of the SSHI strategy. On the other hand, in the S^3HI case, the storage voltage saturates at around 3.5 V, but no decreasing trend could be seen because of the superior harvesting capability of the surging mechanism, which yields a high voltage in order to overcome the charging requirement, $|V_B| \geq V_{fw} + V_s$. As for the H-S^3HI strategy, it possesses the greatest stored voltage compared with the other switching strategies, and its voltage level reached up to 6.1 V. This value is much higher than that obtained with the S^3HI strategy by a factor of 1.7. In terms of stored energy, calculated as $(1/2)C_s V_s^2$, the H-S^3HI strategy yielded 87.4 uJ, while the S^3HI strategy yielded 28.8 uJ. Clearly, the H-S^3HI strategy results in greater stored energy and represents a three-fold increase in energy storing capability over the S^3HI strategy. This superiority is owing to maximizing the incoming energy to the inductor with a relatively longer switching duration in the H-S^3HI case compared with the S^3HI case, while still maintaining the surge-inducing mechanism, as we intended in this study.

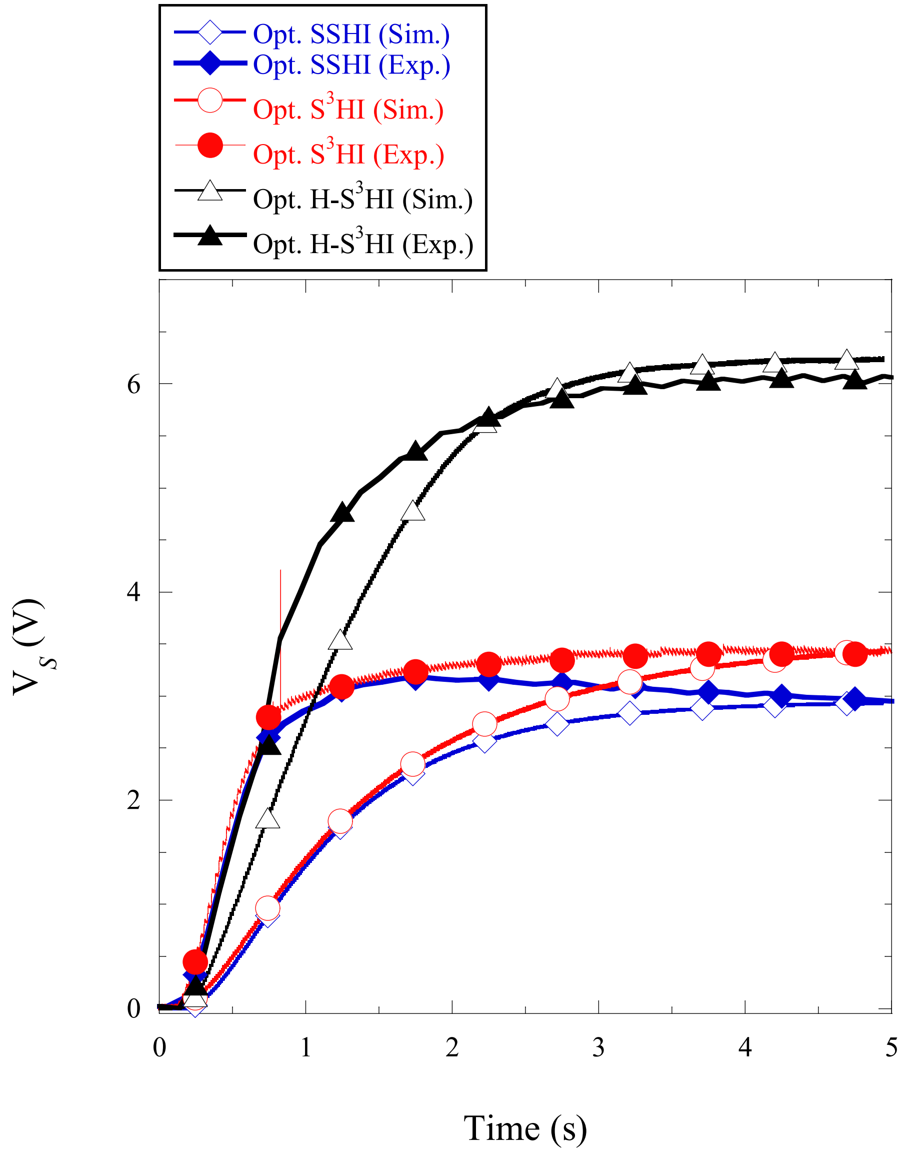

Fig. 57 Time History of Stored Voltage, V_s, obtained from Experiments and Numerical Simulations with respect to Each Switching Strategy

Most vibration energy sources in the real world, in fact, cannot be specialized in a single frequency; they instead have spectra of various frequencies. As an example, satellites experience random mechanical vibrations during lift-off, which can be characterized from 20 to 2000 Hz [52-55]. In addition, satellite on-board appendages that exhibit rotating movements during their on-orbit operations, such as reaction wheels, gimbal antennas, and control moment gyroscopes, induce wide-frequency-range micro-vibration disturbances. However, these vibration sources with wide frequency spectra can be also regarded as a potential renewable energy source. Therefore, in this study, we investigated the feasibility of harvesting wide–frequency-range micro-vibrations, so-called random vibrations, by employing the H-S^3HI strategy. Moreover, the other switching strategies, i.e. SSHI and S^3HI, are also employed in the investigation for the comparison reason. In these random-vibration harvesting tests, vibratory input with a flat power spectral density (PSD) of 0.1 g2/Hz from 1 to 2000 Hz was induced to the piezoelectric harvester as an external random vibration source.

Figure 54 shows the input and output responses when such a random vibration was induced to the piezoelectric harvester. In this result, it can be observed that the input PSD represents the flat responses over the frequency ranged from 1 to 2000 Hz, otherwise the output response has its peak at around the 30 Hz. This 1^{st} eigenfrequency of the piezoelectric harvester was slightly lower than that of the designed 1^{st} eigenfrequency of 40 Hz because an accelerometer was attached to the piezoelectric harvester to achieve the output response. Thereby, the result shown in Fig. 54 is agreeable. Meanwhile, in terms of random-vibration energy, it can be noted that the input and output were 0.19 grms and 0.58 grms, respectively.

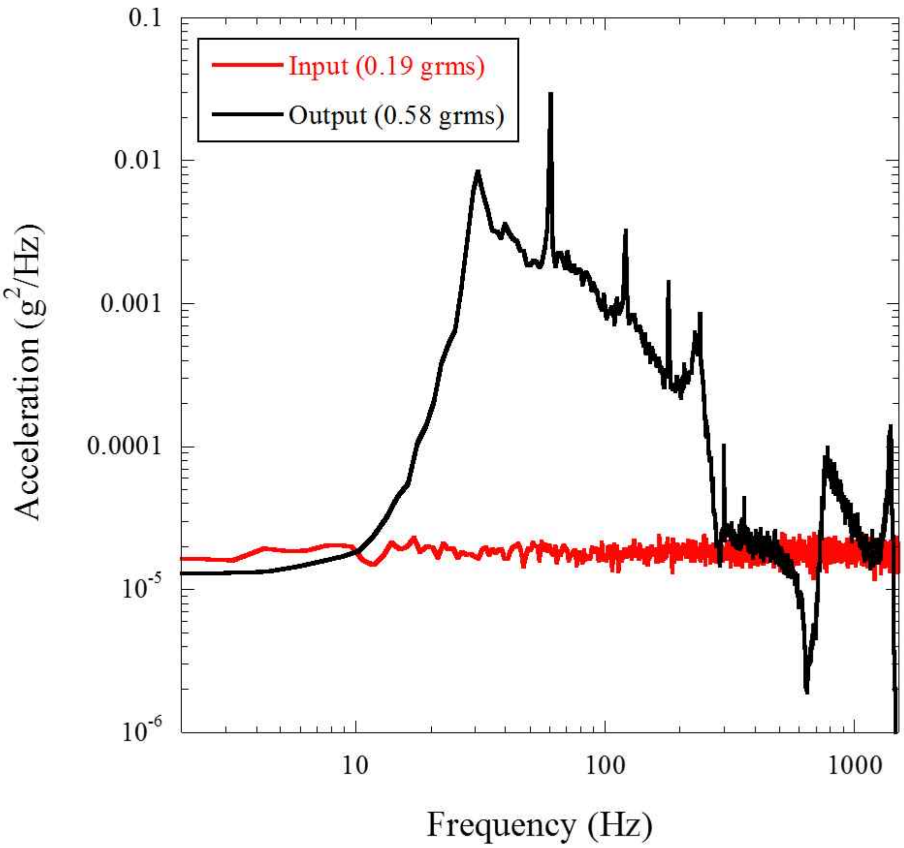

Fig. 58 Input and Output Responses when Random Vibration was induced to Piezoelectric Harvester

During random-vibration harvesting, however, it was hard to implement synchronous switching in accordance with random vibration signals. This means that the switching control scheme shown in Eq. (4-1), i.e., switch is turned on when $t_{on} = t_{|x_{\max}|}$, cannot be implemented. Therefore, during random-vibration harvesting, the switch was designed to be turned on at a specific switching frequency according to preliminary trade-off studies. The selected switching frequency, which exhibited the best harvesting performance of the H-S^3HI, was twice of the 1st eigenfrequency of the piezoelectric harvester, i.e., switching frequency = 80 Hz as shown in Fig. 55. This was so because the dominant response of the piezoelectric harvester occurs at 40 Hz even if the piezoelectric harvester is subjected to random vibration excitations, which implies that the period between the maximum and minimum responses of the piezoelectric harvester was 80 Hz. As for the switching duration, we simply applied the pre-defined switching control schemes for each switching strategy, i.e., S^3HI = 390 us, SSHI and H-S^3HI = 530 us.

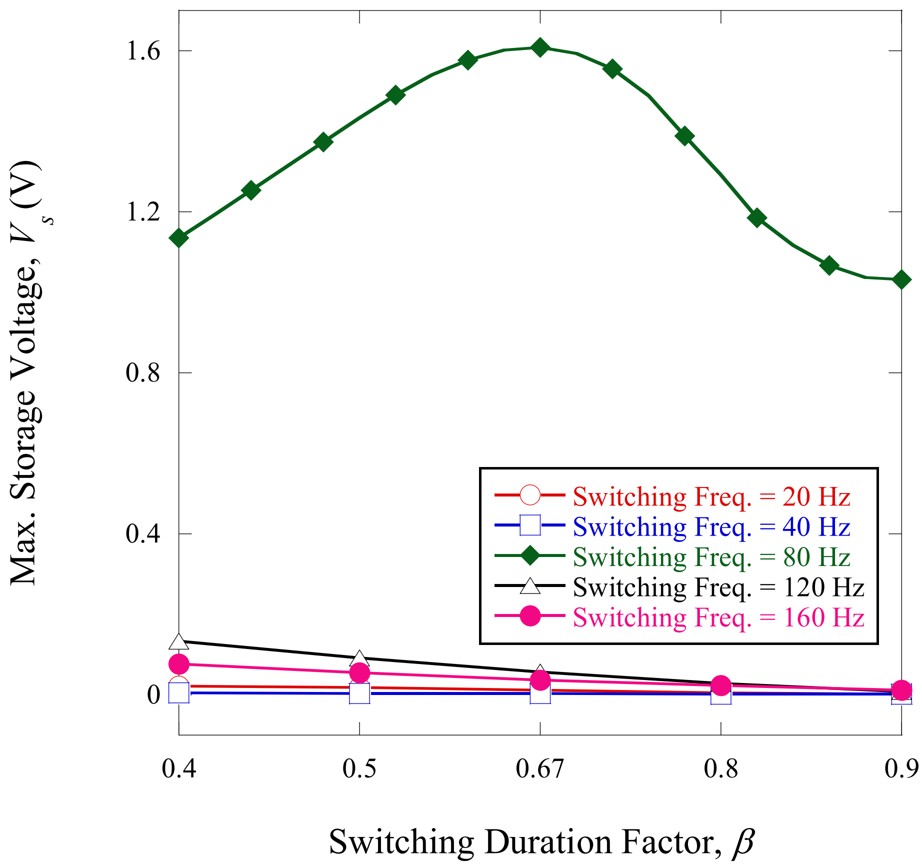

Fig. 59 Maximum Storage Voltage of H-S^{3}HI Strategy under Random Vibration, as a Function of Switching Duration Factor β and Switching Frequency

Figures 56, 57, and 58 show the overall view of time histories for SSHI, S^3HI, and H-S^3HI strategies under random vibration excitations of the piezo-induced voltage, V_p, the boosted voltage, V_B, the storage voltage, V_s, and the switch status. During these tests, switching was continuously executed according to a predefined switching frequency of 80 Hz for all switching strategies, but the switching duration applied the pre-defined switching control schemes for each switching strategy, i.e., S^3HI = 390 us, SSHI and H-S^3HI = 530 us. As can be seen in figures, no increase in V_s can be observed in SSHI case, otherwise the S^3HI, and H-S^3HI strategies that employe the surge-inducing mechanism exhibits some increase trend in V_s.

Figure 59 shows the representative closed-up view of the H-S^3HI. In this figure, it can be noted that surging behavior occurs continuously at every instance of high-frequency switching, regardless of the random vibration signals as intended. In line with every surging voltage at V_B, the storage voltage, V_s, goes up gradually, and its trend is almost the same as that from the results obtained from the sinusoidal vibration tests, shown in Fig. 52. Thereby, it can be said that the proposed H-S^3HI strategy is effective in harvesting the random vibration energy.

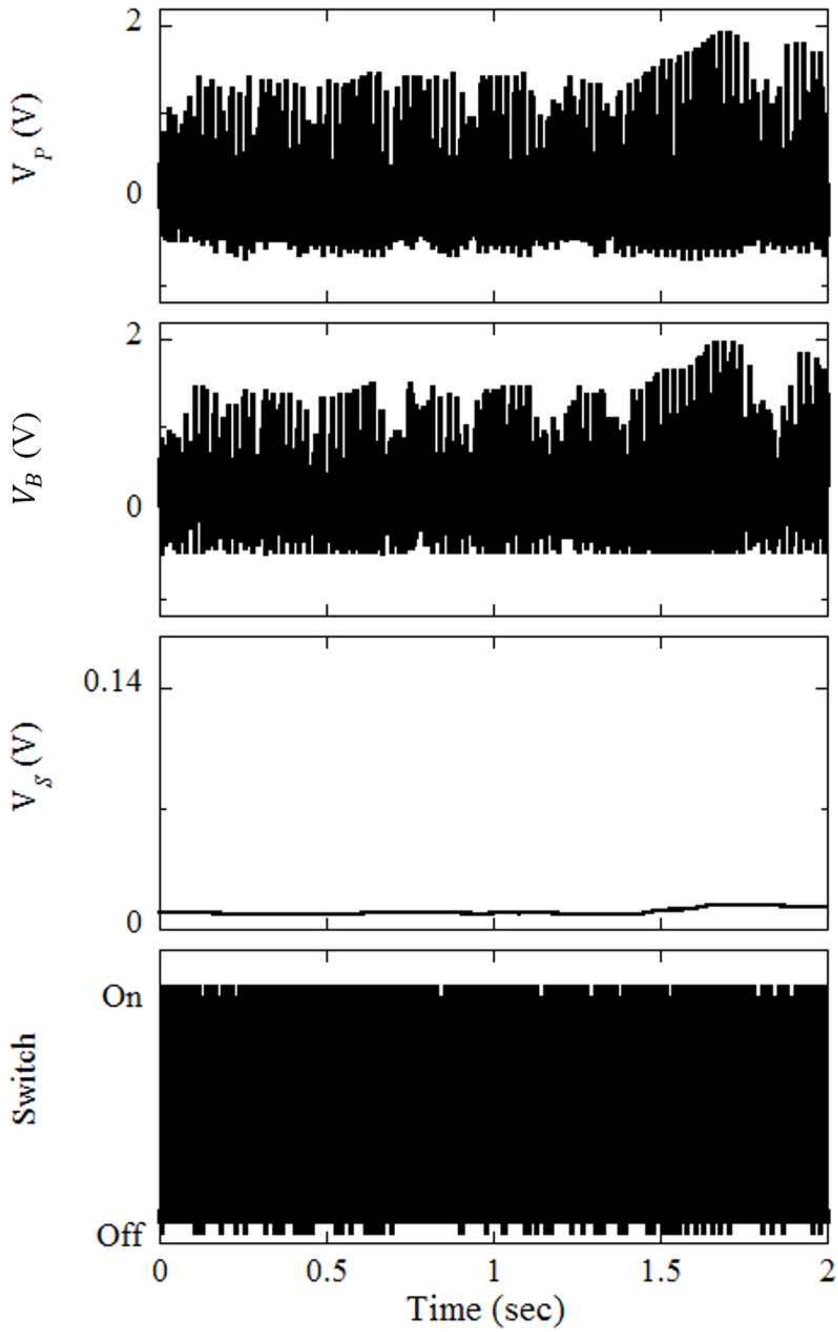

Fig. 60 Time Histories for SSHI Strategy under Random-Vibration Excitation for Piezo-induced Voltage, V_p, Boosted Voltage, V_B, Stored Voltage, V_s, and Switch Status

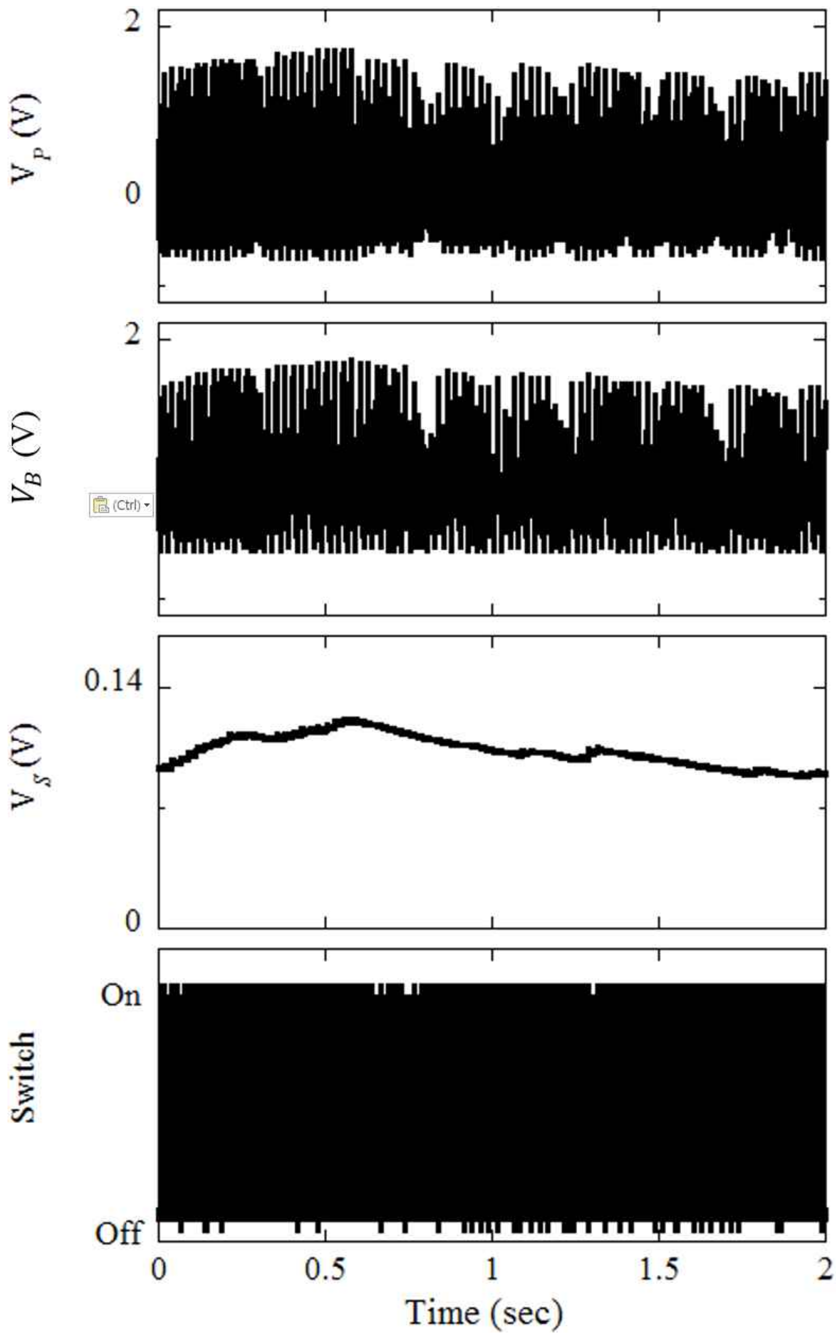

Fig. 61 Time Histories for S[3]HI Strategy under Random-Vibration Excitation for Piezo-induced Voltage, V_p, Boosted Voltage, V_B, Stored Voltage, V_s, and Switch Status

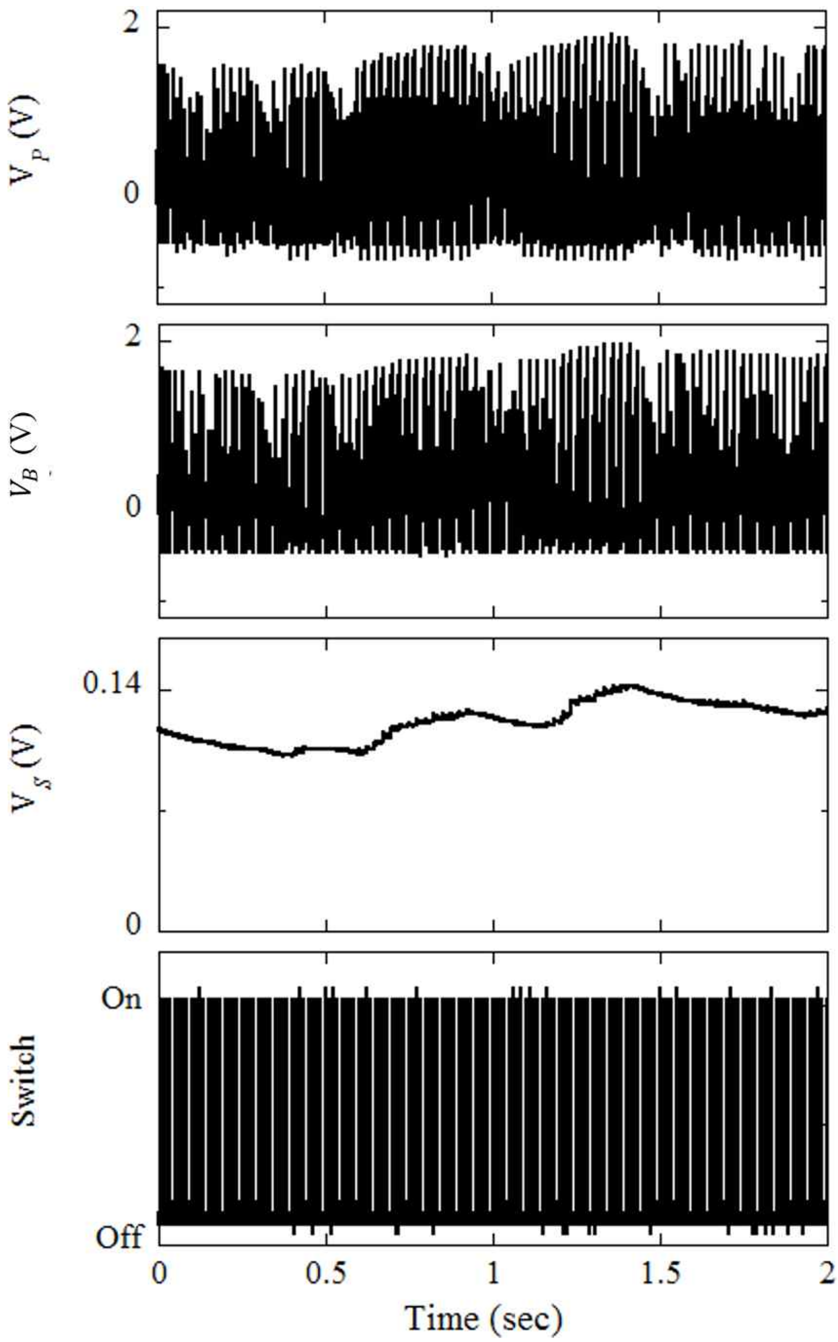

Fig. 62 Time Histories for H-S^{3}HI Strategy under Random-Vibration Excitation for Piezo-induced Voltage, V_p, Boosted Voltage, V_B, Stored Voltage, V_s, and Switch Status

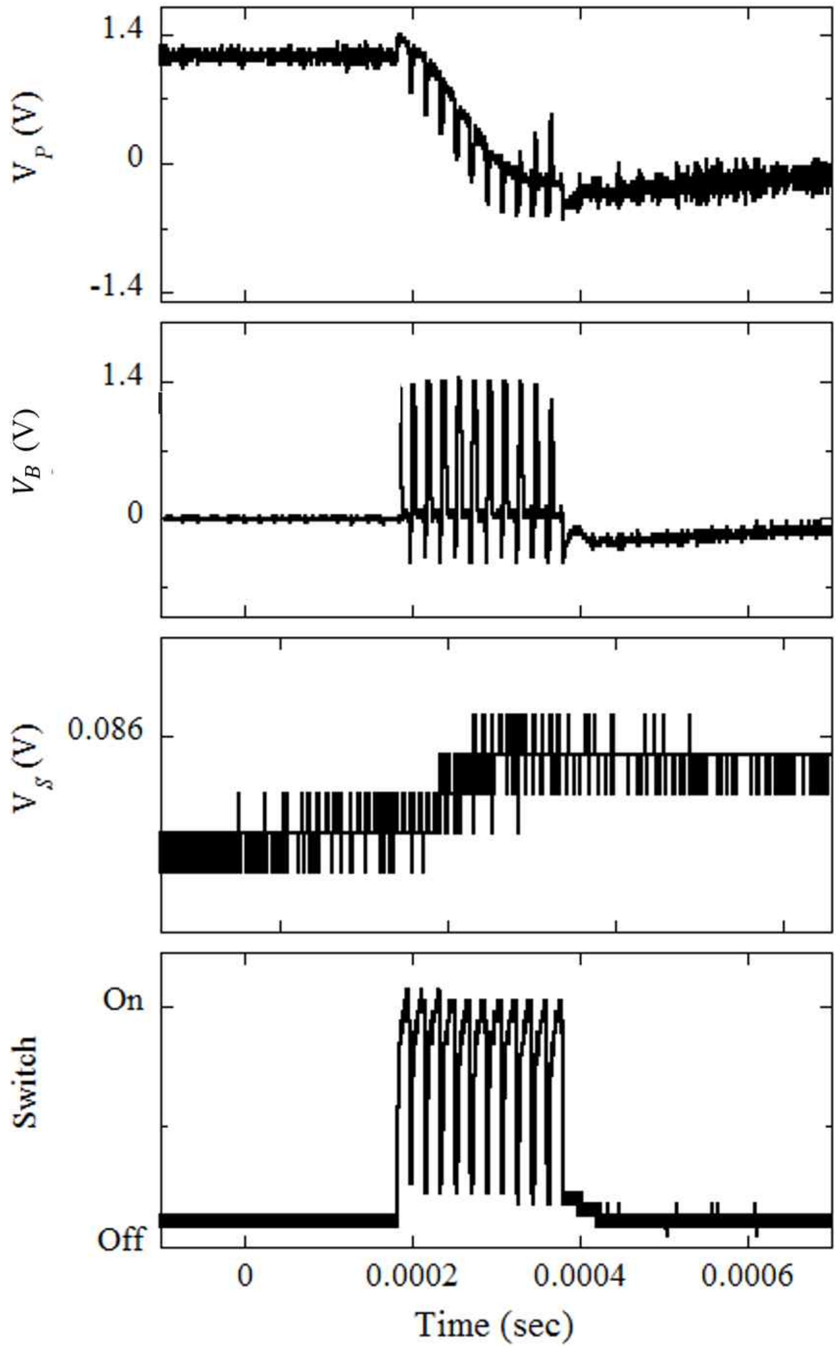

Fig. 63 Representative Closed-up Histories for H-S³HI Strategy under Random-Vibration Excitation for Piezo-induced Voltage, V_p, Boosted Voltage, V_B, Stored Voltage, V_s, and Switch Status

Figure 60 shows the time history of the storage voltage, V_s, under random-vibration excitation conditions for each switching strategy. As shown in the figure, the SSHI strategy cannot properly charge the storage capacitor because it was designed to be optimal taking into account that predictable vibration excitations, such as sinusoidal vibration, would be present. On the other hand, the results obtained with the S^3HI and H-S^3HI strategies in which the surging mechanism within circuit C was employed show that the stored voltage level gradually increased, even if its increasing trend was random, unlike the case in which the piezoelectric harvester was subjected to a sinusoidal excitation as shown in Fig. 53. However, these surge-based switching strategies exhibited feasible energy harvesting capabilities, and the stored voltage level can be taken into account as a potential power source. However, in the experiments, it should be noted that the stored voltage levels obtained with the S^3HI and H-S^3HI strategies, while indicating a by far better performance compared with the SSHI strategy, did not show distinguishable differences because the high-frequency switching aspect of H-S^3HI could not fully leverage its advantages under random-vibration excitation conditions. This fact also can be explained from the results shown in Fig. 49, in which it can be seen that H-S^3HI has an effective force level for exploiting its full potential. However, in terms of energy calculated as $(1/2)C_s V_s^2$, the H-S^3HI strategy yielded 9.4 uJ. Therefore, considering that the abovementioned nano-watt level vibration sensor [31] barely dissipates power at a rate of 0.7 nW/h, the H-S^3HI strategy could be applicable even under random-vibration excitations. Consequently, it can be said that the H-S^3HI strategy has the following advantages during random-vibration harvesting: this strategy only requires a very simple system because it does not need any feedback control, and it does not need to detect the extrema of the piezoelectric displacement to execute the switching action. These are the key advantages of the H-S^3HI strategy for practical applications in the real world.

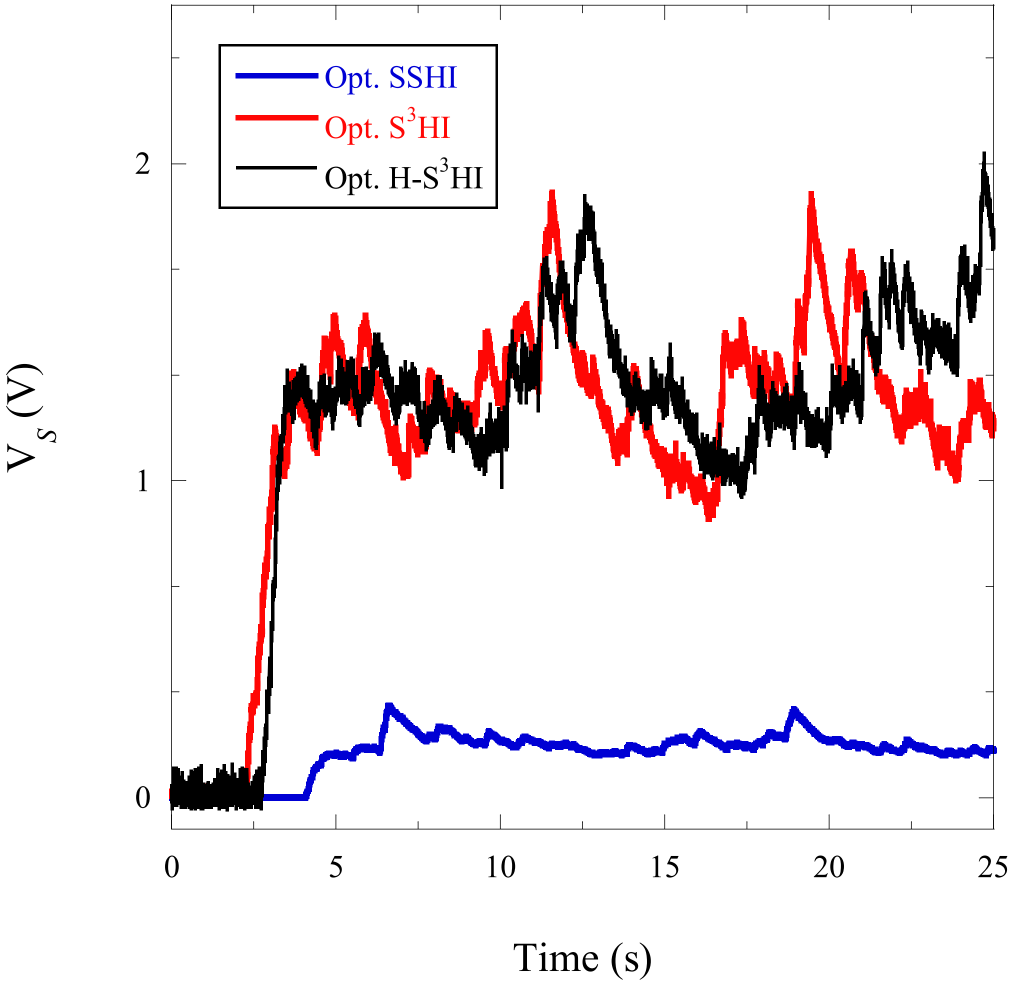

Fig. 64 Time History of Stored Voltage, V_s, under Random-Vibration Excitation with respect to Each Switching Strategy

V. Performance Evaluation on Complex System Level

A. System Configuration

To investigate the feasibility of using the H-S^{3}HI strategy for harvesting cooler-induced micro-vibration energy, a numerical simulation model is established, as shown in Fig. 61. This simulation model is mainly composed of a cooler that induced mechanical micro-vibrations, a passive cooler vibration isolator with low stiffness to support the cooler [56], and a pair of piezoelectric energy harvesters (Hereafter, this model will be called a complex system). In this model, m_1 indicates the mass of the cooler (3.8 kg), and the dashpot element c_1 (7.95 Ns/m) and spring element k_1 (14.408 N/mm) indicate the damping coefficient and stiffness of the passive vibration isolator [56], respectively. The reason why the passive vibration isolator was employed in this system will be discussed in the upcoming results.

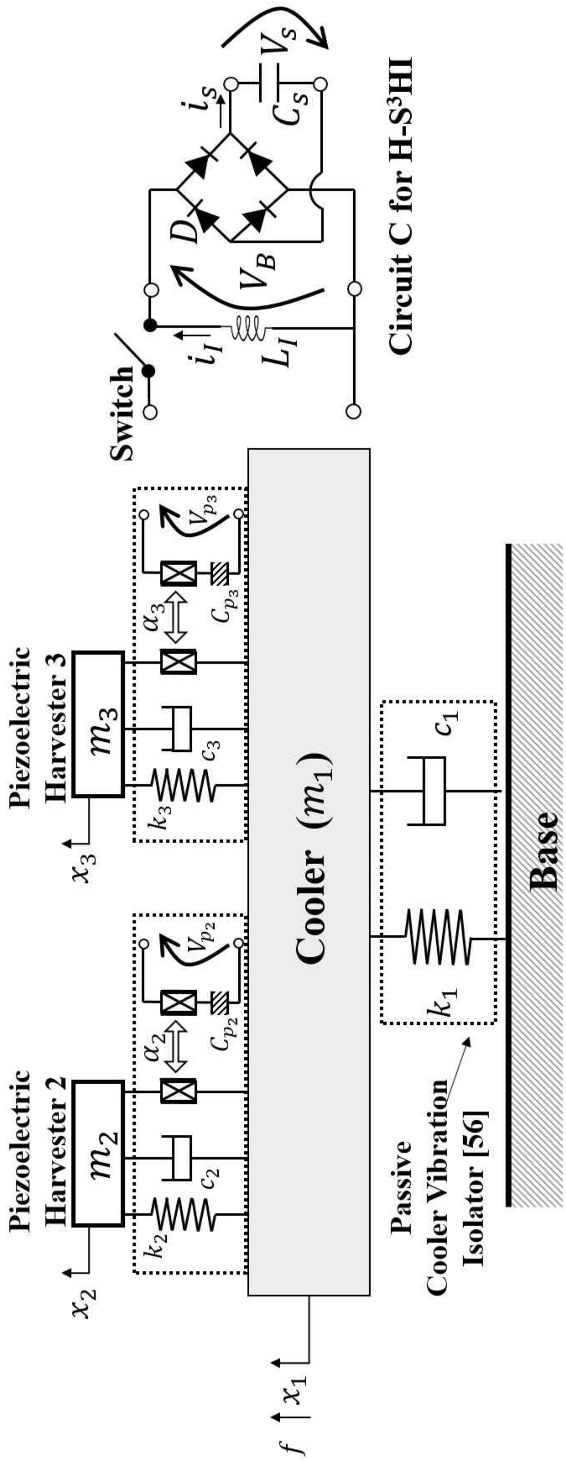

Fig. 65 Numerical Simulation Model of Complex System

1. Passive Cooler Vibration Isolator [56]

In this study, a passive cooler vibration isolator shown in Fig. 62 is dedicatedly employed to support the cooler with a low. This combination enables the complex system to maximize the efficiency of the piezoelectric harvester by substantially improving the deflections acting on the piezoelectric harvester itself. As basic descriptions, the isolator combined with the cooler, as shown in Fig. 63, can guarantee the structural safety of both a cooler supported by the low-stiffened isolator and the isolator itself under severer launch environments without applying a holding-and-release mechanism, while effectively isolating the micro-vibration induced by cooler operations in on-orbit. This strategy is already verified in the previous study [56] and achieved by employing a pseudoelastic shape memory alloy (SMA)-based blade in the isolator design, thereby making it a smart adaptive system that varies its eigenfrequency and damping characteristics in compliance with a given vibration environment. In this study, the assessment of the complex system was conducted under an assumption that it operates in on-orbit conditions. Therefore, the parameter values of k_1 and c_1 of the isolator are based on this assumption.

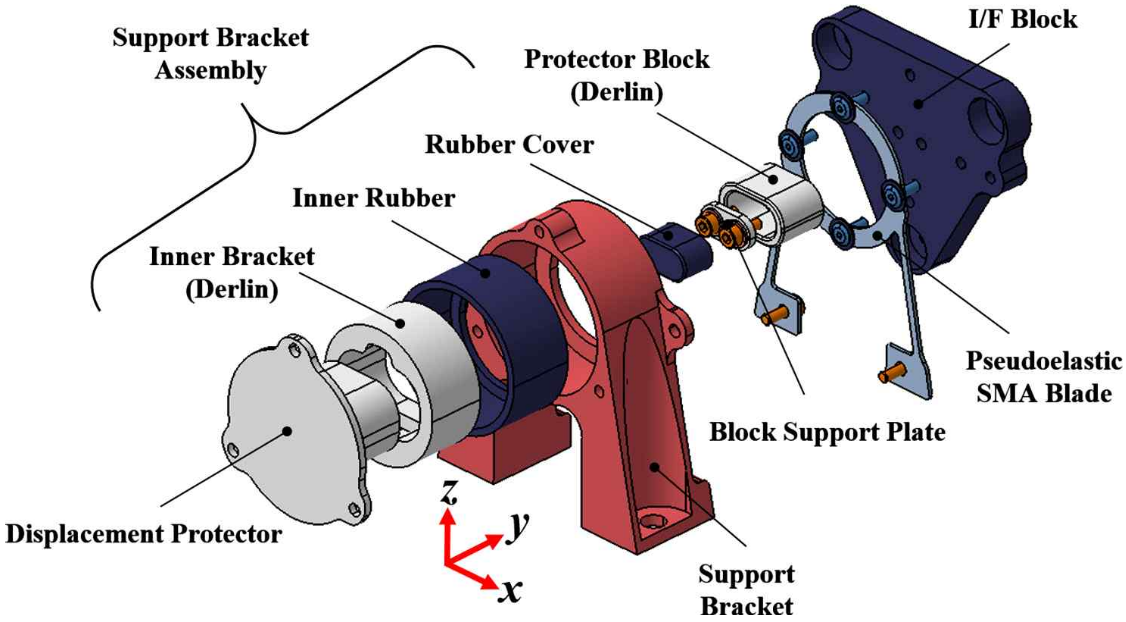

Fig. 66 Passive Cooler Vibration Isolator employing Pseudoelastic SMA Blade [56]

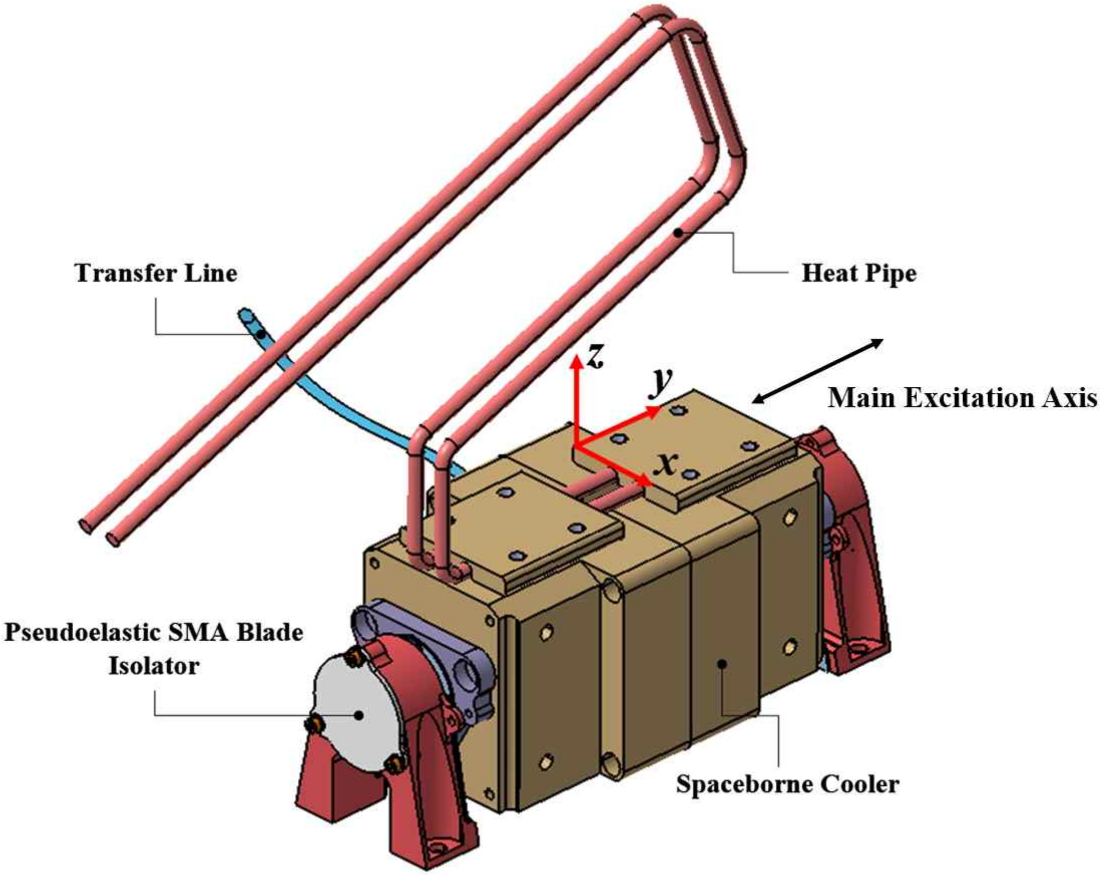

Fig. 67 Cooler Assembly combined with Passive Cooler Vibration Isolator [56]

2. Governing Equation of Motions

Equations of motion of the complex system are derived based on Fig. 61 to assess the energy harvesting capability of the H-S^{3}HI strategy that employs circuit C. As mentioned above, the micro-vibration induced by the cooler operation is of singular frequency and given as following:

$$f = f_0 e^{iwt} \tag{5-1}$$

where, f_0 and w denote the amplitude and excitation frequency of the cooler, respectively. In this study, the external force f_0 induced by the cooler is set as 2.5 N with an excitation frequency of 40 Hz. On the other hand, once the displacements of the cooler and the piezoelectric harvesters are defined as x_1, x_2, and x_3 respectively, the equations of motion for the complex system can be defined as follows:

$$\begin{aligned} m_1\ddot{x}_1 + c_1\dot{x}_1 + k_1 x_1 + c_2(\dot{x}_1 - \dot{x}_2) + c_3(\dot{x}_1 - \dot{x}_3) \\ + k_2(x_1 - x_2) + k_3(x_1 - x_3) = f + \alpha_2 V_{p_2} + \alpha_3 V_{p_3} \end{aligned} \tag{5-2}$$

$$m_2\ddot{x}_2 + c_2(\dot{x}_2 - \dot{x}_1) + k_2(x_2 - x_1) = -\alpha_2 V_{p_2} \tag{5-3}$$

$$m_3\ddot{x}_3 + c_3(\dot{x}_3 - \dot{x}_1) + k_3(x_3 - x_1) = -\alpha_3 V_{p_3} \tag{5-4}$$

$$i_{p_2} = \alpha_2(\dot{x}_2 - \dot{x}_1) - C_{p_2}\dot{V}_{p_2} \tag{5-5}$$

$$i_{p_3} = \alpha_3(\dot{x}_3 - \dot{x}_1) - C_{p_3}\dot{V}_{p_3} \tag{5-6}$$

where, m_1 denotes the cooler mass, m_2 and m_3 denotes the mass of each piezoelectric harvester. V_p, α, and i_p denote the piezo-induced voltage, mechanical-electrical transformation factor and the current out of the piezoelectric harvester, respectively. In addition, the subscripts $_2$ and $_3$ on the parameters of the piezoelectric harvester indicate each piezoelectric harvester, respectively. On the other hand, both piezoelectric harvesters can make a electrical connection with either parallel or series together, then its connection is again connected with the circuit C to effectively harvester the cooler-induced micro-vibration energy by employing the H-S^{3}HI strategy. The identified parameter values of the cooler, and each piezoelectric harvester are summarized in Table 4.

Table 4 Specifications of Complex System

Property		Symbol	Values
Cooler	Cooler Mass (kg)	m_1	3.8
Vibration Isolator [56]	Stiffness (N/mm)	k_1	14.408
	Damping Coefficient (Ns/m)	c_1	7.95
Piezoelectric Harvester 2	Tip Mass (g)	m_2	27.7
	Capacitance (nF)	C_{p_2}	129.1
	Equivalent Stiffness (N/mm)	k_2	1.931
	Equivalent Damping Coefficient (Nsec/m)	c_2	0.1690
	Mechanical Electrical Transformation Factor (N/V)	α_2	0.111
Piezoelectric Harvester 3	Tip Mass (g)	m_3	27.7
	Capacitance (nF)	C_{p_3}	127.9
	Equivalent Stiffness (N/mm)	k_3	1.918
	Equivalent Damping Coefficient (Ns/m)	c_3	0.1728
	Mechanical Electrical Transformation Factor (N/V)	α_3	0.105

B. Numerical Simulation

1. Simulation Result

Figure 64 shows the numerically achieved transmitted force and storage voltage for the complex system, with respect to with and without isolation condition. In here, the condition without the isolation means that the cooler is rigidly fixed on the base, thus the cooler-induced micro-vibration disturbances are directly transmitted to the base. In this rigid condition, the maximum transmitted force level is 2.5 N and its micro-vibration disturbances from the cooler could significantly degrade the image quality of the high-resolution observation satellite. In this condition, no effective energy harvesting capability can be expected as well because the deflections acting on the piezoelectric harvesters are tremendously diminished by the rigidly fixed condition of the cooler. On the other hand, under the condition with the isolation, the storage voltage with H-S^3HI strategy reaches approximately 10.35 V which is by far higher than the condition without the isolation by the factor of 10. As a result, it can be said that the complex system with the isolation condition can guarantee the hybrid demands of both effectively isolating the micro-vibration to comply with the strict micro-vibration requirement and promisingly harvesting the cooler-induced micro-vibration as a renewable energy.

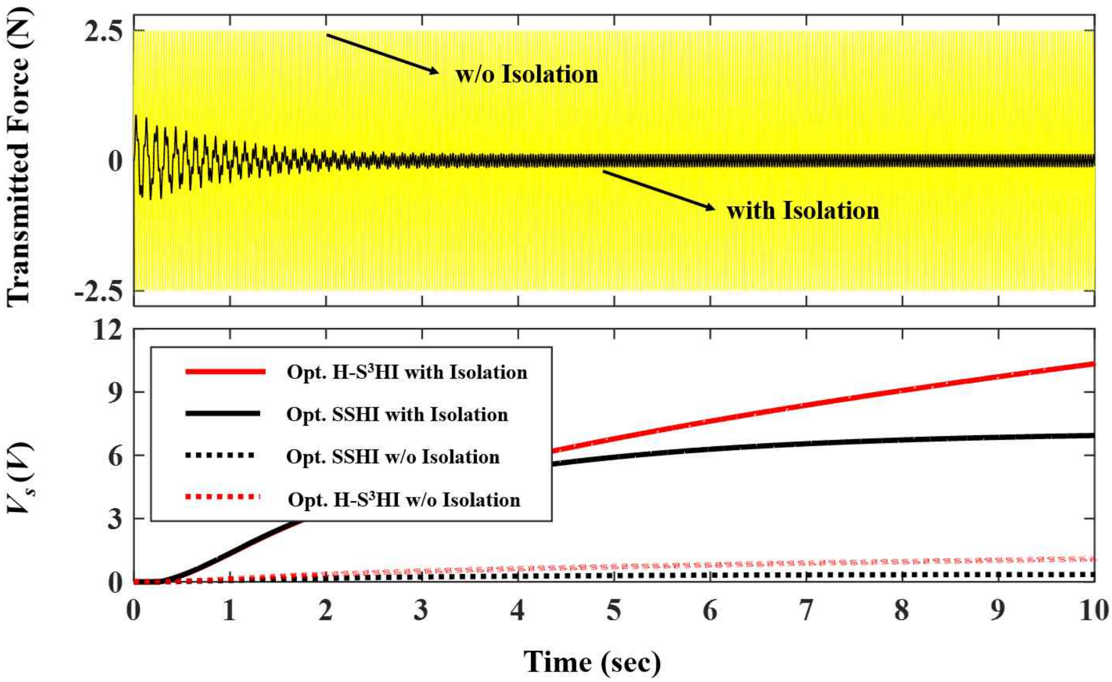

Fig. 68 Time History of Transmitted Force and Storage Voltage for Complex System, with respect to with and without Isolation Condition

C. Experimental Validation

1. Test Set-up

To evaluate the feasibility of harvesting the cooler-induced micro-vibration energy by using the proposed H-S^3HI strategy, energy harvesting tests at the complex system level were carried out. Figure 65 shows the entire test setup for the complex system level tests. This test setup is mainly composed of the complex system combined with a pair of piezoelectric harvesters at both sides, the kistler table to measure the transmitted force from the cooler-induced micro-vibration, the distribution board for either parallel or series connection of the piezoelectric harvester, and the circuit for H-S^3HI strategy. In the test set-up, the kistler table was dedicatedly manufactured in laboratory scale. This kistler table is mainly composed of a air-floating-type customized surface plate (VKP-0606-800H, IVIC) which has a size of 600 × 600 × 800 mm, totally 4 three-axis load cells (MC15-3A-100, DACELL), and an air compressor (LX110HPDP, LG). The air compressor inputs the compressed air to the air spring implemented under the surface plate, thereby the surface plate can be floated and no vibration disturbances from outside can be transmitted on the surface plate. In the test, the transmitted forces from the cooler to the kistler table was achieved by summarizing the achieved data for each of 4 load cells. Then, data achievement and handling were controlled by Labview software.

As already mentioned in above Fig. 34, the sinusoidal signal generated from the function generator and transmitted via the power amplifier was induced to the cooler, thereby desirable excitation force and frequency could be achieved. The function generator also provided the switching trigger signal for H-S^3HI, forwarded to the switching circuit. Both piezoelectric harvesters were connected in either parallel or series via the distribution board and this board was again connected to the switching circuit to deliver the piezo-induced electrical energy resulted from the cooler-induced micro-vibration energy. In this study, the abovementioned switching circuit and the peripherals were powered by an external DC/DC supply, because the aim of this test was not to implement a stand-alone self-powered system, but to demonstrate the performance of the H-S^3HI strategy in harvesting the cooler-induced micro-vibration.

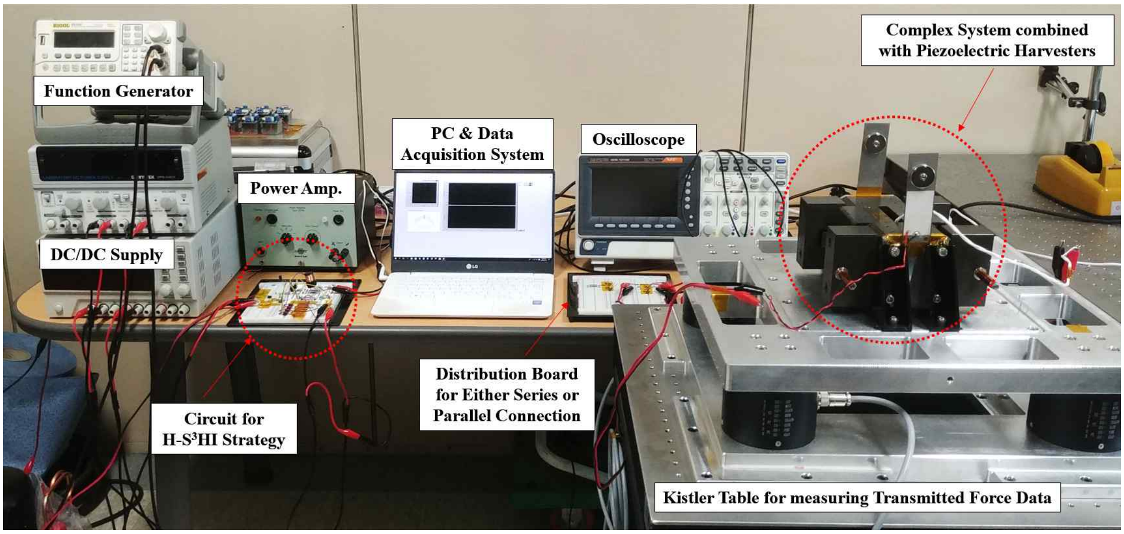

Fig. 69 Entire Test Set-up for the Complex System Level Performance Evaluation Tests of Energy Harvesting and Micro-vibration Isolation

2. Cooler-induced Micro-vibration Harvesting

a. Parallel Connection of Harvesting Circuit

Under a parallel connection condition of the piezoelectric harvesters, the feasibility test of harvesting the cooler-induced micro-vibration by exploiting the full potential of the H-S^{3}HI strategy was performed at the complex system level as shown in Fig. 65. The SSHI strategy was also employed in such a test for the purpose of comparisons with the results obtained from H-S^{3}HI strategy.

Figure 66 shows the overall views of the time histories for the piezo-induced voltage, V_p, the boosted voltage, V_B, the stored voltage, V_s, and the switch status for the optimal SSHI and H-S^{3}HI strategies, respectively. As can be seen in the figure, all strategies invert their piezoelectric voltage, V_p, while the switch is kept on for their corresponding optimal switching durations. However, according to the switching strategy, it can be observed that the behaviors of V_p are quite different from each other. For example, H-S^{3}HI strategy, which use the surging effects for energy harvesting, keeps the transient voltage behavior resulting from variations of the piezoelectric harvester's displacement, namely $\alpha x/C_p$, during switch-off state. Otherwise, the SSHI strategy shows plateau behavior during switch-off state. The occurrence of such a plateau behavior in the SSHI strategy is caused by the energy transformation toward the storage capacitor. In case of H-S^{3}HI strategy, its energy transformation mechanism is the inductor-induced surging voltage observed at every switching instant in V_B. These addressed behavior are well in agreement with the numerically expected results shown in Fig. 47. On the other hand, once considering the increase trend in V_s, the H-S^{3}HI strategy shows that V_s gradually increases. Otherwise, the SSHI strategy shows the opposite trend compared to the H-S^{3}HI strategy because the energy harvesting capability of the SSHI strategy cannot meet the energy balance limits between charging energy and the dissipated energy into the resistor.

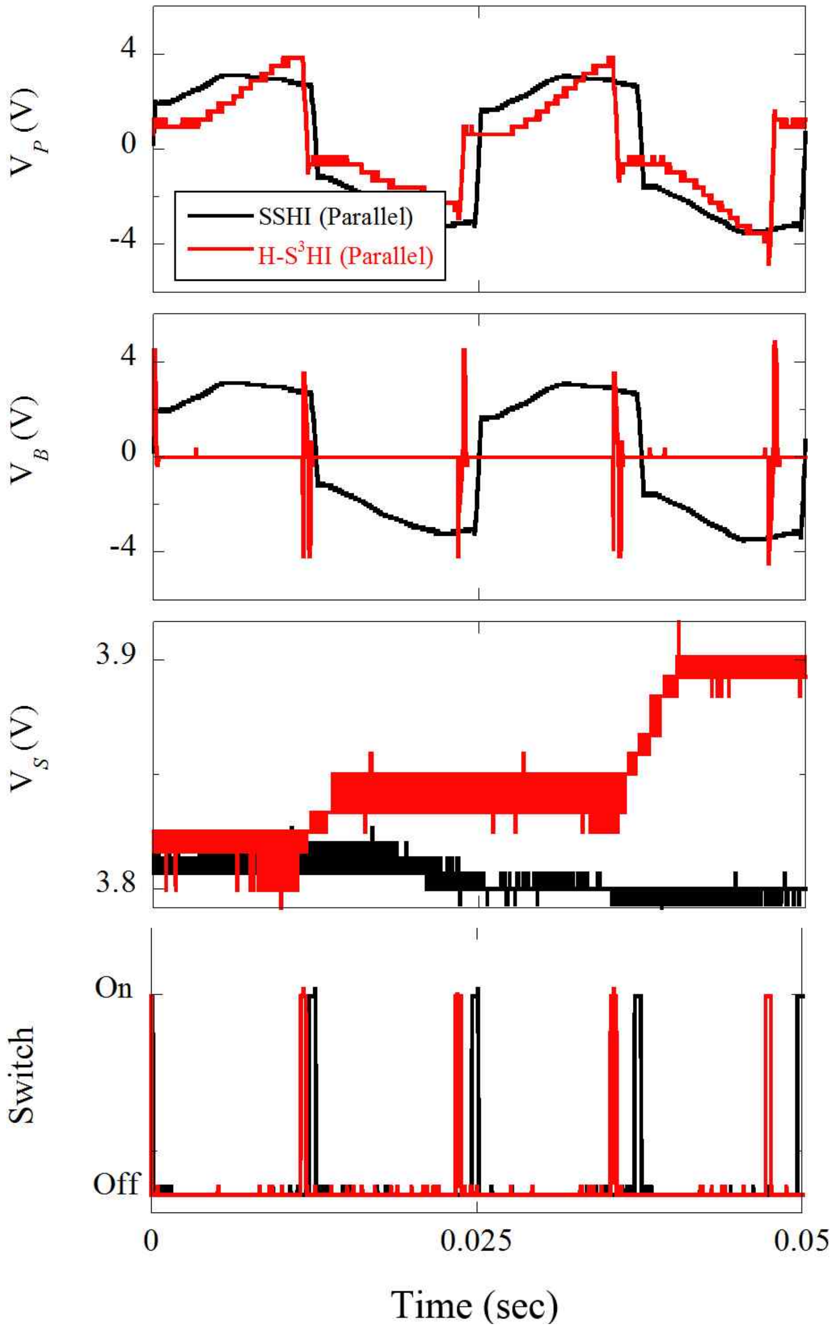

Fig. 70 Time Histories for optimal SSHI and H-S^{3}HI Strategies under Complex System Level Test with Parallel Connection, for Piezo-induced Voltage, V_p, Boosted Voltage, V_B, Stored Voltage, V_s, and Switch Status

Figure 67 shows the time history of the storage voltage, V_s, under the complex system level test with parallel connections of the piezoelectric harvesters, for optimal SSHI and H-S^{3}HI strategies. As shown in the figure, the condition with the isolation guarantees effective harvesting capability in both SSHI H-S^{3}HI strategies compared with the condition without isolation. This phenomenon is identical to the expected results from the numerical simulation shown in Fig. 64. However, it is obvious that each strategy exhibits a different storage voltage level. For instance, the SSHI strategy shows the saturation behavior at around 7 s and it is gradually decreases because the energy balance limits between charging energy and the dissipated energy into the resistor is distorted due to the weak harvesting capability of the SSHI. On the other hand, the H-S^{3}HI strategy exhibits the promising charging capabilities, and its stored voltage level is calibrated at 3 V which is relatively higher than that of the SSHI case by the factor of 1.5. In addition, the storage voltage level keeps its increasing trend without showing saturation behavior. If the charging time becomes longer than the result shown in this figure, much higher storage voltage by using the H-S^{3}HI strategy can be expected. Hence, it can be concluded that the H-S^{3}HI can guarantee the feasible energy harvesting capability from the cooler-induced micro-vibration.

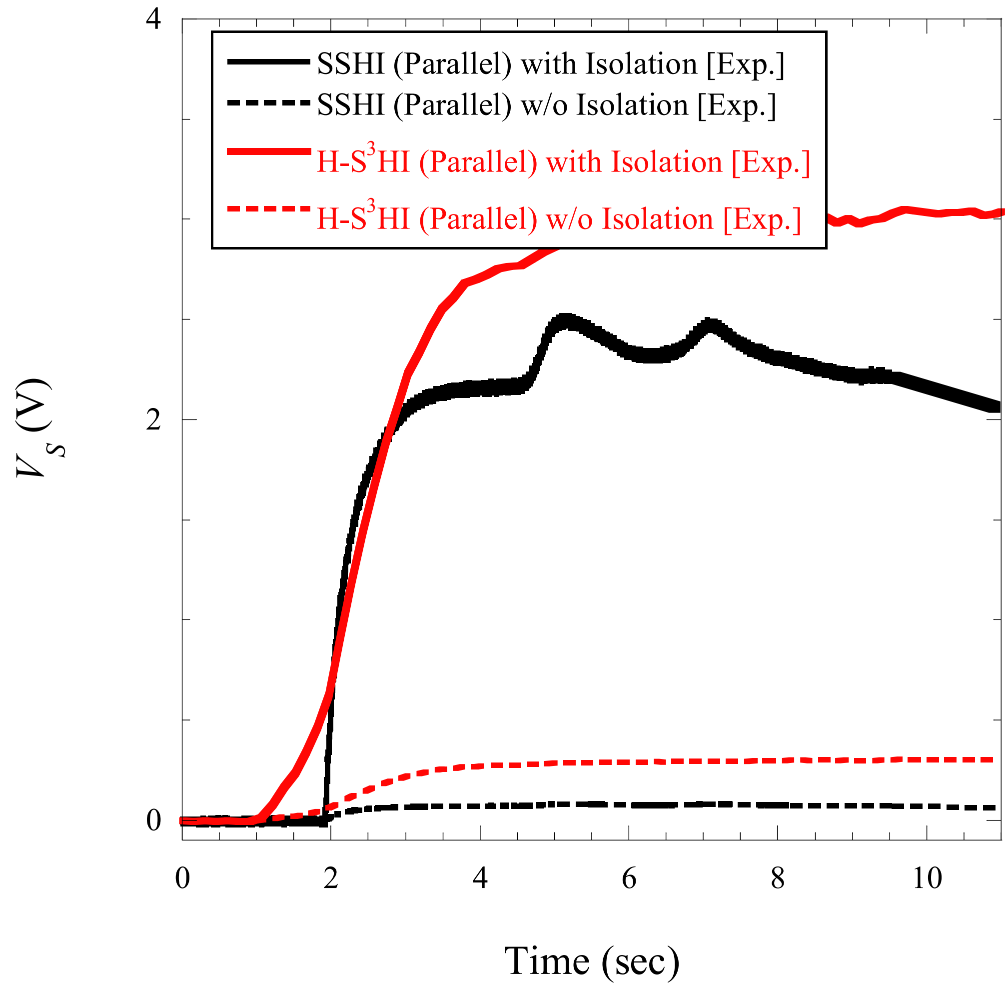

Fig. 71 Time History of Storage Voltage, V_s, under Complex System Level Test with Parallel Connections of Piezoelectric Harvester, for Optimal SSHI and H-S^3HI Strategies

b. Series Connection of Harvesting Circuit

Under a series connection condition of the piezoelectric harvesters, the feasibility test of harvesting the cooler-induced micro-vibration by exploiting the full potential of the H-S^3HI strategy was performed at the complex system level as well. The SSHI strategy was also employed in such a test for the purpose of comparisons with the results obtained from H-S^3HI strategy. Figure 68 shows the overall views of the time histories for the piezo-induced voltage, V_p, the boosted voltage, V_B, the stored voltage, V_s, and the switch status for the optimal SSHI and H-S^3HI strategies, respectively. As can be seen in the figure, the tendencies for all results are almost all the similar with the results obtained under the parallel condition shown in Fig. 66. However, it can be noted that the overall voltage levels are approximately 2 times higher than that of the parallel case. For example, V_s of the H-S^3HI strategies possesses approximately 8 V and its level is relatively higher than the parallel case by the factor of 2. Thereby, it can be said that the series condition for the piezoelectric harvester with the H-S^3HI strategy is much preferable in the energy harvesting capability point of view.

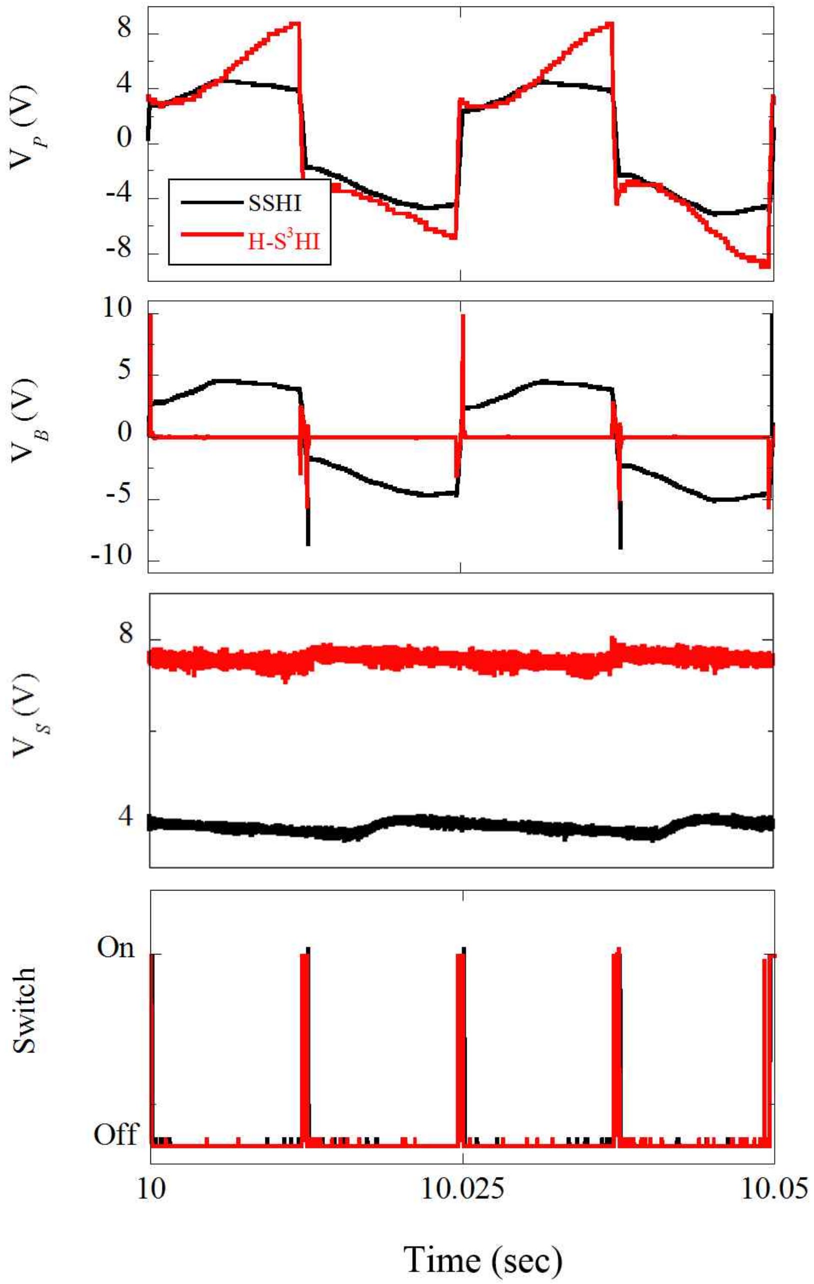

Fig. 72 Time Histories for optimal SSHI and H-S^{3}HI Strategies under Complex System Level Test with the Series Connection, for Piezo-induced Voltage, V_p, Boosted Voltage, V_B, Stored Voltage, V_s, and Switch Status

Figure 69 shows the time history of the storage voltage, V_s, under the complex system level test with the series connection of the piezoelectric harvesters, for optimal SSHI and H-S^{3}HI strategies. As addressed above, the series connection of the piezoelectric harvester possesses approximately 2 times higher storage voltage level than the results obtained from the parallel connection regardless of the switching strategy. In addition, it is obvious that the H-S^{3}HI strategy in the series connection is by far grater than the conventional SSHI strategy. These experimentally achieved results are well in agreement with the results obtained from the numerical simulation by using the governing equations of motion defined in Eqs. (5-2) ~ (5-6). Thereby, the established equations of motion can be further used to expect the efficiency of the H-S^{3}HI strategy. On the other hand, the results obtained from the rigid condition are also plotted in this figure. In here, the rigid condition indicates that the cooler is rigidly mounted on the kistler table without the low-stiffened isolator, but it is instead mounted on the kistler table with the rigid fixture as shown in Fig. 70. As can be seen the result, it is noted that the V_s levels in both SSHI and H-S^{3}HI cases with the rigid condition are significantly degraded compared with the condition with the isolator. Because the deflections acting on the piezoelectric harvesters are tremendously diminished by the rigidly fixed condition. Thereby, the complex system with the isolator that supports the cooler with a low-stiffness to achieve the micro-vibration isolation function is also preferable in terms of energy harvesting capability point of view.

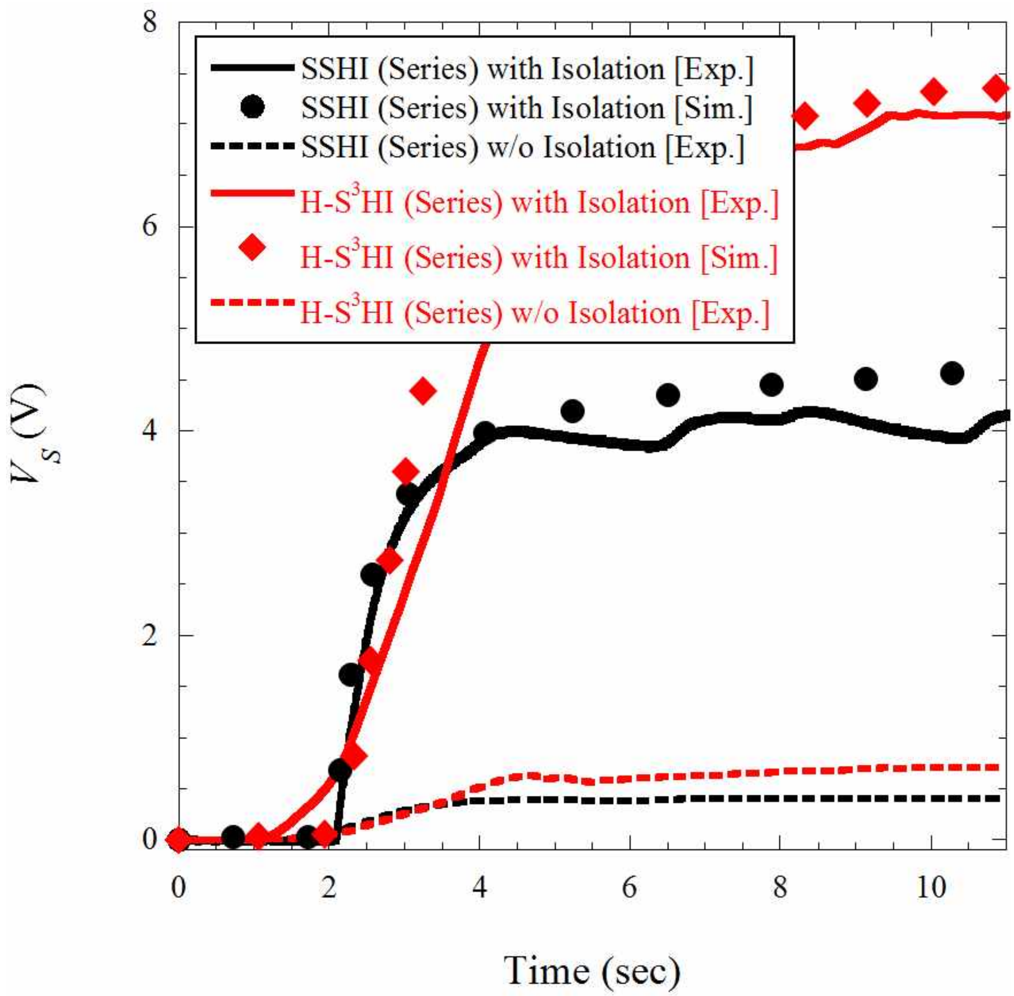

Fig. 73 Time History of Storage Voltage, V_s, at Complex System Level Test with Series Connection for Optimal SSHI and H-S^{3}HI Strategies, as a Function of with and w/o Isolation.

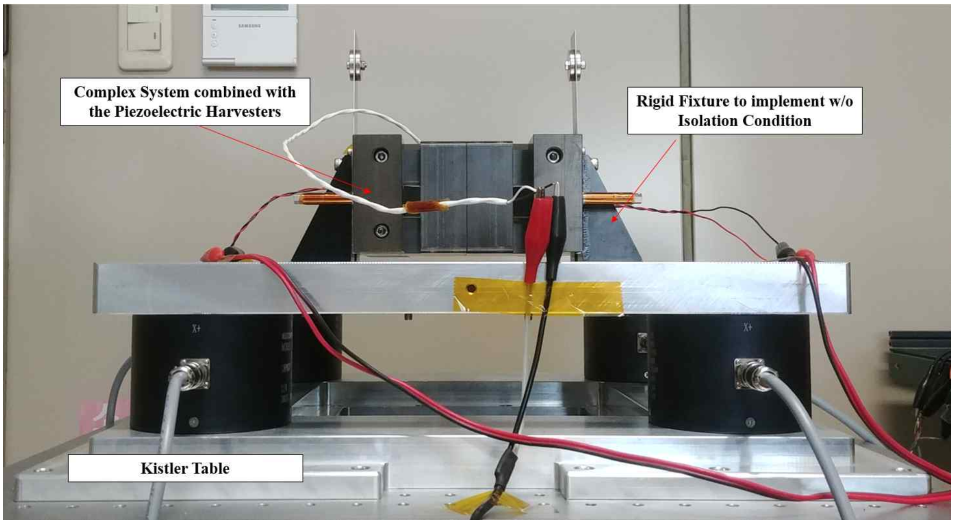

Fig. 74 Complex System mounted on Kistler Table with Rigid Fixture to implement the Condition without Isolation

As mentioned above, the simulation results were well in agreement with the experimental results. Thereby, the established equations of motion can be further used to expect the efficiency of the H-S^{3}HI strategy. So that, the energy harvesting efficiency of the proposed H-S^{3}HI strategy is investigated as a function of the electrical connecting conditions of the piezoelectric harvester in either parallel or series connection, by using the equations of motion of the complex system.

In general, the energy absorbed to the piezoelectric harvester can be divided into two categories, i.e. mechanical damping energy and electrical energy. The mechanical damping energy, $\overline{E_{cm}}$, dissipated by the mechanical damping of the piezoelectric harvester just converts to the unusable heat energy, otherwise the electrical energy, $\overline{E_{ce}}$, can be regarded as a useable recycling energy. However, all the electrical energy cannot be converted to the net energy but divided again into several energies, i.e. piezoelectric force energy $\overline{E_{av}}$, inductor working energy $\overline{E_{ind}}$, loss energy in resistances $\overline{E_{loss}}$, and net output energy $\overline{E_{out}}$. In here, the mechanical damping energy, $\overline{E_{cm}}$, can be calculated as following:

$$\overline{E_{cm}} = \frac{1}{t-0}\int_0^t [c_2(\dot{x}_2 - \dot{x}_1) + c_3(\dot{x}_3 - \dot{x}_1)]dt \tag{5-7}$$

Then, the electrical energy $\overline{E_{ce}}$ can be defined as,

$$\overline{E_{ce}} = \overline{E_{av}} + \overline{E_{ind}} + \overline{E_{loss}} + \overline{E_{out}} \tag{5-8}$$

In here, the piezoelectric force energy $\overline{E_{av}}$ exciting the vibration amplitudes of the cooler can be calculated as,

$$\overline{E}_{av} = \frac{1}{t-0}\int_0^t [\alpha_2 V_{p_2}(t)(\dot{x}_2(t) - \dot{x}_1(t)) + \alpha_3 V_{p_3}(t)(\dot{x}_3(t) - \dot{x}_1(t))]dt \tag{5-9}$$

The inductor working energy $\overline{E_{ind}}$ used to trigger the surging effect can be calculated as,

$$\overline{E}_{ind} = \frac{1}{t-0}\int_0^t V_B(t) i_I(t) dt \tag{5-10}$$

The loss energy $\overline{E_{loss}}$ dissipated in the resistances, i.e. switch resistance R_{sw} and diode resistance R_D can be calculated as,

$$\overline{E_{loss}} = \frac{1}{t-0}\int_0^t [(i_I^2(t) R_{sw}) + (i_s^2(t) R_D)] dt \tag{5-11}$$

Then, the net output energy $\overline{E_{out}}$ that can be used to actuate the low-power consuming sensor systems [27, 31-32] can be calculated as,

$$\overline{E}_{out} = \frac{1}{t-0}\int_0^t V_s(t) i_s(t) dt \tag{5-12}$$

Figure 71 shows the energy distribution plots of the H-S^{3}HI strategy under the series connection, obtained from above addressed energy equations. In order to normalize the energy efficiency, all the energy terms are divided by $\overline{E_{ce}} + \overline{E_{cm}}$, which indicates the entire energy absorbed in the piezoelectric harvester. As can be seen the figure, a portion of 23.8 % is just dissipated into unusable heat energy by the mechanical damping of the piezoelectric harvester, otherwise the rest of 76.2 % is converted into the electrical energy. This electrical energy is then divided into several energy terms. In here, the inductor working energy $\overline{E_{ind}}$ has a portion of 29.8 % and its energy is used to function the voltage inversion and surging voltage. The surging voltage is then forwarded to the storage capacitor via the diode resistance, as a result the storage capacitor is being charged with a portion of 6.9 %. Even if the efficiency of $\overline{E_{out}}$ is somehow small, the quantity of the harvested energy is still promising source to actuate the low-power-consuming sensors as already mentioned above. In fact, the previous study [27] that used a electromagnetic energy harvester to harvest the cooler-induced micro-vibration reported that the efficiency of the net output energy was 1.5 %. This fact means that the proposed H-S^3HI strategy is by far greater than the early harvesting strategy by the factor of 4.6.

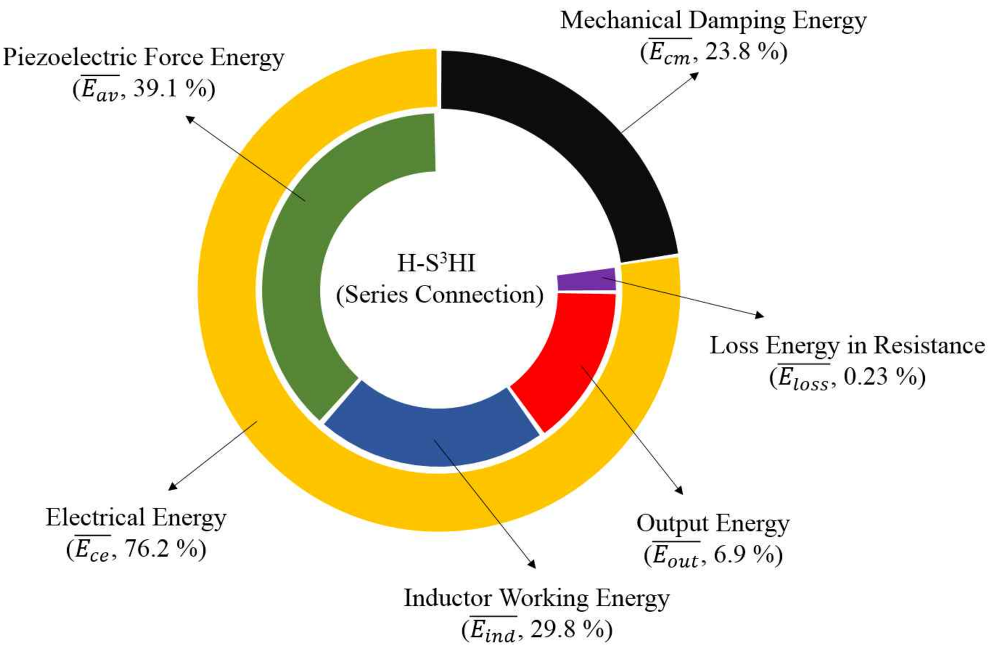

Fig. 75 Energy Distributions of H-S^{3}HI Strategy under Series Connection

Figure 72 shows the energy distribution plots of the H-S^{3}HI strategy under the parallel connection. In this figure, it can be noted that the mechanical damping energy is dominant unlike its role in the series condition shown in Fig. 71. Because the electrical energy absorbed in the piezoelectric harvester is significantly diminished due to relatively lower piezoelectric voltage produced under the parallel condition, compared to the series condition. In here, the relatively lower value of $\overline{E_{av}}$ compared to the series condition is dominant factor that affects the overall performance degradations. On the other hand, the energy portions in $\overline{E_{loss}}$ and $\overline{E_{ind}}$ are almost all similar with that of the series condition because of the same switching strategy. But, the net output energy just possesses a 0.8 % which is significantly lower efficiency compared to the series condition by the factor of 8.6. As a result, it can be said that the parallel connection of the piezoelectric harvester under the micro-vibration harvesting is un-preferable because the major contributor in harvesting the micro-vibration energy is the highly boosted voltage in combination with the surging effects of the H-S^{3}HI strategy. Thus, the series connection is more preferable.

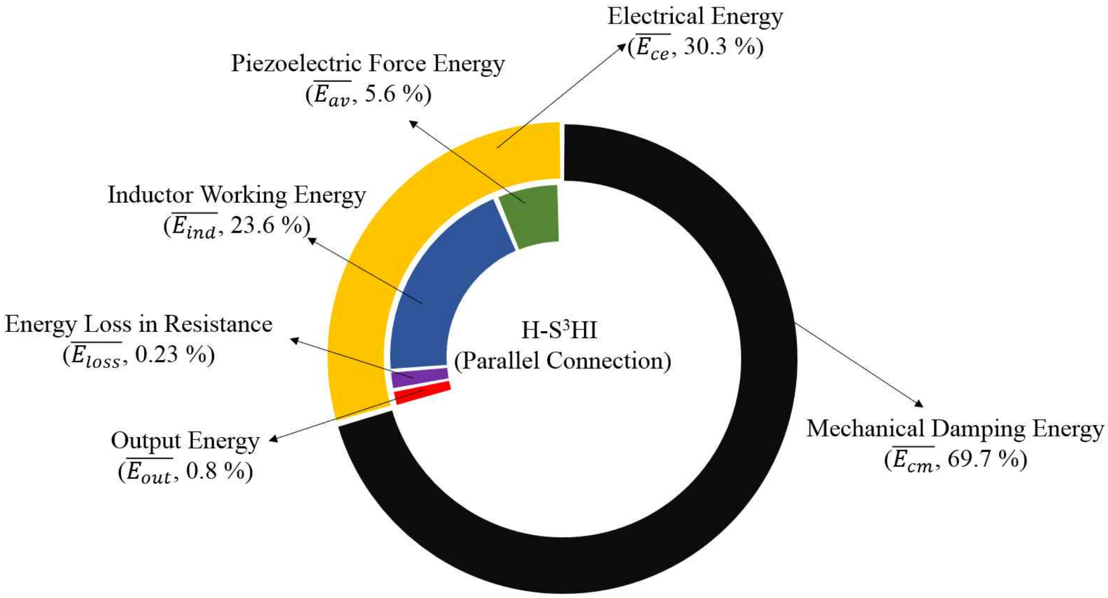

Fig. 76 Energy Distributions of H-S³HI Strategy under Parallel Connection

3. Vibration Isolation Performance Evaluation

Figures 73 and 74 show the time histories of the transmitted forces for the complex system with optimal SSHI and H-S^3HI strategy, as a function of the electrical connection of the piezoelectric harvester in both series and parallel connection. In here, the transmitted force from the cooler-induced micro-vibration was measured by the kistler table, as shown in Fig. 65. And the data labeled as rigid was obtained from the condition that the cooler was rigidly fixed on the kistler table by using the rigid fixture, as shown in Fig. 70. In this rigid condition, the cooler-induced micro vibrations defined as 2.5 N with the excitation frequency 40 Hz is directly transmitted to the kistler table, as shown in Figs. 73 and 74. This micro-vibration disturbance level could significantly degrade the image quality of the high-resolution observation satellite. As already investigated in Figs. 67 and 69, proper energy harvesting capability cannot be expected in this rigid condition as well. However, once the cooler is supported by the low-stiffened isolator shown in Fig. 62, the 1^{st} eigenfrequency of the cooler supported by the isolator becomes 8.2 Hz. This value is properly separated from the main excitation frequency of the cooler, namely 40 Hz, thereby frequency decoupling-based micro-vibration isolation performances are achieved, as shown in Figs. 73 and 74. For example, the micro-vibration level is significantly reduced to a value of 0.06 N in the series condition of the H-S^3HI strategy and its value is lower than the condition without the isolation by a factor of 41. This isolation performance is substantially identical for all cases regardless of which switching strategies and connecting conditions are applied because the major contributor of isolating the cooler-induced micro-vibration is the passive cooler vibration isolator by significantly lowering the 1^{st} eigenfrequency of the cooler assembly. In this isolation condition, much higher harvesting capability can be achieved as well as, shown in Figs. 67 and 69. Hence, it can be said that the complex system with the isolation condition can guarantee the hybrid demands of both effectively isolating the micro-vibration to comply with the strict jitter requirement of the high-resolution observation satellite and promisingly harvesting the cooler-induced micro-vibration.

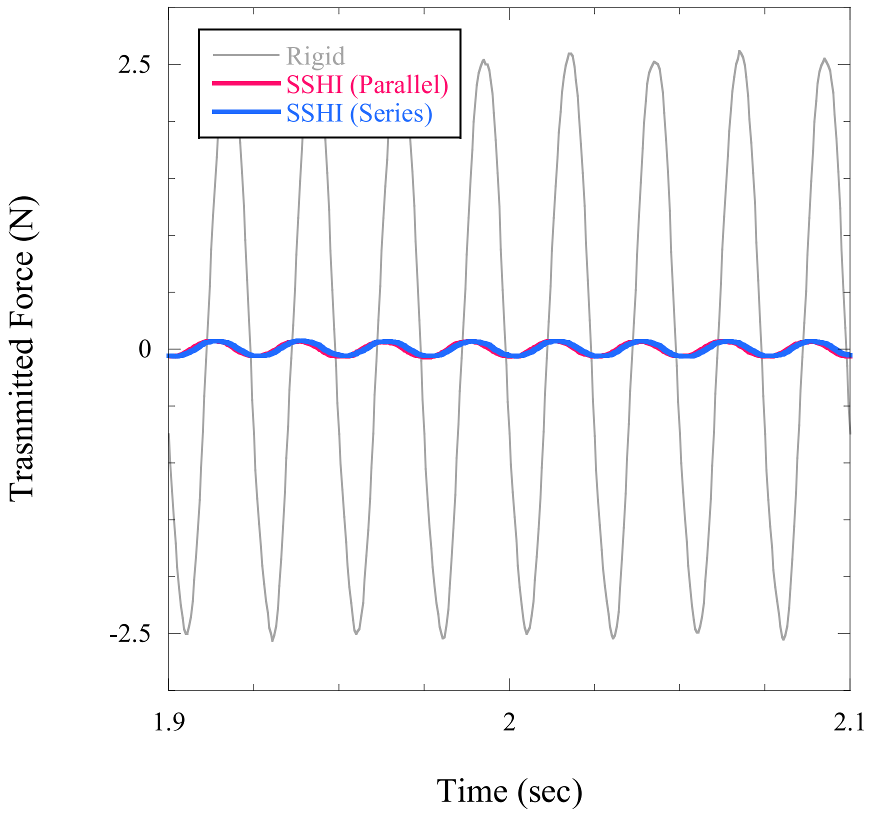

Fig. 77 Time Histories of Transmitted Forces for Complex System with Optimal SSHI Strategy, as a Function of Electrical Connections of Piezoelectric Harvester in Both Series and Parallel

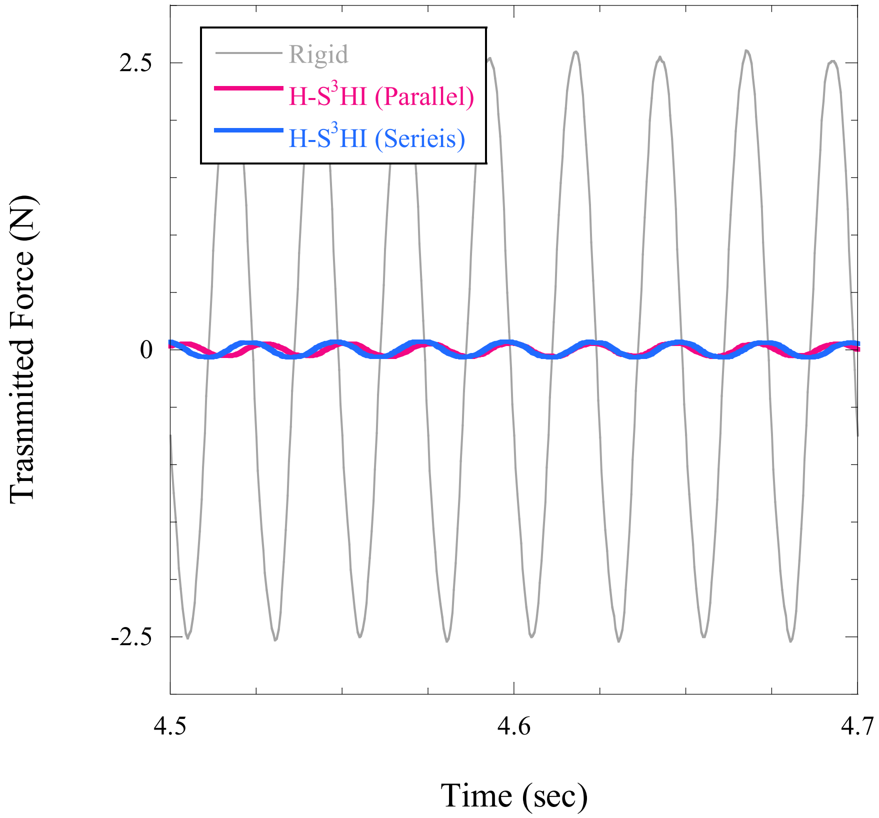

Fig. 78 Time Histories of Transmitted Forces for Complex System with Optimal H-S^{3}HI Strategy, as a Function of Electrical Connections of Piezoelectric Harvester in Both Series and Parallel

Figures 75 shows the summarization of the transmitted forces for the optimal SSHI and H-S^{3}HI strategy with respect to electrical connecting conditions of the piezoelectric harvester in both parallel and series, respectively. As shown in the figure, the transmitted forces in H-S^{3}HI case show relatively lower value compared to the SSHI case regardless of the connection of the piezoelectric harvester. Because much higher energy can be absorbed from the cooler-induced micro-vibrations, contributing to the vibration suppression effects. In this fact, it can be said that the proposed H-S^{3}HI strategy guarantees both superior harvesting and higher isolating capabilities, compared to the conventional SSHI strategy. On the other hand, once considering the electrical connectivity in either parallel or series for H-S^{3}HI case, it can be noted that the series case possesses relatively higher transmitted force level compared to the parallel case. Because there is a phase difference between cooler's displacement, x_1, and piezoelectric harvester's displacements, x_2 and x_3. Thereby, the switching actions of the H-S^{3}HI strategy that largely inverts the piezoelectric voltage act as an external excitation force on the cooler such that the vibration amplitudes of the cooler relatively increases. This phenomenon can be explained by Eqs. (5-2) by the terms of $\alpha_2 V_{p_2}$ and $\alpha_3 V_{p_3}$. In these terms, it can be expected that the larger the V_p becomes, the larger the displacement of the cooler x_1 becomes higher. Hence, the series condition, which produced much higher V_{p_2} and V_{p_3} compared to the parallel condition, shows relatively higher transmitted force level, even if its increasing level is almost all negligible. However, the amplitude amplification by the switching action positively results in increasing the piezo-induced current, i_p, as implied in Eqs. (5-5) and (5-6). In this manner, once considering the energy harvesting efficiency, the series condition has 8 times better performance compared to the parallel condition, as shown in Figs. 71 and 72. Once considering these facts in terms of energy, the piezoelectric force energy, $\overline{E_{av}}$, that excites the cooler vibration amplitudes is just 5.6 % in case of the parallel condition. Otherwise, the series condition possesses 39.1 % which is by far higher than the opposite case by the factor of approximately 7. As a result, the series condition is much preferable in energy harvesting capability point of view.

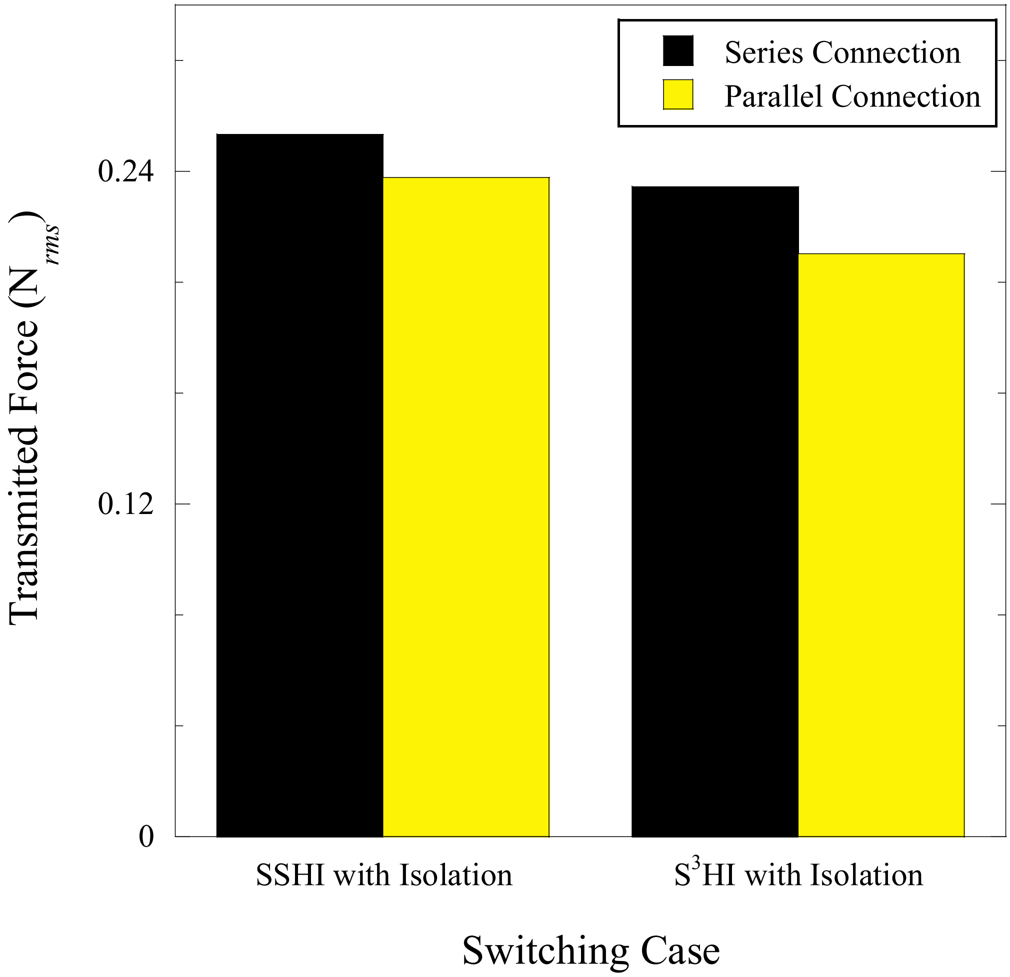

Fig. 79 Summarization of Transmitted Forces for Optimal SSHI and H-S^3HI Strategies with respect to Electrical Connecting Conditions of Piezoelectric Harvester in Both Parallel and Series Connections, respectively

VI. Conclusion

In this study, the feasibility of using the spaceborne cooler-induced micro-vibration energy as a renewable energy source by employing the piezoelectric energy harvester has been considered. To effectively harvest the micro-scale vibrations, a novel switching strategy, namely S^3HI, that intentionally induces a surge phenomenon resulted from sudden current transits in the inductor was proposed. This switching strategy can be further enhanced by controlling the switching duration. The effectiveness of the proposed switching strategy was verified through numerical and experimental approaches with a simply supported piezoelectric harvester, and the results indicate that the proposed strategy was much more efficient in regards to energy harvesting capability compared with conventional switching strategies, i.e., SSHI and standard one.

However, S^3HI strategy inevitably suffers from a series of energy losses in the inductor at every instance of switching, due to its relatively shorter switching duration compared with conventional SSHI. Thereby, to overcome the drawbacks of the S^3HI strategy, while still striving to induce surge phenomena to exploit their full potential from the point of view of energy harvesting capability, an enhanced strategy that combines high-frequency switching with the S^3HI switching was also proposed, complying both the demands of maximizing the incoming energy in the inductor and maintaining the surge-inducing mechanism, called H-S^3HI strategy. The effectiveness of the H-S^3HI strategy was verified through numerical and experimental approaches. Moreover, the feasibility of harvesting the random vibration by employing H-S^3HI strategy was experimentally investigated and its outputs implied the following advantages of the H-S^3HI strategy, e.g., requiring only a simple system without any feedback control but still powerful enough for random-vibration harvesting.

Based on numerical and experimental investigation results of the proposed H-S^3HI strategy, the feasibility of harvesting the cooler-induced micro-vibration was demonstrated at complex system level which comprised the cooler, the passive cooler vibration isolator, and the piezoelectric harvester. The experimental outputs indicated that the series connecting condition of the piezoelectric harvesters in line with the proposed H-S^3HI strategy possessed 8.6 times better performance in net output energy point of view, compared to the parallel condition. However, these addressed performances of the H-S^3HI strategy can be effectively guaranteed under the condition with the isolator that supports the cooler with a low-stiffness. In such a condition, the desirable micro-vibration isolation performance could be achieved by the frequency decoupling methodology. As a result, it can be said that the complex system with the isolation condition can guarantee the hybrid demands of both effectively isolating the micro-vibration to comply with the strict jitter requirement of the high-resolution observation satellite, and promisingly harvesting the cooler-induced micro-vibration in line with the proposed H-S^3HI strategy.

As a result, the advantages of the proposed surge-inducing switching strategies, i.e. S^3HI and H-S^3HI, can be summarized as followings:

1) It guarantees promising energy harvesting performance even under small vibration level due to surging-phenomenon

2) it does not require any feedback controller and system state observer for synchronized switching under the random vibration conditions, but simple and powerful in harvesting the random vibration

3) In case of H-S^3HI, its switching duration is the same with the optimal SSHI, thus the energy flowed toward the inductor is relatively higher than the S^3HI;

4) Thereby, the energy harvesting performance of the H-S^3HI is much higher than the S^3HI

5) In addition, H-S^3HI strategy guarantees hybrid functions of both isolating the micro-vibration and energy harvesting

Once considering high potential candidates for the piezoelectric harvesting system, artificial heart power supplier; streetlight, electronic board, and traffic light power supplier; and huge structures (high building, bridge and so on) health-monitoring system could be one of the examples. These addressed examples could be realized by the proposed switching strategy that enables promising energy harvesting performance even under small vibration level and random vibration, due to surging-phenomenon. Moreover, once considering the space applications, self-powered health monitoring system for on-board appendages that have mechanical moving parts, e.g. spaceborne cooler, gimbal antenna, solar array driver, reaction wheel assembly, control moment gyro, could be one of the promising application by sensing the temperature, vibration amplitude, and its frequency variations. The technological progress in nano-watt powered sensor applications [57-59] has triggered above mentioned health monitoring sensor system, overcoming critical obstacles that prevent the realization of energy harvesting systems, especially on micro-vibration fields. In addition, the piezoelectric harvester with the proposed switching strategy can be applied in harvesting the launch vibration energy that is significantly huge one compared with the above mentioned micro-vibration energy from the satellite on-board appendages. The recycled energy during the launch periods can be used to heat some on-board payloads at an initial orbit phase to help the payload stay within allowable operating temperature ranges, contributing to the increase of power budget in satellite system point of view. Aside from abovementioned applications, it is promisingly expected that the proposed surge-inducing switching strategy can hugely contribute to the energy harvesting filed and can trigger the new challenge toward micro-vibration filed as potential harvesting source.

VII. Future Study

The ultimate goal of this research was effectively harvesting the micro-scale vibration energy induced by the cooler, by employing the piezoelectric harvesting system in combination with the novel surge-inducing switching strategy, i.e. S^3HI and H-S^3HI.

In this study, however, the piezoelectric harvester was just designed in consideration of the frequency coupling effect between the main excitation frequency of the cooler and the 1st eigenfrequency of the piezoelectric harvester. Thereby, if taking the optimal values of damping, proof mass and stiffness of the piezoelectric harvester was into account based on optimal tuned mass damper design approach [60-63], much more performances from the piezoelectric harvester could be achieved.

In case of satellite, it has a lot of vibration-inducing on-board appendages that can be regarded as recycling energy sources like the spaceborne cooler considered in this study. For example, solar array driver, gimbal-type antenna, reaction wheel assembly, control moment gyro, scanning mirror, telescope focus adjusting mechanism and so on. In here, investigating the harvesting energy quantitatively considering the vibration amplitudes and operating times for each payload could be worthful future study by using the proposed switching strategy.

Moreover, to realize the applicability of the proposed harvesting system toward the space program in future study, following development processes that are generally applied in space program [64-66] are required. First, it needs to define the development model philosophy such as engineering model (EM), qualification model (QM), and flight or proto-flight model (FM or PFM); Second, it needs to define the system requirement and design specification with regard to each development model; Third, it needs to define the verification test items with regard to each development model. For example in third phase, followings are required to be included in the verification test item, i.e. functional performance test from the sub-assembly level to the system level; environment tests such as thermal vacuum test and launch vibration test. Once the proposed harvesting system deals with above development process and complies with the system requirement, it can be practically used in space program. If on-boarding such a harvesting system in cube satellite or science satellite is available, it would be great chance to get the space heritage with regard to the relevant technologies required to implement the proposed piezoelectric harvesting system in line with the surge-inducing switching strategy, hugely spawning various researches and affecting various industries that require the energy harvesting technology.

【Reference】

1) D. Guyomar, A. Badel, E. Lefeuvre and C. Richard, “Toward energy harvesting using active materials and conversion improvement by nonlinear processing”, IEEE Transactions on Ultrasonics, Ferroelectrics and Frequency Control, Vol. 52, No. 4, pp. 584-595, 2005

2) H. U. Oh, “Variable damping semi-passive vibration isolation for enhancing pointing performance of on-board payload”, Journal of the Korean Society for Aeronautical and Space Sciences, Vol. 35, No. 6, pp. 533-538, 2007

3) J. P. Karl and C. J. Schauwecker, "Use of a passive reaction wheel jitter isolation system to meet the advanced X-ray astrophysics facility imaging performance requirements", Progress in Biomedical Optics and Imaging, No. 3356, pp.1078-1094, 1998

4) D. Poter, C. David and H. John, “Advanced 1.5 Hz passive viscous isolation system”, Proceeding of the 35th AIAA SDM Conference, Hilton Head, South Carolina, April, 1994

5) S. V. Riabzev, A. M. Veprik, H. S. Vilenchik, N. Pundak and E. Castiel, "Vibration-free stirling cryocooler for high definition microscopy", Cryogenics, Vol. 49, No. 12, pp. 707~713, 2009

6) G. C. Richard, M. S. Jeanne, D. Alok, L. P. Davis, T. T. Hyde, D. Torey, H. R. Zahidul and T. S. John, "Vibration isolation and suppression for precision payloads in space", Smart Materials & Structures, Vol. 8, No. 6, pp. 798~812, 1999

7) D. Kamesh, R. Pandiyan and A. Ghosal, "Passive vibration isolation of reaction wheel disturbances using a low frequency flexible space platform", Journal of Sound and Vibration, Vol. 331, No. 6, pp. 1310~1330, 2012

8) S. C Kwon, S. H. Jeon and H. U. Oh, “Smart adaptive passive vibration isolation system for launch and on-orbit vibration isolation”, 2015 The 8th Asian-Pacific Conference on Aerospace Technology and Science, Jeju Island, Korea, 2015

9) S. C. Kwon, S. H. Jeon and H. U. Oh, “SMA mesh washer applications for launch and on-orbit vibration isolation”, The 44th Inter-Noise Congress & Exposition on Noise Control Engineering, San Francisco, USA, 2015

10) S. C. Kwon, Y. H. Park and H. U. Oh, “Characteristics of spaceborne cooler vibration isolator using a pseudoelastic shape memory alloy”, SPIE Smart Structures NDE, Portland Oregon, USA, 2017

11) S. C. Kwon, S. H. Jeon and H. U. Oh, “Performance evaluation of spaceborne cryocooler micro-vibration isolation system employing pseudoelastic SMA mesh washer”, Cryogenics, Vol. 67, 2015, pp.19-27

12) H. U. Oh, S. C. Kwon and S. H. Youn, “Characteristics of spaceborne cooler passive vibration isolator by using a compressed shape memory alloy mesh washer”, Smart Materials and Structures, Vol. 24, No. 1, pp. 015009-015020, 2015

13) S. C. Kwon, M. S. Jo and H. U. Oh, “Experimental validation of fly-wheel passive launch and on-orbit vibration isolation system by using a superelastic SMA mesh washer isolator”, International Journal of Aerospace Engineering, Vol. 2017, pp. 1-16, 2017

14) S. C. Kwon, S. H. Jeon and H. U. Oh, “Performance investigation of a novel pseudoelastic SMA mesh washer gear wheel with micro-jitter attenuation capability”, Smart Materials and Structures, Vol. 25, No. 5, pp. 055004-055018, 2016

15) S. C. Kwon and H. U. Oh, “Passive micro-jitter isolation of gimbal-type antenna by using a superelastic SMA gear wheel”, Mechanical Systems and Signal Processing, Vol. 114, No. 1, pp. 35-53, 2019

16) S. H. Jeon, S. C. Kwon, T. H. Kim and H. U. Oh, “Enhancement of micro-jitter attenuation capability for a stepper actuated two-axis gimbal-type antenna by using spring-blade isolator”, ASCE Journal of Aerospace Engineering, Vol. 30, No. 4, pp. 1-9, 2017

17) S. C. Kwon, S. H. Jeon and H. U. Oh, “Derivation of numerical equivalent

model of vibration isolator using pseudoelastic SMA mesh washer", Journal of the Society for Aerospace System Engineering, Vol. 8, No. 3, pp. 6-13, 2014

18) S. H. Joen, S. C. Kwon, D. K. Kim and H. U. Oh, "Investigation of micro-vibration isolation performance of SMA mesh washer isolator for vibration isolation of X-band antenna", Journal of the Korean Society for Aeronautical and Space Sciences, Vol. 42, No. 11, pp. 988-995, 2014

19) S. C. Kwon, S. H. Jeon and H. U. Oh, "On-orbit micro-vibration isolation performance verification for spaceborne cryocooler passive vibration isolator using SMA mesh washer", Transactions of the Korean Society for Noise and Vibration Engineering, Vol. 25, No. 1, pp. 24-32, 2015

20) S. H. Jeon, S. C. Kwon, T. H. Kim, Y. H. Kim and H. U. Oh, "Micro-vibration isolation performance of X-band antenna using blade gear", Transactions of the Korean Society for Noise and Vibration Engineering, Vol. 25, No. 5, pp. 313-320, 2015

21) K. Ylli, D. Hoffmann, A. Willmann, P. Becker, B. Folkmer and Y. Manoli, "Energy harvesting from human motion: exploiting swing and shock excitations", Smart Materials and Structures, Vol. 24, No. 2, pp. 1-12, 2015

22) L. Zhongjie, Z. Lei, K. Jian and L. George, "Energy-harvesting shock absorber with a mechanical motion rectifier", Smart Materials and Structures, Vol. 22, No. 2, pp. 1-10, 2013

23) V. B. Thomas, D. M. Paul, C. G. Tim, M. Y. Eric, S. H. Andrew and T. Gerhard, "Optimization of inertial micro-power generators for human walking motion", Sensors Journal, IEEE, Vol. 6, No. 1, pp. 28-38, 2006

24) Z. Dibin, R. Stephen, J. T. Michael and P. B. Stephen, "Design and experimental characterization of a tunable vibration-based electromagnetic micro-generator", Sensors and Actuator A: Physical, Vol. 158, No. 2, pp. 284-293, 2010

25) K. Makihara, J. Onoda and K. Minesugi, "A self-sensing method for switching vibration suppression with a piezoelectric actuator", Smart

Materials and Structures, Vol. 16, No. 2, pp. 455-461, 2007

26) S. C. Kwon and H. U. Oh, “Numerical feasibility study for a spaceborne cooler dual-function energy harvesting system”, International Journal of Aeronautical and Space Sciences, Vol. 18, No. 3, pp. 112-121, 2017

27) S. C. Kwon and H. U. Oh, “Experimental validation of satellite micro-jitter management strategy in energy harvesting and vibration isolation”, Sensors and Actuators A: Physical, Vol. 249, pp. 172-185, 2016

28) S. C. Kwon, M. S. Jo and H. U. Oh, “Numerical investigation of complex system for electrical energy harvesting and vibration isolation”, Journal of the Korean Society for Aeronautical and Space Sciences, Vol. 42, No. 8, pp. 648-653, 2014

29) S. C. Kwon, S. H. Jeon and H. U. Oh, “Experimental investigation of complex system for electrical energy harvesting and vibration isolation”, Journal of the Korean Society for Aeronautical and Space Sciences, Vol. 44, No. 1, pp. 40-48, 2016

30) S. C. Kwon, S. H. Jeon, Y. G. Lee, S. J. Kang and H. U. Oh, “Performance investigation of cryocooler micro-jitter isolation system combined with energy harvesting tuned mass damper”, The 30th International Symposium on Space Technology and Science, Kobe-Huogo, Japan, 2015

31) T. Shimamura, N. Ugajin, J. Suzuki, K. Ono, N. Sato, K. Kuwabara, H. Morimura and S. Mutoh, “Nano-watt power management and vibration sensing on a dust-size battery-less sensor node for ambient intelligence applications" 2010 IEEE International Solid-State Circuits Conference (ISSCC), San Francisco, CA, 2010, pp. 504-505

32) A. M. Aragon, “Space applications of micro/nano-technologies”, Journal of Micromechanics and Microengineering, Vol. 8, pp. 54-56, 1996

33) W. A. Shen, S. Zhu and Y. L. Xu, “An experimental study on self-powered vibration control and monitoring system using electromagnetic TMD and wireless sensors”, Sensors and Actuators A: Physical, Vol. 180, pp. 166-176,

2012

34) M. E. Hami, P. G. Jones, N. M. White, M. Hill, S. Beeby, E. James, A. D. Brown and J. N. Ross “Design and fabrication of a new vibration-based electromechanical power generator”, Sensors and Actuators A: Physical, Vol. 92, No. 1-3, pp. 335-342, 2001

35) J. Liang and W. H. Liao, “Improved design and analysis of self-powered synchronized switch interface circuit for piezoelectric energy harvesting systems”, IEEE Transactions on Industrial Electronics, Vol. 59, No. 4, pp. 1950-1960, 2012

36) Y. Y. Chen, D. Vasic, F. Costa, W. J. Wu and C. K. Lee, “Self-powered piezoelectric energy harvesting device using velocity control synchronized switching technique”, IECON 2010 36th Annual Conference on IEEE Industrial Electronics Society, 2010

37) E. Lefeuvre, A. Badel, C. Richard and D. Guyomar, “piezoelectric energy harvesting device optimization by synchronous electric charge extraction”, Journal of Intelligent Material Systems and Structures, Vol. 16, No. 10, pp. 865-876, 2005and Actuators A: Physical, Vol. 249, pp. 172-185, 2016

38) R.G. Ross and D.L. Johnson, “NASA’s advanced cryocooler technology development program”, Advances in Cryogenic Engineering, Vol. 823, pp. 607-614

39) A. Veprik, S. Zechtzer, N. Pundak, S. Riabzev, C. Kirckonnel and J. Freeman, "Low vibration microminiature split stirling cryogenic cooler for infrared aerospace applications." AIP Conference Proceedings Series, Vol. 1434, No. B, pp. 1473-1480

40) R. Radebaugh, “Pulse tube cryocoolers for cooling infrared sensors”, Proceedings of SPIE, The International Society for Optical Engineering, Infrared Technology and Applications XXVI, Vol. 4130, pp. 363-379

41) J. Onoda, S. Shimose and K. Minesugi, “Optimal configuration and combination of piezoelectric transducer and inductor for

synchronized-switch-damping-on-an-inductor technique", Journal of Intelligent Material Systems and Structures, Vol. 28, No. 7, pp. 1-19, 2017

42) R. Pierret, "Semiconductor Device Fundamentals" New York: Addison-Wesley Publishing Company, 1996

43) R. Solecki and R. J. Conant, "Advanced Mechanics of Materials" New York: Oxford University Press, 2003

44) S. Katzir, "The Discovery of the Piezoelectric Effect", Archive for History of Exact Sciences, Vol. 57, No. 1, pp. 61-91, 2003

45) S. Priya, "Modeling of electric energy harvesting using piezoelectric windmill", Applied Physics Letters, Vol. 87, No. 18, 2005

46) S. Roundy, P. K. Wight and J. Rabaey, "A study of low level vibrations as a power source for wireless sensor nodes," Computer Communications, Vol. 26, No. 11, pp. 1131–1144, 2003

47) T. Starner, "Human-powered wearable computing", Vol. 35, No. 3-4, pp. 618-629, 1996

48) X. J. Yan and J. X. Nie, "Study of a new application form of shape memory alloy superelasticity", Smart Materials and Structures, Vol. 12, No. 6, pp. 14-23, 2003

49) F. Calame and P. Muralt, "Growth and properties of gradient free sol-gel lead zirconate titanate thin films", Applied Physics Letters, Vol. 90, No. 6, 2007

50) K. Makihara, Y. Yamamoto, K. Yoshimizu, C. Horiguchi, H. Sakaguchi and K. Fujimoto, "A novel controller to increase harvested energy from negating vibration-suppression effect", Smart Materials and Structures, Vol. 24, No. 3, pp. 037005-037011, 2015

51) J. Liang and W. H. Liao, "Energy Flow in Piezoelectric Energy Harvesting Systems", Smart Materials and Structures, Vol. 20, No. 1, pp. 015005-015016, 2011

52) H. U. Oh, K. J. Lee and M. S. Jo, "A passive launch and on-orbit vibration isolation system for the spaceborne cryocooler", Aerospace Science and

Technology, Vol. 28, No. 1, pp. 324-331, 2013

53) J. J. Wijker, "Spacecraft structures", Springer, 2008

54) S. H. Youn, Y. S. Jang and J. H. Han, "Compressed mesh washer isolators using the pseudoelasticity of SMA for pyroshock attenuation", Journal of Intelligent Material Systems and Structures, Vol. 21, pp. 407-421, 2010

55) S. H. Youn, Y. S. Jang and J. H. Han, "Development of a three-axis hybrid mesh isolator using the pseudoelasticity of a shape memory alloy", Smart Materials and Structures, Vol. 20, No. 7, pp. 1-12, 2011

56) S. C. Kwon, Y. H. Jeon and H. U. Oh, "Micro-jitter attenuation of spaceborne cooler by using a blade-type hyperelastic shape memory alloy passive isolator", Cryogenics, Vol. 87, pp. 35-48, 2017

57) T. Shimamura, H. Morimura, K. Kuwabara, N. Sato, J. Terada and M. Ugajin, "A capacitive sensing scheme for control of movable element with complementary metal-oxide-semiconductor microelectromechanical-systems device", Japanese Journal of Applied Physics, Vol. 47, No. 5R, pp. 3418-3422, 2008

58) X. Zou, X. Xu, L. Yao and Y. Lian, "A 1-V 450-nW fully integrated programmable biomedical sensor interface chip", IEEE Journal of Solid-State Circuits, Vol. 44, No. 4, pp. 1067-1077, 2009

59) G. Balachandran and R. E. Barnett, "A 110 nA voltage regulator system with dynamic bandwidth boosting for RFID systems", IEEE Journal of Solid-State Circuits, Vol. 41, No. 9, pp. 2019-2028, 2006

60) F. Weber and M. Maslanka, "Frequency and damping adaptation of a TMD with controlled MR damper", Smart Materials and Structures, Vol. 21, No. 5, pp. 1-17, 2012

61) J. S. Bae, J. H. Hwang, J. H. Roh, J. H. Kim. M. S. Yi and J. H. Lim, "Vibration suppression of a cantilever beam using magnetically tuned-mass-damper", Journal of Sound and Vibration, Vol. 331, No. 26, pp. 5669-5684, 2012

62) G. L. Larose, A. Larsen and E. Svensson, “Modeling of tuned mass dampers for wind-tunnel tests on a full-bridge aeroelastic model”, Journal of Wind Engineering and Industrial Aerodynamics, Vol. 54-55, pp. 427-437, 1995

63) A. A. Farghaly and M. S. Ahmed, “Optimum design of TMD system for tall buildings”, International Scholarly Research Network Civil Engineering, Vol. 2012, pp. 1-13, 2012

64) T. D. Tuttle and W. P. Seering, “Experimental verification of vibration reduction in flexible spacecraft using input shaping”, Journal of Guidance, Control, and Dynamics, Vol. 20, No. 4, pp. 658-664, 1997

65) J. D. Nielsen and J. A. Larsen, “A decentralized design philosophy for satellites”, Recent Advances in Space Technologies, 5th International Conference, 2011

66) H. U. Oh, S. H. Jeon and S. C. Kwon, “Structural design and analysis of 1U standardized STEP cube lab for on-orbit verification of fundamental space technologies”, International Journal of Materials, Mechanics and Manufacturing, Vol. 2, No. 3, pp.239-244, 2014